

DTIC FILE COPY

AD-A215 673



DTIC
ELECTE
DEC 28 1989
S DCS D

GROUND-BASED DEEP-SPACE LADAR
FOR SATELLITE DETECTION:
A PARAMETRIC STUDY

THESIS

Kevin F. G. Davey
Flight Lieutenant, RAAF

AFIT/GSO/ENP/ENS/89D-1

DISTRIBUTION STATEMENT A

Approved for public release;
Distribution Unlimited

DEPARTMENT OF THE AIR FORCE

AIR UNIVERSITY

AIR FORCE INSTITUTE OF TECHNOLOGY

Wright-Patterson Air Force Base, Ohio

89 12 27 051

AFIT/GSO/ENP/ENS/89D-1

DTIC
ELECTE
DEC 28 1989
S D

GROUND-BASED DEEP-SPACE LADAR
FOR SATELLITE DETECTION:
A PARAMETRIC STUDY

THESIS

Kevin F. G. Davey
Flight Lieutenant, RAAF

AFIT/GSO/ENP/ENS/89D-1

DISTRIBUTION STATEMENT A
Approved for public release;
Distribution Unlimited

Accession For	
NTIS (GPO)	<input checked="" type="checkbox"/>
DTIC TAG	<input type="checkbox"/>
Unpublished	<input type="checkbox"/>
Justification	
By	
Distribution	
Availability Codes	
Dist	Availability or Special
A-1	

Approved for public release; distribution unlimited

AFIT/GSO/ENP/ENS/89D-1

GROUND-BASED DEEP-SPACE LADAR
FOR SATELLITE DETECTION:
A PARAMETRIC STUDY

THESIS

Presented to the Faculty of the School of Engineering
of the Air Force Institute of Technology
Air University
In Partial Fulfillment of the
Requirements for the Degree of
Master of Science in Space Operations

Kevin F. G. Davey, B.E.
Flight Lieutenant, RAAF

December, 1989

Approved for public release; distribution unlimited

Preface

The purpose of this research was to determine the minimum performance requirements for a ground-based, infrared LADAR designed to detect deep-space satellites, and to select a candidate sensor design using available technology. The research shows that a design capable of high accuracy and resolution is feasible using current technology, with greatly improved sensor availability compared to the Ground-Based Electro-Optical Deep-Space Surveillance (GEODSS) system currently in use.

I wish to thank my thesis advisor, Lieutenant Colonel Howard Evans, for providing constructive comments and acting as a 'sounding-board' throughout this research. I also thank Major Thomas Kelso, my co-advisor, for assistance with \LaTeX , and Michael Wichura for inventing the \PjCTEX macros. Finally, I wish to thank my family for their perseverance throughout this 1,500-hour 'academic exercise'.

Kevin F. G. Davey

Table of Contents

	Page
Preface	ii
Table of Contents	iii
List of Figures	iv
List of Tables	v
List of Symbols	vi
Abstract	vii
I. Introduction	1
Background	1
Specific Problem	2
Scope and Limitations	3
Methodology	3
LADAR Techniques.	4
The Infrared Environment.	4
Parametric Analysis.	4
Candidate Design.	5
II. Literature Review	6
Introduction	6
Deep-Space Surveillance Objectives	6
GEODSS	7
LADAR History	10

	Page
Firepond LADAR	10
Current LADAR Technology	11
Summary	12
III. LADAR Techniques	13
Introduction	13
Target Characteristics	13
LADAR Detection Methods	17
Pulse Compression.	20
LADAR Transmitters	21
CO ₂ Transmitters.	21
Nd:YAG Transmitters.	23
DF Transmitters.	23
Detectors	24
Optics	25
Acquisition, Tracking, and Pointing	27
Summary	29
IV. The Infrared Environment	32
Introduction	32
Atmospheric Models	32
Background Radiance	34
Atmospheric Transmission	38
Look Angle.	41
Cloud and Rain.	42
Other Effects	47
Turbulence.	47
High-Power Beam Effects.	50
Summary	51

	Page
V. Parametric Analysis	53
Introduction	53
Detection Probability	53
The LADAR Equation	60
Transmitter Antenna Gain	61
Receiver Antenna Gain	69
Gaussian LO Distribution.	76
Uniform LO Distribution.	78
Phase Front Misalignment.	79
FPA Detection Analysis	83
LADAR Accuracy	90
LADAR Resolution	91
Angular Resolution	92
Summary	93
VI. Candidate Design	97
Introduction	97
Design Calculations	97
Unmodulated Pulse Train	100
Alternative Designs	104
Space-Based LADAR.	104
Target Enhancement.	105
FM-Chirp Pulse Train	106
Resolution and Accuracy.	108
Sensitivity and Coverage.	109
Summary	110
VII. Conclusions	112
Recommendations	114

	Page
Appendix A. FPA Detection Analysis	116
Two Overlapped Pixels	116
Three Overlapped Pixels	119
Four Overlapped Pixels	122
Summary	124
Bibliography	128
Vita	134

List of Figures

Figure	Page
1. Classes of Orbits for Deep-Space Objects	14
2. Typical Sensor-Target Viewing Geometry	15
3. Block Diagram of Pulse-Doppler LADAR using Heterodyne Detection	18
4. Cassegrainian Telescope Configuration	27
5. Geometry for Calculation of Solar and Thermal Scattered Radiance	35
6. Background Spectral Radiance in the 1-3 μm Band, Calculated Using LOWTRAN7 for two Cases: 70° Look Angle From Sea-level Against a Clear Sky, and 10° Look Angle From Sea-level Against a Cloudy Sky	36
7. Background Spectral Radiance in the 3-12 μm Band, Calculated Using LOWTRAN7 for two Cases: 70° Look Angle From Sea-level Against a Clear Sky, and 10° Look Angle From Sea-level Against a Cloudy Sky	37
8. Atmospheric Transmittance of Frequency-Doubled CO ₂ Laser Transi- tions over a Vertical Path from Ground to Space for three cases: Mid- Latitude Summer and Winter Atmospheres with Rural Aerosol, and Tropical Atmosphere with Maritime Aerosol	40
9. Atmospheric Transmittance of Five Selected Laser Wavelengths over a Vertical Path from Ground to Space for three cases: Mid-Latitude Winter and Summer Atmospheres with Rural Aerosol, and Tropical Atmosphere with Maritime Aerosol	41
10. Atmospheric Transmittance at Socorro — Slant Path from 1.53 km Altitude to Space, Through a Mid-Latitude Winter Atmosphere and Rural Aerosol with 23 km Visibility	43
11. Atmospheric Transmittance at Diego Garcia — Slant Path from Sea- Level to Space, Through a Tropical Atmosphere and Maritime Aerosol with 23 km Visibility	43
12. Transmittance Component due to Cloud and Rain from Socorro for Three Cases: Cirrus Cloud from 8 km to 9 km Altitude, Drizzle Orig- inating from 2 km, Light Rain from 2 km, and Moderate Rain from 2 km	46

Figure	Page
13. Transverse Phase Coherence Length for Transmit and Receive Paths versus Wavelength	50
14. LADAR Detection Circuitry (Adapted from Bachman (6:39))	54
15. Graphical Representation of p_t and p_{fa}	57
16. Minimum SNR Requirement using Post-Detection Multi-Pulse Integration, and $p_t = 0.95$ for various p_{fa} (Extracted from Skolnik (73:2-21))	58
17. LADAR Transmitter Aperture Geometry	63
18. Transmitter Efficiency Variation against Off-Axis Parameter	69
19. Detector Geometry	70
20. Airy Size Parameter Variation with Obscuration Ratio	72
21. Optimum Airy-to-LO Ratio versus Detector-to-Airy Ratio for Gaussian LO Distribution	77
22. Heterodyne Efficiency versus Detector-to-Airy Ratio for Gaussian LO	78
23. Heterodyne Efficiency versus Detector-to-Airy Ratio, for Uniform LO	79
24. LO-Received Beam Misalignment Geometry (Reproduced from Wang (82:3422))	80
25. Heterodyne Efficiency versus Misalignment Parameter, $\beta = ka \sin \delta$	82
26. Normalized Airy Disk Power versus Normalized Image Radius	84
27. Normalized Integrated Airy Power as a Function of Outer Image Radius	85
28. Possible Image Locations on an FPA for $\gamma = 0.2$ and $L/g = 1.67$	86
29. Distribution of Image Center Locations for n overlapped pixels	87
30. Maximum Signal Fraction when Image Overlays n Pixels and $\gamma = 0.2$	88
31. Probability of Image Overlaving n Pixels with $\gamma = 0.2$	89
32. Expected Maximum Signal Fraction for FPA detection	90
33. Image Center Geometry for the Case of Two Overlapped Pixels	117
34. Image Center Geometry for the Case of Three Overlapped Pixels	119
35. The Two Possible Image-Pixel Geometries for the Cases of Three and Four Overlapped Pixels	121

Figure	Page
36. Image Center Geometry for the Case of Four Overlapped Pixels . . .	123
37. Maximum Signal Fraction when Image Overlays n Pixels and $\gamma = 0$. . .	125
38. Maximum Signal Fraction when Image Overlays n Pixels and $\gamma = 0.4$. . .	125
39. Probability of Image Overlaying n Pixels with $\gamma = 0$	126
40. Probability of Image Overlaying n Pixels with $\gamma = 0.4$	126

List of Tables

Table	Page
1. Summary of Known, Lost, Deep-Space Satellites (Reproduced from (78:5))	7
2. GEODSS Telescope Characteristics	8
3. Firepond LADAR Characteristics (Extracted from (26:329))	11
4. GEODSS Site Characteristics (Extracted from (47:57; 30:III-22))	35
5. Laser Transition Wavelengths used in FASCOD2 Calculations	39
6. Candidate LADAR Design Sequence	99
7. Candidate Design Specifications for all Detection Cases Using an Unmodulated Transmitter Pulse Train	101
8. Received Power Calculations at 11.17 μm Using an Unmodulated Pulse Train	102
9. Received Power Calculations at 4.64 μm Using an Unmodulated Pulse Train	103
10. Received Power for Enhanced Target and an Unmodulated Pulse Train	106
11. Received Power Calculations Using a Linear-FM Chirp Pulse Train	107

List of Symbols

Symbol		Page
σ_{LCS}	LADAR target cross-section	16
ρ_{ir}	Infrared target reflectivity	16
A	Projected physical target area	16
B_{FM}	Frequency-modulated bandwidth of transmitted pulse	20
τ	Transmitted pulse width	20
R	Target range	28
c	Speed of light	28
T	Total transmitted waveform duration	28
α_r	Receiver angular field-of-view	29
ψ_s	Sensor look angle	44
C_n^2	Refractive-index structure coefficient	48
σ_x^2	Variance in log-amplitude of received signal	48
r_o	Transverse phase coherence length	49
r_{ot}	Transverse phase coherence length for transmitter-to-target path	49
k	Angular spatial frequency	49
r_{or}	Transverse phase coherence length for target-to-receiver path	49
p_d	Probability of detection	54
p_{fa}	Probability of false-alarm	54
σ_n^2	Average noise power	55
r_t	Threshold for detection decision	55
t_{fa}	Mean time between false-alarms	55
M	Number of pulses in transmitted signal	55
t_g	Receiver range gate on-time	56
σ_d^2	Average signal power from diffuse target	56

Symbol		Page
σ_t^2	Total average received power from noise and diffuse target	56
$S.N.R$	Signal-to-noise power ratio	57
$\langle P_{lo} \rangle$	Mean local oscillator power	59
η_q	Detector quantum efficiency	59
λ	Photon wavelength	59
B	Detector and intermediate-frequency bandwidth	59
q	Charge per electron	59
h	Planck's constant	59
$\langle P_{if} \rangle$	Mean intermediate-frequency power	60
$\langle P_r \rangle$	Mean received signal power	60
P_t	Transmitter power	60
G_t	Transmitter power gain	60
τ_{to}	Transmitter optics transmittance	61
τ_A	One-way atmospheric transmittance	61
G_r	Receiver power gain	61
τ_{ro}	Receiver optics transmittance	61
A_t	Transmit antenna primary aperture area	62
η_t	Transmit antenna efficiency	62
ϵ_o	Permittivity of free-space	62
θ	Off-boresight target angle	63
a	Primary aperture radius	65
b	Secondary aperture radius	65
ω	Laser beam radius	66
R_ϕ	Laser beam phase-front curvature at transmitter aperture	66
X	Off-axis parameter	67
α	Ratio of aperture to laser beam radii	68
γ	Telescope obscuration ratio	68

Symbol		Page
A_r	Receive antenna primary aperture area	69
η_r	Receive antenna efficiency	69
η_H	Heterodyne efficiency	69
E_{r_0}	Peak amplitude of electric field at receiver aperture	70
ρ_d	Radial coordinate of image at detector plane	71
x_d	Cartesian coordinate of image at detector plane	71
y_d	Cartesian coordinate of image at detector plane	71
R_A	Received Airy disk radius	71
σ	Airy disk parameter	71
F_s	Receive telescope F-number	71
ω_t	Transmitter angular frequency	72
ω_l	Local oscillator angular frequency	72
L	Detector element half width	73
x	Scaled radial coordinate of image at detector plane	75
y	Scaled radial coordinate of image at detector plane	75
r	Ratio of detector half-width to Airy radius	75
ω_L	Local oscillator beam radius	76
t	Ratio of Airy disk to local oscillator beam radii	76
δ	Received beam misalignment angle	80
β	Received beam misalignment parameter	81
ρ_A	Radial coordinate of Airy image at detector	83
ω_A	Airy disk radius approximation	83
g	Gap distance between detector pixels	85
S_n	Maximum power from single pixel among n pixels	86
p_n	Probability that all received power is contained within n pixels	86
n	Number of pixels over which received image lies	86
$E\{S_R\}$	Expected value of the maximum received signal	86

Symbol	Page
$P_{disk}(\gamma)$ Total power in Airy disk	86
$P_{im}(\gamma)$ Total power in Airy image	86
v_r Target radial velocity component	91

Abstract

This research determines the minimum performance requirements of a ground-based infrared LADAR designed to detect deep-space satellites, and presents a candidate sensor design based on current technology. The research examines LADAR techniques and detection methods to determine the optimum LADAR configuration, and then assesses the effects of atmospheric transmission, background radiance, and turbulence across the infrared region to find the optimum laser wavelengths. Diffraction theory is then used in a parametric analysis of the transmitted laser beam and received signal, using a Cassegrainian telescope design and heterodyne detection. The effects of beam truncation and obscuration, heterodyne misalignment, off-boresight detection, and image-pixel geometry are also included in the analysis.

The derived equations are then used to assess the feasibility of several candidate designs under a wide range of detection conditions including daylight operation through cirrus. The results show that successful detection is theoretically possible under most conditions by transmitting a high-power frequency-modulated pulse train from an isotopic $^{13}\text{CO}_2$ laser radiating at $11.17\text{ }\mu\text{m}$, and utilizing post-detection integration and pulse compression techniques.

GROUND-BASED DEEP-SPACE LADAR FOR SATELLITE DETECTION: A PARAMETRIC STUDY

I. Introduction

Background

The mission responsibilities of US Space Command lie in the areas of space operations and aerospace defense (81:36). In support of these responsibilities, US Space Command controls a comprehensive network of space surveillance sensors known as the Space Surveillance Network (SSN). Although some of the 28 SSN sensors are capable of detecting objects in deep-space (from 5,000 km to about 40,000 km altitude), the only dedicated deep-space capability lies with the Ground-Based Electro-Optical Deep-Space Surveillance System (GEODSS) (81:42; 62:18). Since satellite detection by GEODSS is achieved through the detection of sunlight reflected off the satellite, GEODSS operation relies on clear weather, night-time conditions. This severe limitation means that each of the four currently existing GEODSS sensors is available for an average of only 14% of the time for surveillance tasks — a shortfall which has contributed to the widening gap between the estimated population of deep-space objects, and the SSN-monitored population (25:1). The current escalation in numbers of deep-space satellite systems, coupled with rising Soviet activity in geosynchronous orbit, and continued Soviet development of ASAT capability, now mandates increased deep-space surveillance (74:252; 58:19).

The majority of plans for deep-space capability improvements (30:Sec V,2; 58:38) have so far been aimed at increasing GEODSS track rates (number of different satellite detections per hour), while no reports were found which investigate

improved sensor availability. Attempts to improve GEODSS availability would have little utility, however, due to the inherent limitations of passive sensing at visible wavelengths. Clearly, an alternative detection method must be used to gain useful improvements in sensor availability under diverse weather and lighting conditions. Therefore, active detection techniques must be introduced. These techniques could be implemented for deep-space surveillance using conventional microwave radars, but the large size, high cost, and poor search capability of radars preclude them from serious consideration. An attractive alternative to microwave radar is infrared LADAR (*LA*ser *ra*DAR), which uses an infrared (IR) laser as the active source. LADAR advantages over microwave radar include smaller size, superior accuracy, and improved resolution (29:3; 12:1526; 73:37-2). Benefits of using IR over visible wavelengths include operation in daylight and successful detection under a diverse range of meteorological conditions.

Although LADAR technology has improved steadily throughout the past two decades, the application of LADAR techniques to satellite detection has been limited. 'Enhanced' satellites, equipped with retro-directive corner-cube reflectors for enhanced laser returns, have been successfully detected with LADAR on several occasions (38:1742; 54:77; 20:398). However, the only LADAR routinely used for 'unenhanced' satellite detection is the Firepond LADAR operated by MIT Lincoln Laboratory at Westford, Massachusetts (26:329; 77:148; 76:1). The major Firepond limitation for deep-space application is that 'unenhanced' detection has been limited to medium altitudes (below 10,000 km) (76:1). No evidence has been found of the successful demonstration of an operational LADAR for detecting 'unenhanced' deep-space satellites under adverse weather, daylight conditions.

Specific Problem

The viability of an alternative ground-based deep-space sensor with high availability requires investigation. The purpose of this research, therefore, is *to analyt-*

ically determine the minimum theoretical performance requirements for a ground-based, IR LADAR for deep-space satellite detection, and to select a candidate sensor design by matching minimum performance parameters with available technology. Where available technology cannot meet the required performance specifications, the corresponding technological shortfalls will be highlighted.

Scope and Limitations

The general research approach is limited to parametric analysis of a LADAR system which is capable of search, acquisition, and tracking of a deep-space satellite to provide range, direction, and velocity information. Specifically, the research analyzes the characteristics of the laser, optics, detector, target, background radiance, and atmospheric transmission. The effects on performance of weather, turbulence, and daylight are also included, along with a review of search and detection techniques, and scanning strategies.

The analysis does not consider LADAR mechanical construction, or detailed design of signal-processing circuitry beyond sub-system level. Furthermore, detection of satellites below 5,000 km altitude and above 40,000 km altitude is not considered.

Methodology

Investigation of the research problem is divided into four major subject areas: (1) LADAR techniques, (2) the infrared environment, (3) parametric analysis, and (4) candidate system design. Following a review of background literature in Chapter II, research results corresponding to the four subject areas are presented in Chapters III to VI, inclusive. Research conclusions and recommendations are then presented in Chapter VII. The sub-objectives of each chapter are outlined in the following paragraphs.

LADAR Techniques. This research phase reviews available LADAR techniques for long-range high-resolution LADAR. The four major research sub-objectives are as follows:

1. *Target Characteristics.* Determine the approximate size of deep-space satellites, and their typical IR reflectivity characteristics.
2. *Detection Methods.* Review the application of coherent and incoherent LADAR detection schemes, including the use of high-resolution focal-plane detector arrays.
3. *LADAR Technology.* Review the performance characteristics of currently available lasers, optics, and detectors suitable for LADAR applications.
4. *Target Acquisition.* Determine a suitable search scheme for deep-space target acquisition.

The Infrared Environment. The second research phase examines the major environmental characteristics which affect LADAR reception and IR propagation in the atmosphere. The three major research sub-objectives are as follows:

1. *Background Radiance.* Determine the level of background solar and thermal sky-radiance across the IR region.
2. *Atmospheric Transmission.* Determine the transmittance characteristics of IR laser beams through typical atmospheric aerosols for various weather conditions and slant paths.
3. *Other Propagation Effects.* Assess the influence of atmospheric turbulence and high-power beam effects on laser beam propagation through the atmosphere.

Parametric Analysis. The third phase in the solution process involves the development of all design parameter equations necessary to predict theoretical LADAR performance. Sub-objectives include the optimization of laser, optics, and detector characteristics to achieve maximum system efficiency.

Candidate Design. The final phase of research involves translation of the derived LADAR parametric equations into a candidate design based on the performance capabilities of current technology. The primary sub-objective is to determine whether the necessary laser, detector, optics, and processing technology is currently available to match the specified performance requirements.

II. Literature Review

Introduction

This chapter reviews background literature pertinent to this research. In particular, the review covers the topics of deep-space surveillance objectives, GEODSS, LADAR history, Firepond, and a brief summary of current LADAR technology.

Deep-Space Surveillance Objectives

The objectives of the US Space Command deep-space sensor network are defined by Gaposchkin as follows:

1. Support acquisition of new launches; especially foreign.
2. Monitor, identify, and quantify orbital maneuvers.
3. Maintain a catalogue of all targets in deep-space.
4. Support technique development and target identification. (25:1)

In fulfillment of these objectives, the SSN tracks a variety of orbiting space objects, such as active and inactive payloads, spent booster-rocket stages, and miscellaneous debris resulting from anomalous satellite events, such as explosions (18:306). SSN tracking data also helps in planning space launches and orbital maneuvers so that possible collisions are avoided (18:306).

Although SSN surveillance capability appears comprehensive, the resource-consuming objective of maintaining a catalogue of deep-space objects is difficult to achieve. Catalogue maintenance places growing demands on each sensor, commensurate with the rapid growth in deep-space population, which is projected to be 2,600 by the year 2000 (47:4). Furthermore, even the catalogued objects require frequent updates of their catalogued positions due to orbital maneuvers and perturbations.

If a catalogued position becomes outdated, the object is 'lost.' A common definition used for a 'lost' satellite is a catalogued item with an orbital element set greater than 30 to 60 days old, depending on the type of object (25:3). Table 1 provides a breakdown of 142 'lost' satellites, compiled by Taff for a selected day in 1986.

Table 1. Summary of Known, Lost, Deep-Space Satellites (Reproduced from (78:5))

<i>Object</i>	<i>Soviet</i>	<i>Non-Soviet</i>
Payloads		
Synchronous	13	32
Semi-Synchronous	6	1
Rocket Bodies		
Synchronous	8	8
Semi-Synchronous	2	11
Debris		
Synchronous	18	12
Non-Synchronous	29	2
TOTALS	76	66

GEODSS

The primary SSN sensor for deep-space surveillance is GEODSS (81:42). Four GEODSS sites are currently operational, with locations at Socorro, New Mexico; Maui, Hawaii; Taegu Air Base, South Korea; and Diego Garcia in the Indian Ocean. A fifth site is planned for location somewhere in the eastern Atlantic region (47:3). Each GEODSS site has two primary telescopes and one auxiliary telescope for sensing in the 0.3-0.86 μm band (47:18). General telescope characteristics are listed in Table 2 (63:129; 65:57-58).

Each telescope mount contains a sidereal drive, which maintains the telescope field-of-view fixed on the star background so that orbiting satellites appear as streaks of light on the sensed image (65:57). Using this method, objects with a visual

Table 2. GEODSS Telescope Characteristics

<i>Parameter</i>	<i>PRIMARY</i>	<i>AUXILIARY</i>
Diameter	1 m	40 cm
Field-of-View	2.1 degrees	6 degrees
Focal Length	218 cm	76 cm
Max Slew Rate	2 deg/sec	15 deg/sec
Pointing Accuracy	1.5 arc-second	1.5 arc-second
Scan Rate	2,400 sq. deg/hr	15,000 sq. deg/hr
Main Element	Ritchey-Chretien	Schmidt camera

magnitude of 15.5 are routinely tracked (33:586), while detection of fainter objects at magnitude 16.5 is possible under certain conditions (65:57).

Performance Limitations. The primary gauge of GEODSS performance is track rate (58:2). Although extreme nightly variations occur, peak track rates were reported in 1987 to be between 100 and 150 tracks per telescope per night (58:14). These rates could be considerably improved through software modifications and hardware replacement, but are ultimately limited by ambient light and weather conditions (58:1-2). Bright-sky conditions, such as twilight, or the 7-day period centered on the full moon, seriously affect GEODSS capability (78:7; 58:2). Additionally, tracking is not attempted when less than 1% of the night sky is clear. This weather condition often exists for 30% to 60% of available tracking time (47:5).

Availability. Koehler reports seasonal data for each GEODSS location concerning hours of darkness and the probability of cloud-free viewing (47:60). When data is averaged over all seasons and sites, an average expected value for *hours of darkness per night*, and *probability of clear skies* can be derived. These figures are 9.375 and 0.6, respectively. If a twilight period of two hours per night is considered unacceptable for operation, then the average available viewing time, limited by twilight and weather, is only 4.5 hours each night. If 91 'bright-sky' nights are then assumed to occur each year due to full moon conditions, average GEODSS availability during

hours of darkness is estimated to be 35%. This translates to an average *24-hour availability* of 14%. These figures do not account for the additional limitations due to solar illumination of the orbit, satellite viewing geometries, and system failures. However, the calculations do support several reports that, due to environmental restrictions on operation, GEODSS is not suited to providing time-critical surveillance support (58:20; 47:5; 30:Sec V.2).

Improvements. Clearly, sensor availability is the limiting factor in improving GEODSS track rate. Therefore, substantial improvement in GEODSS tolerance to adverse weather and high ambient light is required to meet tasking objectives. Indeed, one analysis of deep-space sensor performance recommends that GEODSS sensors be modified for 24-hour capability by shifting operation to the long-wavelength IR portion of the spectrum (30:Sec V.3). This method could use a passive IR sensor to detect object thermal radiation, and is attractive due to the lower levels of background sky radiance at IR wavelengths when compared to visible wavelengths (80:49). However, if the object is space debris, or an inactive payload, the temperature difference between object and background may be insufficient for reliable passive detection.

A more reliable detection scheme could be implemented by using an active IR laser source to irradiate the target. The detection decision would be then based on the relative level of received laser power reflected from the target. Any additional IR signal received due to the object's thermal radiation is, therefore, a 'bonus' in the active scheme (23). Processing of the received target signal can also provide additional target information such as range, velocity, and rotation rate (26:329; 28:976).

Advantages of using IR wavelengths over visible wavelengths include higher atmospheric transmission, lower scattering and lower scintillation (intensity fluctuations) (12:1526). When compared to microwave sources, IR laser sources provide superior angular, range, and Doppler-frequency (velocity) resolution (12:1526; 73:37-2).

LADAR History

The use of lasers for satellite detection was first demonstrated in 1964, when a Q-switched ruby laser (visible wavelength — 694.3 nm) was used to determine range to the Beacon Explorer B satellite within a precision of a few meters (20:398). The satellite was fitted with retro-reflectors for enhanced signal reflection, and detection was achieved at night. Daytime detection using a ruby laser was subsequently demonstrated in 1967 (38:1743). Since then, at least 14 reflector-equipped satellites have been placed in orbit, providing reference points for a variety of geodetic studies (20:398; 70:391). Satellite detection at IR wavelengths was further assisted by the launch of the Laser Geodynamic Satellite (LAGEOS) in 1976. LAGEOS was specifically designed to support scientific applications, and consists of a 60-cm diameter sphere, studded with 426 reflectors (20:398). Four of the reflectors are made of germanium for long wavelength IR use, while the remainder are for operation in the visible region (77:152). For LADAR applications, the launch of LAGEOS into a stable, well-defined orbit at 5,900 km altitude provides a reference point in inertial space for LADAR calibration purposes (20:398; 77:152).

Although tracking of enhanced satellites is routinely performed, evidence of unenhanced detection is scarce. One example system is the Maui Optical Tracking and Identification Facility (MOTIF), which uses a ruby laser “for space object illumination or to provide range information on selected targets” (1:22). The only example found in the literature of an operational satellite-tracking IR LADAR is the Firepond LADAR operated by MIT Lincoln Laboratory (31; 32; 10).

Firepond LADAR

The Firepond LADAR project commenced development in the late 1960s with primary emphasis on satellite tracking and identification (26:327). Drawing from CO₂ laser and IR detector research at Lincoln Laboratory, a LADAR was developed by the late 1970s into an “automatic angle, range, and Doppler frequency tracking

coherent laser radar operating at a wavelength of $10.6 \mu\text{m}$...capable of tracking and recording a variety of data on both enhanced and *unenanced low earth orbiting targets*" [emphasis added] (77:148). The characteristics of the Firepond LADAR are taken from Gschwendtner et al. and summarized in Table 3.

Table 3. Firepond LADAR Characteristics (Extracted from (26:329))

<i>Parameter</i>	<i>Specification</i>
Wavelength	$10.6 \mu\text{m}$
Aperture	1.2 meters
Beamwidth (λ/D)	$\approx 10 \mu\text{rad}$
Rayleigh Range (D^2/λ)	100 km
Beam Diameter (at 1000 km)	10 meters
Doppler Coefficient	2 kHz/cm/sec
Peak Power	1 to 10 kW
PRF Continuously Variable	20 to 200 pps
Pulse Width Continuously Variable	10 to 1 ms

Major Firepond accomplishments are reported by Gschwendtner et al. as follows:

1. Development of a high-frequency-stability, long-range, coherent IR radar.
2. Demonstration of monopulse angle tracking of enhanced and unenhanced satellite targets.
3. Determination of target center-of-gravity motion and rotational dynamics using Doppler measurements capability.
4. Generation of one-dimensional pseudo-images from narrowband time-Doppler-intensity data. (26:329)

Current LADAR Technology

In principle, an increase in LADAR detection range from low altitude to deep-space appears to affect only the free-space 'loss' term in the LADAR range equation.

However, implementation is not so simple due to limitations in laser transmitter power, and the consequent need for a very small divergence laser beam to provide high irradiance at long range (4:53). This narrow-beam requirement increases the need for an accurate *a priori* orbital prediction for the object, so that acquisition/search time is reduced. The narrow-beam requirement also means that very precise pointing and tracking of the laser/telescope combination is essential, so that the object remains in the telescope field-of-view.

Technological research and development has produced many LADAR improvements during the last decade. Advances in laser technology have been considerable, with current IR lasers exhibiting high power, stable operation, and narrow beam divergence (31; 35; 60; 66). The optics and detector components needed to handle high levels of laser power and provide long-range resolution have also undergone extensive development (7; 11; 38; 64). Finally, the acquisition, tracking, and pointing sub-systems have been adapted and refined from microwave radar systems to accommodate the special needs of electro-optical systems (80). The detailed capabilities of current LADAR technology is the subject of further analysis in Chapter III, with emphasis on specific deep-space requirements.

Summary

The current deep-space surveillance network is not achieving the track rates necessary to accomplish all operational objectives. In particular, although GEODSS detection performance is sufficient for deep-space surveillance, availability is severely hampered by adverse weather and bright-sky conditions. An attractive alternative to the GEODSS method of passive sensing in the visible region uses an IR laser to irradiate the target. Although active IR methods have been implemented in the Firepond LADAR, capability is limited to detection of unenhanced satellites at low altitude. Extension of this low-altitude capability to deep-space appears promising with the benefit of recent developments in IR laser, detector, and optics technology.

III. LADAR Techniques

Introduction

This chapter describes various LADAR techniques suitable for a long-range LADAR, and reviews the currently available technology for major LADAR elements. In particular, the typical characteristics of deep-space targets are discussed, followed by an outline of detection methods suitable for these targets. Current technology is then reviewed for laser transmitters, detectors, and optics. Finally, a target acquisition scheme is proposed to optimize the target search phase of LADAR detection.

Target Characteristics

The distribution of deep-space objects which are of primary interest to this research can be categorized according to three orbital classes: geosynchronous, semi-synchronous, and highly-elliptical. Figure 1 provides a pictorial representation of each orbital class. Successful detection of targets from all three classes depends on, among other factors, the relative viewing geometry between the ground-based sensor and the target object. For example, only a fraction of the geosynchronous population are 'visible' from a fixed sensor site all of the time, while the remaining fraction may never be visible from the same site due to obscuration by the earth. Conversely, objects with much shorter orbital periods (lower altitudes) may be visible several times daily for short durations from a single site, depending on the exact orbital characteristics.

Clearly, a global network of sensors is required to provide adequate coverage of the majority of deep-space objects. The target range from any one of these sensors is then dependent on the relative position of the object along its orbit. Although targets in the highly-elliptical orbit class can occupy altitudes as high as 40,000 km or more, successful orbit predictions can be performed from observations taken closer to

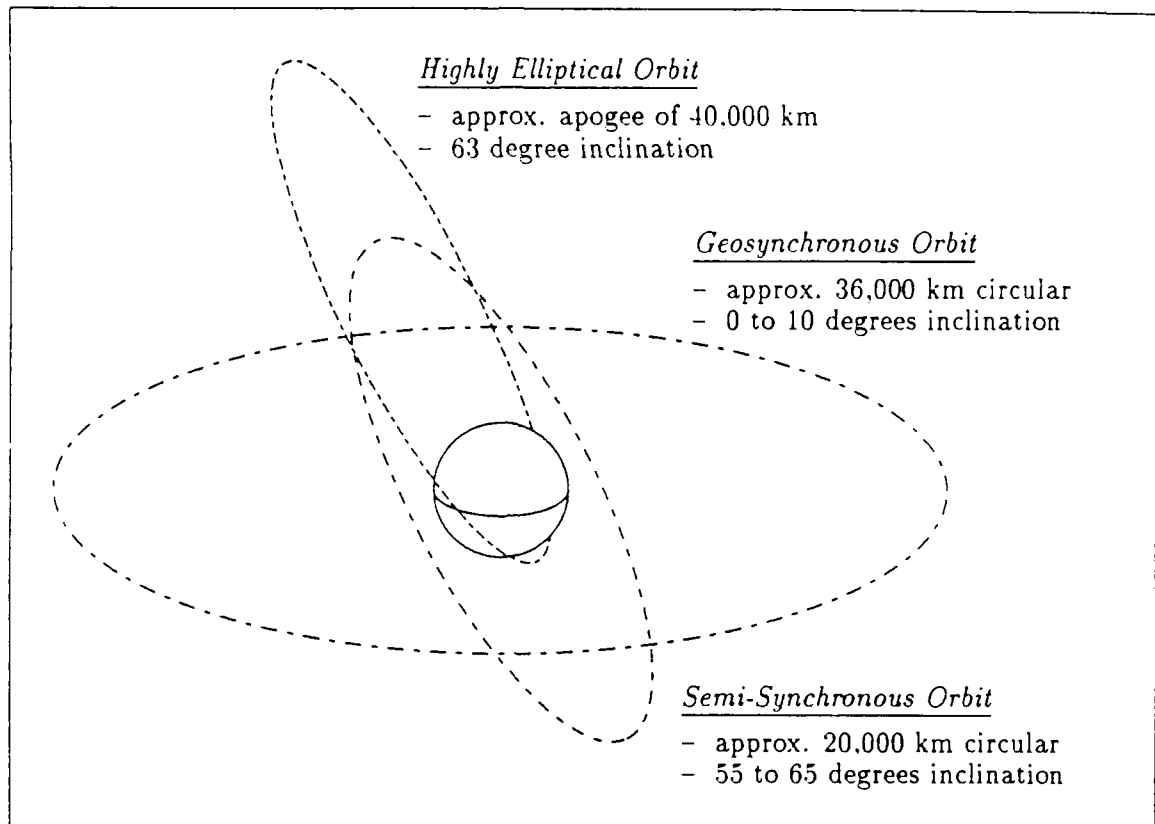


Figure 1. Classes of Orbits for Deep-Space Objects

the target's perigee, which is only a few hundred kilometers altitude. Assuming that observations for this class are not essential near apogee, the maximum target range experienced by a deep-space sensor would then occur when observing geosynchronous objects.

For an equatorial sensor which is situated coincident with the orbital sub-point of a geostationary satellite (zero degree inclination), the target range is nearly 36,000 km. In general, however, the satellite-sensor geometry is more complicated, as shown in Figure 2. Based on GEODSS site characteristics, the sensor may be located at latitudes of up to 36 degrees (30:III-22), while the satellite orbit may be inclined by several degrees to the equatorial plane. Since the target range is also a function of the satellite sub-point, a wide range of satellite-sensor geometries is possible.

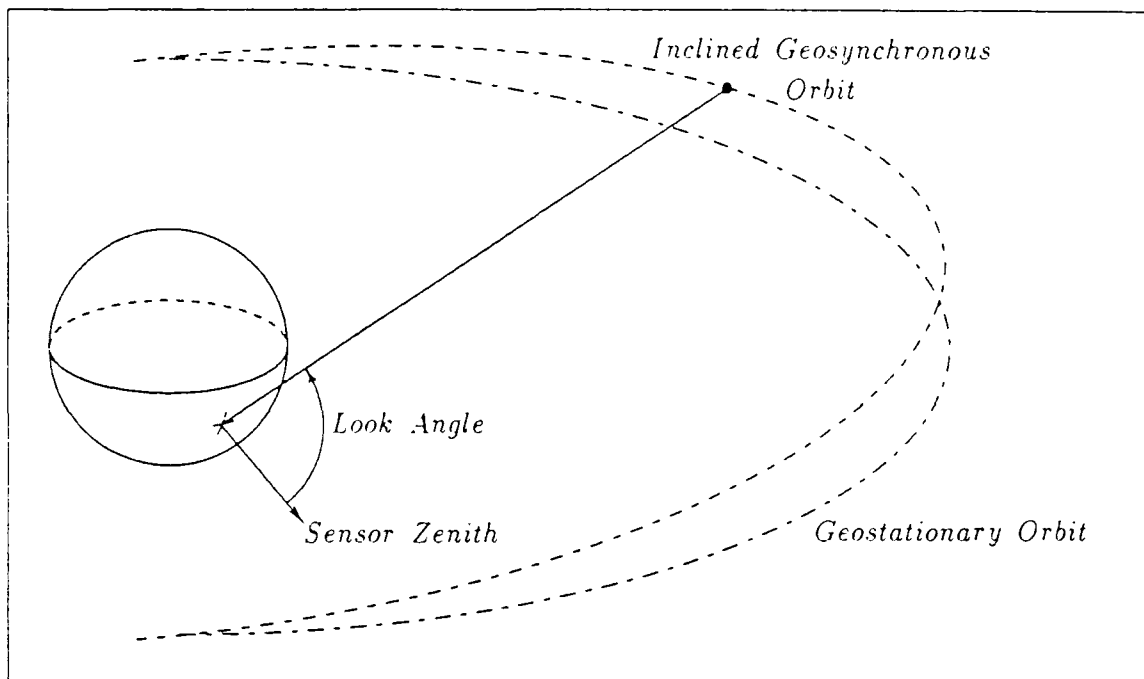


Figure 2. Typical Sensor-Target Viewing Geometry

The limits of sensor coverage can be defined in terms of *maximum look angle*, which is the average maximum sensor viewing angle for successful target detection, measured from the sensor local zenith. Although actual values of maximum look angle for successful detection of a specific target will vary due to atmospheric effects, background radiance, and target characteristics, an average maximum sensor look angle is appropriate for design calculations. For example, GEODSS maximum look angles are generally less than 60 degrees (30:III-22). This value will be adopted as a minimum design objective to ensure adequate sensor coverage. This equates to target ranges for geosynchronous objects of between 36,000 and 40,000 km.

Apart from target range, the other major target characteristic that affects detection is the target's *LADAR cross-section*, which is a function of target size and orientation, surface shape and roughness, and surface reflectivity. For LADAR detection purposes, target surfaces may be classified as either *specular* or *diffuse*. A specular target is composed of surfaces which are 'flat' at IR wavelengths, and reflect incident radiation preferentially in a specific direction. A diffuse, or rough, target is

composed of many independent scatterers and reflects incident radiation equally in all directions.

In general, objects such as satellites may be modeled as hybrid targets, exhibiting IR reflectivity characteristics which include both diffuse and specular components. In terms of LADAR cross-section, the addition of a relatively small diffuse reflectivity component to a purely specular target surface causes the overall reflected signal to resemble that from a purely diffuse target (6:43). Therefore, without loss of generality, this analysis assumes that typical deep-space targets are characterized by surfaces with a purely diffuse IR reflectivity. Using a diffuse spherical target model, with diameter much greater than the incident wavelength, the LADAR cross-section, σ_{lcs} , may consequently be written as follows (48:201B):

$$\sigma_{lcs} = \frac{8}{3} \rho_{ir} A \quad (1)$$

where ρ_{ir} is the IR reflectivity of the target surface, and A is the projected physical target area.

Typical target cross-sections can be determined from typical values of A and ρ_{ir} . The size and shape of deep-space objects varies considerably, with target characteristic dimensions ranging from 1 to 30 meters (84:37). For detection analysis purposes, a spherical target with a diameter of 3 meters is therefore assumed as typical.

The IR reflectivity of deep-space objects also varies, depending on the composition of target surface material. For satellites, surface materials include solar cell components, optical solar reflectors, multi-layer insulation, surface paints, and heat radiators (2). The majority of such materials are designed for satellite thermal-management purposes, and are characterized by high reflectivity in the optical region and high emissivity in the IR region, so that heat absorption and retention is minimized. Unfortunately, the goals of satellite thermal management design oppose the

desire for LADAR targets with high IR reflectivity. Accordingly, typical IR reflectivity values for thermal control surfaces are only about 20% (3:9).

Substituting $A = \pi(1.5)^2$ and $\rho_{ir} = 0.2$ into Equation (1) yields a value of $\sigma_{lcs} \approx 4 \text{ m}^2$, which is suitable for further analysis of design feasibility. With typical examples of target orbits, maximum range, and LADAR cross-section thus defined, methods of long-range, high-resolution, LADAR detection will now be discussed.

LADAR Detection Methods

LADAR systems may be categorized according to receiver design as either *direct detection*, or *coherent detection* systems. In the direct detection scheme, detection decisions are based on the results of a direct measurement of received signal energy. Using a pulsed transmitter and measuring the pulse round-trip time gives the target range, while the addition of shaft-position encoders on the receiver telescope mount allows calculation of the target's angular position. The major benefits of direct detection are simplicity of hardware design and relaxed requirements for stringent laser frequency stability. However, high levels of background noise severely degrade the performance of direct detection systems.

In coherent detection schemes, the received signal is mixed with a local oscillator (LO) signal on the photodetector surface. Photocurrent is produced in the detector at a beat frequency equal to the difference between signal and local oscillator frequencies. Normally, the local oscillator is offset from the transmitter frequency by an intermediate frequency (IF), so that the photocurrent beat frequency equals the IF frequency plus any Doppler shift imposed by target radial velocity. This coherent detection scheme is known as *heterodyne detection* and is illustrated for a pulsed system in the LADAR block diagram shown in Figure 3. If a single laser is used to provide both transmitter and local oscillator signals, the system is referred to as an *offset homodyne* scheme (49:153); if no offset is used, the system is simply called *homodyne* detection (24:318).

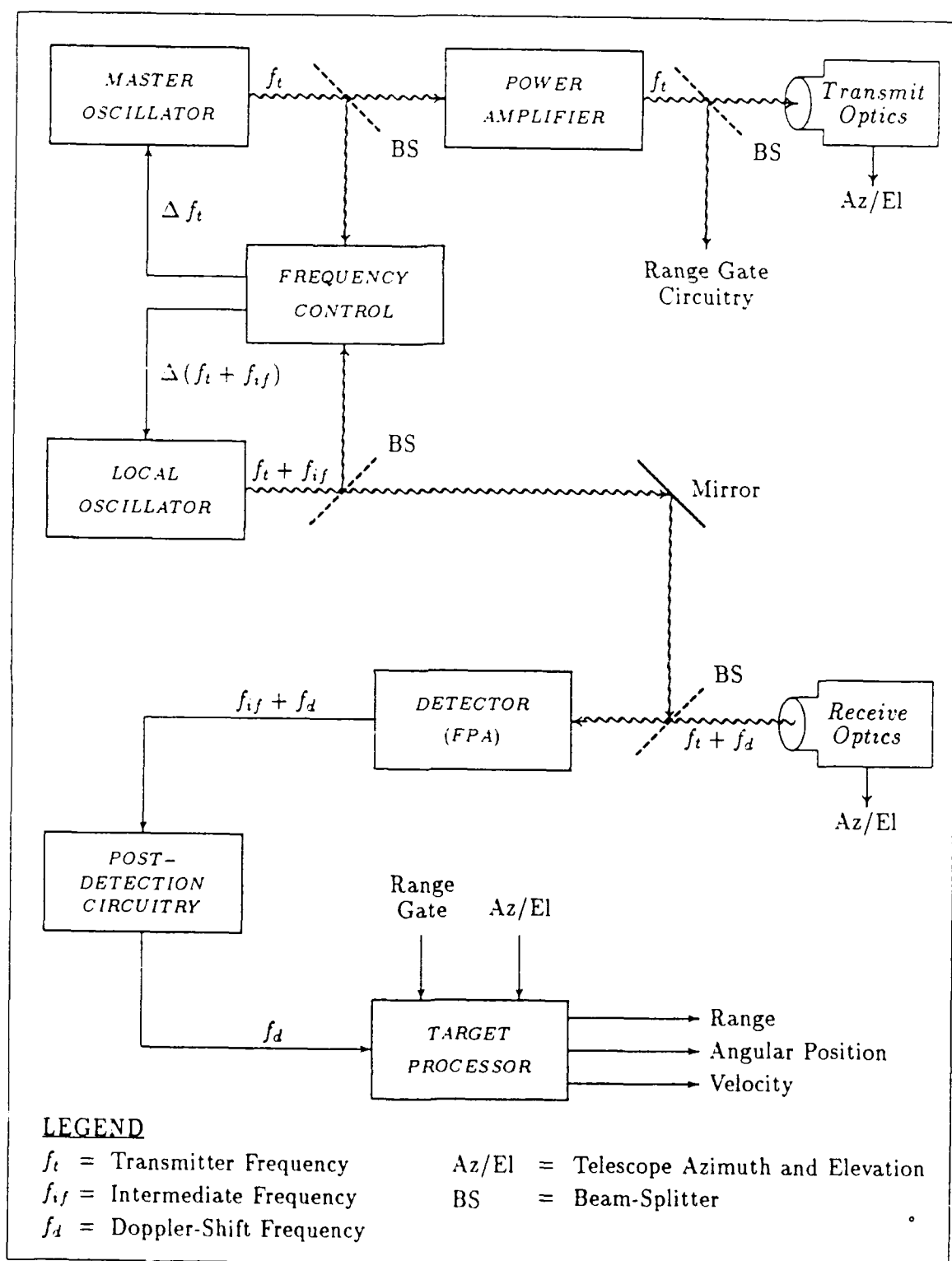


Figure 3. Block Diagram of Pulse-Doppler LADAR using Heterodyne Detection

Figure 3 also shows the use of range gates for signal timing. Range gates are used to control receiver-on time so that detector output is only enabled during the period in which a transmitted pulse is expected to return. For example, the pulse round-trip time to a target at 36,000 km range is about 240 milliseconds. Allowing for atmospheric propagation delays, optics delays, variation in the target range, and a typical pulse duration of 1 μ s, the receiver might be triggered 'on' after a delay of 239 ms from pulse transmission, and then triggered 'off' after a further 2 ms delay. This method prevents erroneous detections during the 239 ms between pulse transmission and the earliest expected pulse return, and allows more efficient searching of pre-defined range cells. The improvement in detection performance through the use of range gates will be further discussed in Chapter V.

One major element normally found in the post-detection circuitry shown in Figure 3 is the *matched filter*. The matched filter is also triggered by range gate signals and is the optimum filter when the signal is corrupted by additive white Gaussian noise (73:3-8). The ideal matched filter is usually approximated as a filter with a frequency response matched to the spectrum of the transmitted pulse (88:72). A bank of such filters, with bandpasses which are contiguous in the frequency domain, provides ease of Doppler-shift measurement and closer matching of the filter to the received Doppler-shifted signal.

The main benefits of coherent detection schemes are additional target information through measurement of Doppler shift, and the capability of obtaining quantum-limited detection with high background noise (73:37-4). Heterodyne systems, therefore, may be "several orders of magnitude more sensitive than a direct detection system which is typically background noise or amplifier noise limited" (27:93). For a typical 10.6 μ m LADAR, heterodyne reception should allow detection of signals which are 100 to 1000 times weaker than the equivalent direct detection receiver (17:290). Further sensitivity improvements are possible by transmitting a train of pulses and then integrating the received signal over several pulses.

Pulse Compression. Improvements in range resolution can be gained by using short pulse widths; however, many high-power lasers are characterized by long pulses (10–1000 μs) of high energy (50–300 J). A common technique used to achieve high range-resolution with long pulses is *pulse compression* (72:421). The simplest pulse compression technique uses frequency modulation (FM) to generate a transmitter pulse of constant amplitude with linearly increasing frequency throughout the pulse, also known as *chirp*. The matched filter of Figure 3 then acts as a pulse compression filter by adding a signal time delay which is inversely proportional to frequency. The added time delay allows the higher frequencies in the pulse's trailing edge to 'catch up' to the leading edge so that the wide, low-amplitude received pulse is compressed into a short, high-amplitude pulse (73:422).

A typical implementation of the pulse compression filter uses a surface acoustic-wave device made of a piezoelectric material such as lithium niobate (36:439). If the FM bandwidth in the transmitted pulse is B_{FM} , with pulse width τ , then the ratio of uncompressed pulse width to compressed pulse width — or *compression ratio* — is τB_{FM} . The peak power of the received pulse is also increased by the compression ratio τB_{FM} after passing through the filter (72:423).

The pulse compression method may also be used with the post-detection integration scheme. This allows high resolution to be combined with the high sensitivity possible through using coherent detection. Although several advantages are gained by using coherent detection schemes, some disadvantages exist. The primary drawbacks are critical optical alignment tolerances, hardware complexity, and stringent stability requirements for the transmitter and local oscillator. Nevertheless, for the extremely long ranges under consideration, high receiver sensitivity is of prime importance in LADAR design. For this reason, and because the target's radial velocity component is available from the measured Doppler shift, the LADAR system of Figure 3 will be adopted as the basis for further system analysis. The performance requirements of each LADAR system element will now be examined in detail.

LADAR Transmitters

The characteristics required of a laser which is suitable for long-range coherent IR LADAR applications include single-frequency operation, high pulse energy, high frequency stability (both inter-pulse and intra-pulse), and high pulse repetition rate. Several transmitter configurations are currently in use, with the majority utilizing Transversely-Excited Atmospheric-pressure carbon dioxide (TEA CO₂) lasers as the radiation source, at a wavelength of 10.6 μm (88:83; 39:2). Two other important sources exist for LADAR transmitters: Neodymium-doped Yttrium Aluminum Garnet (Nd:YAG) at 1.06 μm (27:96), and Deuterium Fluoride (DF) at about 3.8 μm (9:8).

Due to moderate atmospheric absorption at 10.6 μm , two variants of the ordinary CO₂ laser have been recently considered. The first uses isotopically-substituted ¹³C¹⁶O₂ in lieu of ¹²C¹⁶O₂ in the lasing gas mixture, which produces radiation at about 11.1 μm (57: 31; 27). Since carbon-13 abundance in the atmosphere represents only 1.1% of the total CO₂ concentration (87:5-61), self-absorption is greatly reduced at 11.1 μm . Performance from ¹³C¹⁶O₂ lasers is reported to equal that of ¹²C¹⁶O₂ lasers (57:106).

The second CO₂ variant uses a frequency-doubling crystal such as Tl₃AsSe₃ or AgGaSe₂ to convert CO₂ 9-11 μm radiation to 4.5-5.5 μm radiation (56; 27). Conversion efficiencies of 40%, or higher, for frequency-doubled CO₂ are advocated (27:99; 56:6).

Although several other laser sources are currently under consideration for LADAR use, the CO₂, Nd:YAG, and DF lasers represent the most technologically-mature examples of high-power pulsed IR LADAR transmitters currently available. The characteristics of each source will now be described individually.

CO₂ Transmitters. CO₂ LADAR technology is the oldest and most mature of the sources under consideration (88:83). High electrical efficiencies of around 20% are

achievable, which significantly reduces power generation and handling requirements when compared to other systems. The output pulse from a TEA CO₂ laser usually consists of a short, high-amplitude spike of 30 to 200 ns duration, followed by a long, low-amplitude 'tail' of 1 to 5 μ s duration (52:74). Since ideal LADAR pulse characteristics include high energy and short duration, the presence of the long tail in the TEA CO₂ pulse is undesirable. Recent experiments have been performed successfully with intra-cavity SF₆-He saturable-absorber cells to greatly reduce the tail duration without loss of peak pulse power (52:77).

For high-power applications, several different laser arrangements are possible such as hybrid TEA, injection-locked TEA, and Master Oscillator-Power Amplifier (MOPA) configurations. The hybrid TEA set-up consists of a TEA gain section and a low pressure continuous-wave (CW) section in a common optical cavity (17:290; 60:149). Although good inter-pulse frequency stability is achieved with this system, output pulse energy and pulse repetition rates are limited due to saturation of the CW section, and the onset of heating and acoustic effects (60:149-150).

The injection-locked technique uses an external low-power CW oscillator as an injection source into a TEA cavity. In this case, laser output frequency is controlled by the TEA cavity. Mode selection in the TEA section only requires a small injected signal when the difference between TEA tuned frequency and injection frequency is small (61:41). Therefore, careful frequency control between the TEA section and the injected signal is required.

Additional problems exist with injection-locked systems in the form of intra-pulse frequency instability, or 'chirp'. Frequency chirp results primarily from a phenomenon known as laser-induced medium perturbation (LIMP) (32:56; 66:62). The origin of LIMP lies in "differential heating between lasing and non-lasing levels" (32:56), which gives rise to density variations in the lasing medium; the resultant change in medium refractive index causes intra-pulse chirp on the order of a few hundred kilohertz (32:56).

The MOPA configuration consists of a low-pressure master oscillator operating at low pulse energies, which is then directed into a multi-pass TEA amplifier configured as an unstable resonator (60:151; 32:57). MOPA configurations have several advantages over the previous systems and are characterized by low levels of frequency chirp, high gain, and improved control of pulse width and shape (32:57; 66:63). For these reasons, MOPA systems are the preferred configuration for moderate to high-power systems, exhibiting pulse repetition rates of several hundred pulses per second, with typical pulse energies of 2 to 3 joules, and pulse widths of 1 to 5 μ s (66:63; 32:59; 60:151).

Higher pulse energies with longer pulse widths can be obtained from the amplifier by using different laser excitation techniques. Using an electron-beam sustained discharge in a $^{13}\text{CO}_2$ amplifier, for example, Moody et al. report a pulse energy of 200 J and pulse width of 30 μ s (57:102).

Nd:YAG Transmitters. Pulsed Nd:YAG lasers of moderate to high-power have been used extensively in a variety of applications for many years. Unfortunately, the "poor transverse-mode quality and broad spectral width typical of Nd:YAG lasers" (27:97) renders them poor candidates for high-resolution LADAR systems. Additionally, atmospheric scintillation is most severe at shorter wavelengths (88:83), reducing the probability of reliable LADAR operation at 1.06 μ m.

DF Transmitters. DF lasers have undergone considerable development in recent years, and have been implemented successfully in ranging applications, with peak powers above 2 MW and pulse lengths less than 100 ns (9:8). However, DF lasers normally operate in multi-line mode, with power divided over about 32 discrete lines (42:70). Single-line operation is possible, but at conversion efficiencies of around only 20% of multi-line power (67:13). Since reported repetition rates are also low at around 60 Hz (9:11), DF lasers require further scaling improvements to warrant serious consideration for high-power LADAR application.

Detectors

As LADAR transmitter technology has evolved and improved, great advances in IR detector technology have also been made. The single detector elements used in the late 1950s were replaced by linear detector arrays in the 1960s and early 1970s, with two-dimensional focal plane arrays (FPAs) becoming state-of-the-art in the late 1970s (16:60). Since then, FPA development has concentrated on improved manufacturing techniques and array uniformity, and fabrication of higher array densities. For LADAR applications, higher spatial resolution requires a higher density of FPA elements, while reliable detection requires a highly uniform detector responsivity across all FPA elements.

If linear arrays are used, some form of mechanical scanning is usually required to cover the desired field-of-view. However, the use of two-dimensional FPAs allows the array to 'stare' at a scene for a fixed time before moving, or 'stepping', to the next scene. The 'step-staring' method, which is adopted for this analysis, greatly simplifies LADAR design since precise mechanical scanning of the field-of-view is no longer required, while sensitivity is increased from longer signal integration times (16:61).

An additional detector requirement for use with high-speed LADAR targets is high bandwidth. For the wavelengths and radial velocity components of the targets under consideration, the detector must be able to respond to a maximum IF bandwidth of about 2 GHz. Fortunately, FPAs are routinely fabricated with bandwidths which meet this requirement (64:53).

The majority of detector advances have so far been concentrated on the wavelength regions corresponding to the two major IR atmospheric transmission windows at 3-5 μm and 8-12 μm . However, a significant decrease in available detector performance exists when moving from short to long-wavelength detector operation. For example, state-of-the-art FPA technology for visible wavelengths consists of an array of 2048 \times 2048 elements; at 3-5 μm , current array limits are 512 \times 512 elements,

while the 8-12 μm region is currently limited to 128×128 elements (22:15). Detector element sizes for these arrays vary from $10 \mu\text{m} \times 10 \mu\text{m}$ to $50 \mu\text{m} \times 50 \mu\text{m}$, depending on the material used (22:13; 21:74).

Various FPA materials, integration techniques, signal multiplexing, and data processing methods are in use or are being developed for IR detectors. The primary configurations currently in use for the 3-5 μm band are made from $\text{Hg}_{1-x}\text{Cd}_x\text{Te}$, InSb , PtSi , or PbS , while for the 8-12 μm band, only $\text{Hg}_{1-x}\text{Cd}_x\text{Te}$ has been developed to a sufficient level (11:114). The value of x in the $\text{Hg}_{1-x}\text{Cd}_x\text{Te}$ material is varied to achieve a desirable material bandgap, detector cut-off wavelength, and peak responsivity. For example, a value of $x = 0.205$ for a detector cooled to 77 °K provides a material with quantum efficiency exceeding 85% (with anti-reflective coating), cut-off wavelength of 11.7 μm , and peak responsivity at 10.6 μm (64:52).

Two-dimensional FPAs are made using both Charge-Coupled-Device (CCD) and Field-Effect-Transistor (FET) switches to address the detectors, with both types allowing full two-dimensional multiplexing (11:114; 22:15). However, two practical limitations exist for staring FPAs which arise from finite CCD storage capacity and data readout time. These limitations are reflected in a specified 'maximum FPA stare time' and 'maximum data output rate' for FPAs. Typical values for maximum stare times are 200-2000 μs for the 3-5 μm band, and 5-50 μs for the 8-12 μm band, while typical maximum output rates are reported to be about 10 MHz for the 3-5 μm band and 2 MHz for the 8-12 μm band (11:115).

Optics

The purpose of LADAR optics is to efficiently deposit the maximum amount of transmitter energy onto the target, and then to efficiently focus the maximum amount of reflected signal from the target onto the detector. The tasks of transmitting and receiving energy in this manner need not be performed by the same set of optics, but is often performed with one transmit/receive telescope due to reduced

cost and complexity. On the other hand, coherent LADAR performance is significantly improved in terms of signal-to-noise ratio by using a receiver aperture which is up to three times larger than the transmitter aperture (83:117).

The aperture used in IR LADAR can be considered to be the IR equivalent of an antenna at microwave frequencies. In the IR case, several reflectors and/or lenses are used in a telescope configuration, with the detector or FPA situated at the telescope's effective focal length. Additional beamsplitters, mirrors, and lenses are used to direct laser output radiation out through the telescope in much the same manner as microwave feed-horns. If a single telescope is used for both the transmit and receive functions, a system of mirrors is used as a 'transmit/receive' switch to alternately direct laser energy out through the telescope during the transmit cycle, and direct received radiation onto the detector during the receive cycle.

Telescope configurations vary widely; however, analyses have shown that the best performance is obtained from the Cassegrain configuration (34; 85). In particular, the aplanatic version of the Cassegrain design — the Ritchey Chretien configuration — is favored for its compactness, superior alignment, and low aberration characteristics (34:161). An example of such a design is illustrated in Figure 4, showing a typical Cassegrainian arrangement. Typical Ritchey-Chretien dimensions are shown in Table 2 in Chapter II for the GEODSS main telescope. Diameters of secondary mirrors for such telescopes range from 20% to 35% of primary mirror diameters (44:979), which results in partial obscuration of the signal. This effect will be examined in detail in Chapter V.

Primary mirror diameter is the limiting factor in manufacturing large telescopes for high-resolution applications. The fabrication of mirrors larger than 2 to 3 meters is best performed by first making several smaller mirror segments, and then assembling them into a single element afterwards (38:58). A prime example of this technology is the Hubble Space Telescope mirror, which has a diameter of 2.4 meters and was made as a welded assembly of ultra-low expansion fused-silica (38:58).

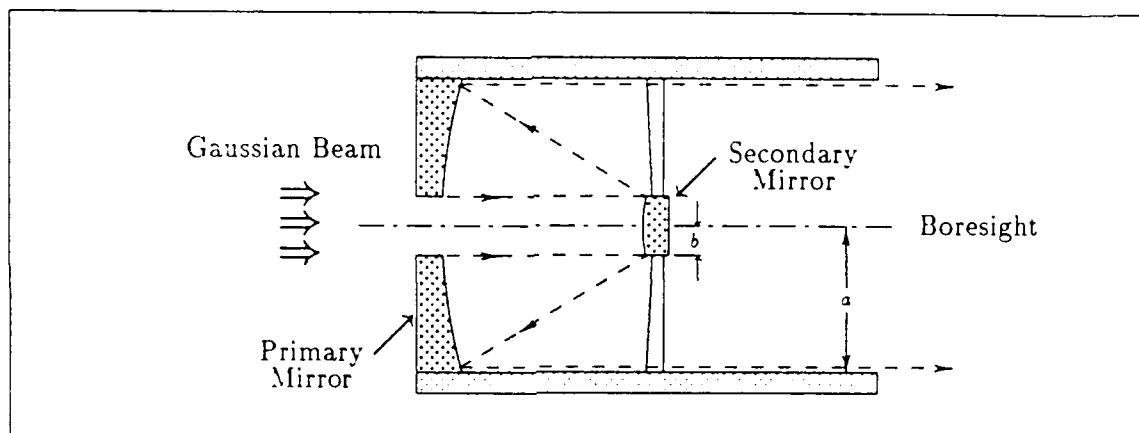


Figure 4. Cassegrainian Telescope Configuration

One other limitation encountered when designing LADAR optics is possible damage of optical surfaces when using high-power transmitters. For this reason, care must be taken to avoid maintaining high-power laser output as a small diameter beam when passing through lenses or reflecting off mirrors. For example, experiments have shown that surface reflectivity of copper and molybdenum mirrors is altered when CO_2 laser irradiance exceeds 1.2 GW/cm^2 (79:415).

Acquisition, Tracking, and Pointing

Acquisition, tracking, and pointing (ATP) functions of a LADAR system consist of three related tasks. *Acquisition* involves searching of a specific volume in target space with the aim of identifying a suitable target. *Pointing* involves the accurate positioning of the telescope boresight, or instrumental line of sight (LOS), in the same direction as the target LOS. Therefore, *pointing error* can be defined as the average difference between instrumental LOS and target LOS (80:40). Using the same terminology, *tracking* involves minimizing any variation in pointing error over time.

The LADAR's ability to perform effective pointing and tracking is largely determined by the quality of electro-mechanical control systems used to position the telescope and control the various beam-steering mirrors. Several design concepts

exist to perform these functions, including inertial stabilization, mirror stabilization, gear-driven gimbals, momentum wheels, shaft-angle encoders, active structural elements, and thermal control sub-systems. Detailed discussion of these topics is beyond the scope of this research and is comprehensively treated by Ulich, Masten and Hilkert, and Stockum et al. (80; 51; 75). Additionally, a detailed analysis of disturbances such as wind, seismic, gyroscope noise, electronics noise, and atmospheric turbulence is performed by Merritt and Meline (55).

While tracking and pointing performance is primarily an electro-mechanical design problem, selection of an acquisition scheme is a fundamental step which affects the choice of detector, optics, and transmitted waveform characteristics. In the case under study, the choice of a staring FPA and pulsed waveform to obtain high resolution and sensitivity places limits on the number of suitable acquisition methods. Also, the long round-trip time of at least 0.24 seconds to geosynchronous orbit for transmitted pulses implies a relatively long search time for each stage of the step-stare sequence, assuming only a single telescope is used.

However, search time could be reduced if two telescopes are fixed to the same mount, with independent LOS control systems. The first 'master' telescope would perform as transmitting antenna, and be 'pointed-ahead' along the search path by an angular distance of θ_{lead} . The other 'slave' telescope, configured as receiving antenna, would always lag the transmitter telescope position by θ_{lead} throughout the step-stare acquisition phase. In this manner, the 'stare' process is being performed by the receiver telescope while several pulse trains are 'in-flight'.

The determination of θ_{lead} can be written as a multiple of the receiver telescope field-of-view, which is equivalent to a multiple of the number of steps in the step-stare sequence. That is, if the time of flight for one pulse is expressed as $2R/c$, where R is the target range, and c is the speed of light, and the total waveform duration is denoted by T , then

$$\theta_{lead} = \frac{2R}{cT} \alpha_r \quad (2)$$

where receiver processing and telescope stepping delays have been ignored, and α_r is the receiver angular field-of-view.

To alleviate interference problems associated with backscatter of in-flight waveforms, variations in pulse transmission rate can be implemented in a similar way to PRF switching or jitter in microwave applications. With this refinement, each transmitted waveform is given a unique pulse spacing which is synchronized with receiver range-gate circuitry. Therefore, the receiver only locks-on to the expected synchronized return waveform.

This 'master-slave' acquisition method has the potential to dramatically reduce search times when compared with a single-telescope design. The actual search time is limited primarily by the stare period, which depends on the duration of the transmitted waveform. An additional benefit gained from using this method is the potential to gain performance improvements through selection of a receiver aperture which is larger than the transmitter aperture.

Summary

This chapter has examined the various LADAR techniques available for design of a ground-based, deep-space LADAR. Deep-space target characteristics have been examined, with selection of the following target specifications for further analysis of design feasibility:

$$\text{Maximum Target Range} = 40,000 \text{ km}$$

$$\text{Maximum Look Angle} \geq 60 \text{ degrees}$$

$$\text{LADAR Cross Section of Target} = 4 \text{ m}^2$$

Various detection methods have been reviewed, with the heterodyne detection method selected as the optimum LADAR choice due to superior receiver sensitivity, and the availability of Doppler shift information. Further sensitivity improvements

are possible by performing post-detection integration over several transmitted pulses, while range resolution and received pulse power can be dramatically improved using pulse compression techniques. A general block diagram of the proposed LADAR system is shown in Figure 3.

High power lasers suitable for long-range IR LADAR were studied, with the following types highlighted as technologically-mature, high-power LADAR transmitters:

Nd:YAG @ 1.06 μm
DF @ 3.8 μm
Frequency-doubled $^{12}\text{CO}_2$ @ 4.5–5.5 μm
 $^{12}\text{CO}_2$ @ 10.6 μm
 $^{13}\text{CO}_2$ @ 11.1 μm

While $^{13}\text{CO}_2$ lasers were found to provide similar performance to $^{12}\text{CO}_2$, frequency-doubled versions of $^{12}\text{CO}_2$ are also available at conversion efficiencies of about 40%. DF lasers, on the other hand, are capable of single-line operation at conversion efficiencies of only 20%, while Nd:YAG lasers suffer from poor quality output characteristics. Therefore, lasers based on CO_2 appear to be the best choices for LADAR transmitters due to their degree of technological maturity, high power, narrow linewidth, and small chirp characteristics. Of the possible CO_2 laser configurations, the MOPA configuration was selected for its low frequency-chirp, high gain, and superior control of pulse characteristics.

High spatial resolution was then used as a measure of effectiveness in reviewing detector technology, with two-dimensional FPAs providing the best performance. Array sizes for current-technology IR FPAs are 512×512 elements for the 3–5 μm band, and 128×128 elements for the 8–12 μm band. Typical square element sizes range from 10 μm to 50 μm .

The major design variable in choosing optics is the telescope configuration. The Ritchey-Chretien variant of the Cassegrainian arrangement was found to be optimum in terms of size, alignment, and aberration qualities. Relatively large primary reflectors can now be accommodated in the manufacture of telescope optics by welding individual mirror segments together. However, care must be taken during LADAR operation to avoid mirror damage with high-power laser irradiance.

Effective acquisition schemes for searching geosynchronous orbits are limited by the lengthy pulse round-trip times from such long ranges. However, by using two telescopes with differing primary apertures in a transmit/receive combination, acquisition time is greatly reduced as well as improving system sensitivity.

IV. The Infrared Environment

Introduction

This chapter examines the major environmental characteristics which affect LADAR reception and IR propagation in the atmosphere. The chapter covers four major areas which describe (1) computer models of the atmosphere, (2) background solar and thermal radiance across the IR region, (3) atmospheric transmission of selected IR wavelengths, and (4) other effects on propagation such as turbulence and air breakdown. Although the unsuitability of current-technology Nd:YAG and DF lasers for LADAR applications was highlighted in Chapter III, both wavelengths are included in initial radiance and transmittance calculations for comparison purposes.

Atmospheric Models

Several computer programs exist which approximate the structure and characteristics of the atmosphere in order to calculate the amount of scattering and absorption of optical radiation. Perhaps the most widely used program in the scientific community is the LOWTRAN atmospheric transmittance/radiance model developed by the Air Force Geophysics Laboratory. The currently available version of the program is LOWTRAN7, and was developed, according to Kneizys et al., to provide a quick method of estimating

... atmospheric transmittance, atmospheric background radiance, single scattered solar and lunar radiance, direct solar radiance, and multiple scattered solar and thermal radiance. The spectral resolution of the model is 20 cm^{-1} (full width at half-maximum) in steps of 5 cm^{-1} from 0 to $50,000 \text{ cm}^{-1}$ ($0.2 \mu\text{m}$ to infinity). A single-parameter band model is used for molecular line absorption and the effects of molecular continuum-type absorption; molecular scattering, aerosol and hydrometeor absorption and scattering are included. Refraction and earth curvature are considered in the calculation of the atmospheric slant path and attenuation amounts along the path. (46:2)

The LOWTRAN7 program contains six representative atmospheric models for different geographies and seasons, and also includes several representative aerosol, cloud, and rain models (40:18-46; 46:4). However, the use of LOWTRAN for calculating transmittance of laser radiation is inadequate due to insufficient resolution for monochromatic calculations. For example, calculation of transmittance over a vertical path from ground (sea level) to space for CO₂ laser radiation at 10.6 μm (944.19402961 cm^{-1}) is calculated using LOWTRAN to be about 0.87 for clear skies, mid-latitude summer atmosphere, and no aerosol attenuation. Since this value is averaged over a 20 cm^{-1} interval, the full effect of line absorption by atmospheric CO₂ is not included.

A detailed calculation of monochromatic transmittance can only be obtained by considering the absorption contribution from each spectral line of the atmospheric constituents (40:18-37). Such a 'line-by-line' calculation is possible using FASCODE (Fast Atmospheric Signature Code), which is another program developed by the Air Force Geophysics Laboratory. Major FASCODE features are similar to LOWTRAN, but the algorithm is optimized for the "accelerated line by line calculation of spectral transmittance and radiance for atmospheric problems" (15:1). Using the FASCOD2 version of FASCODE, the calculated transmittance value for CO₂ laser radiation yields a ground-to-space transmittance value of only 0.32, with the same options selected as for the LOWTRAN7 calculation. Clearly, line-by-line calculation is required to compute accurate transmittance values for the wavelengths under study.

In addition to modeling the atmospheric transmittance of radiation, both LOWTRAN7 and FASCOD2 include the capability to calculate background sky-radiance for a selected look angle. In particular, LOWTRAN7 includes a multiple scattering parameterization to allow calculation of background solar and thermal radiance. The estimated error associated with this parameterization is less than 20%, when all possible look angles are considered (46:4). FASCOD2, however, does

not include multiple scattering effects, and only uses a single scattering model when calculating radiance (15:1). Although the single scattering model is a good approximation when look angles close to the sun are selected, FASCOD2 radiance calculations generally underestimate sky radiance (40:18-58). Therefore, the LOWTRAN7 program was selected for all radiance calculations in this analysis.

Background Radiance

Sources of background radiance in a LADAR system include direct solar radiance, scattered solar radiance, thermal sky emission, and thermal emission from receiver optics. To simplify calculations, direct viewing of the sun will not be considered, and cryogenic cooling of receiver optics will be assumed so that optics emission is negligible. In terms of viewing conditions, worst-case background radiance occurs in daytime due to solar radiation and thermal sky emission. Furthermore, sunlit cloud is detrimental for near IR wavelengths, while sky emission is detrimental at longer wavelengths (87:3-71). These factors will be examined using LOWTRAN7.

Several options are available for calculating radiance using LOWTRAN7, with choices between several reference atmospheres, aerosol models, weather conditions, and viewing geometries. Models for the atmosphere and aerosol can be selected with knowledge of the proposed sensor site. Since co-location with GEODSS is a logical choice for siting of a LADAR sensor network, characteristics of the four existing GEODSS sites are assumed to be representative of likely LADAR locations. The geographic locations and elevations above sea level for the four GEODSS sites are shown in Table 4.

The available LOWTRAN7 atmospheric models are *tropical* (15° N), *mid-latitude* (45° N) summer and winter, *subarctic* (60° N) summer and winter, and the 1976 US Standard atmosphere. The available aerosol models for the boundary layer (0-2 km) include *rural*, *maritime*, *urban*, *tropospheric*, *advective fog*, *radiative fog*, and *desert*. Aerosol models for the tropospheric (2-10 km) and stratospheric

Table 4. GEODSS Site Characteristics (Extracted from (47:57; 30:III-22))

<i>GEODSS Site</i>	<i>Latitude</i>	<i>East Longitude</i>	<i>Elevation (km)</i>
Socorro, NM	33.8	253.3	1.53
Maui, HI	20.7	203.7	3.04
Daegu, South Korea	35.7	128.6	0.75
Diego Garcia	-8.0	73.0	sea level

(10–30 km) layers are usually determined by the season of the model, while aerosols above 30 km are assigned a default profile unless the effect of volcanic aerosol extinction is sought.

The viewing geometry used for radiance calculations appears in Figure 5, and shows that three angles must be specified for a particular viewing event. The *look angle* is determined by the satellite's position relative to the sensor, the *solar zenith angle* by the sun's relative position, and the *relative azimuth angle* by the relative positions of satellite and sun with respect to the sensor.

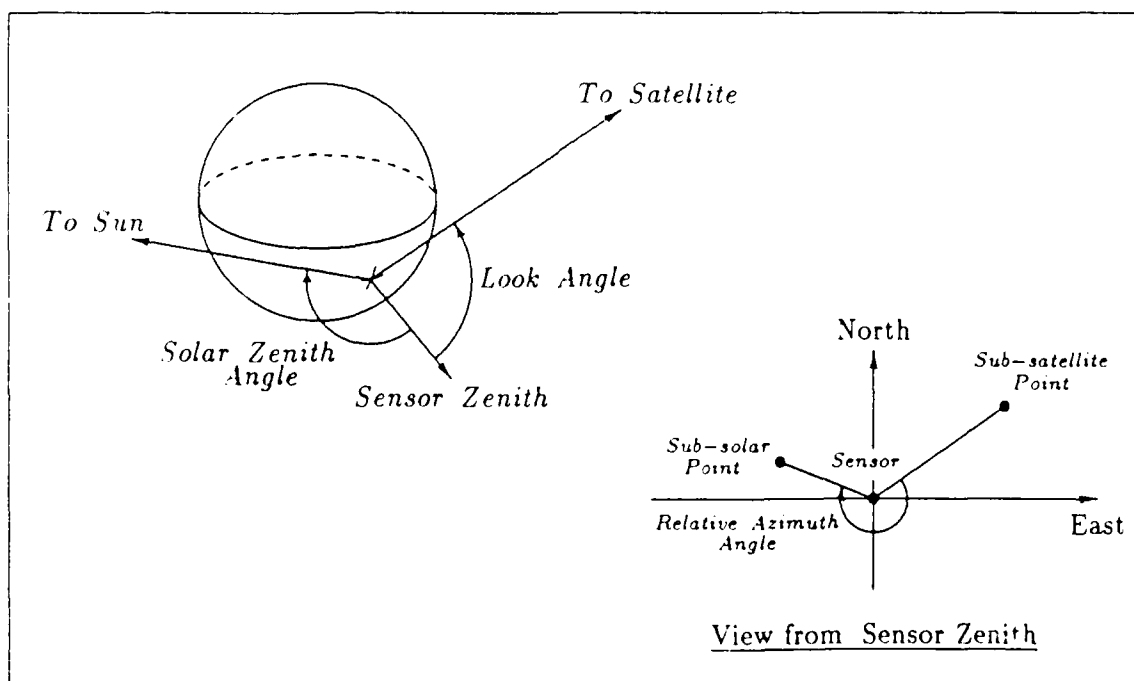


Figure 5. Geometry for Calculation of Solar and Thermal Scattered Radiance

Using the terminology of Figure 5, two cases of viewing geometry were analyzed for IR background radiance using LOWTRAN7. Both cases were calculated using a mid-latitude summer atmosphere, rural aerosol with 23 km visibility, solar zenith angle of 0° , and a sensor location at sea level. The first case was calculated for a look angle of 70° against a clear-sky background, while the second case used a look angle of 10° against a cloudy background. Figure 6 shows the resultant background level of spectral radiance for both cases over the wavelength band of $1\text{ }\mu\text{m}$ to $3\text{ }\mu\text{m}$. The Nd:YAG laser operating wavelength is also annotated.

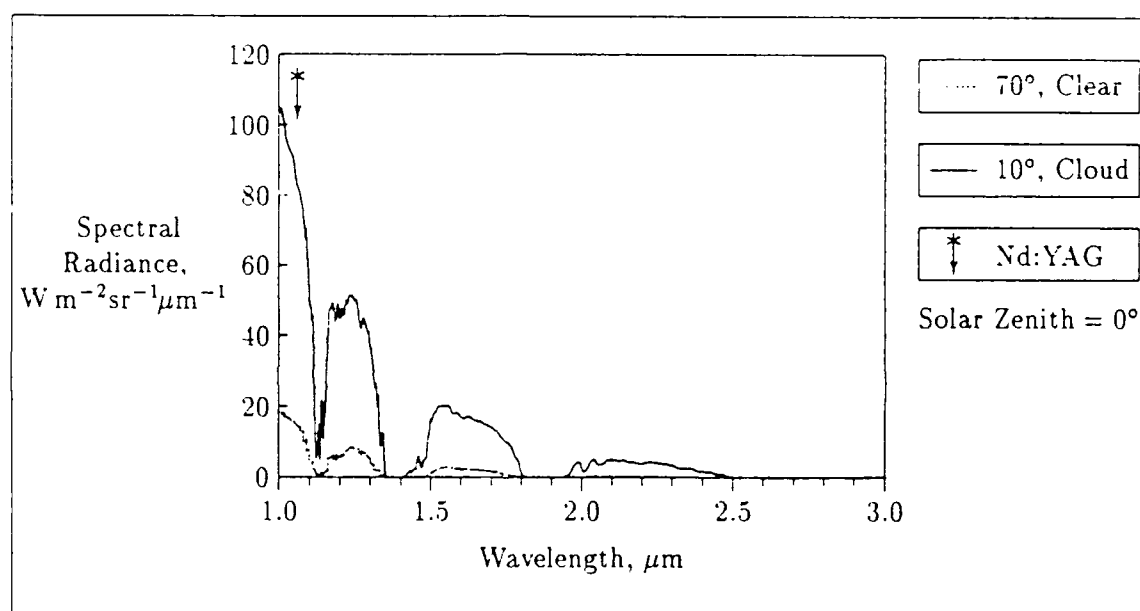


Figure 6. Background Spectral Radiance in the $1\text{--}3\text{ }\mu\text{m}$ Band, Calculated Using LOWTRAN7 for two Cases: 70° Look Angle From Sea-level Against a Clear Sky, and 10° Look Angle From Sea-level Against a Cloudy Sky

Radiance levels for the additional cases of 70° look angle/cloudy sky, and 10° look angle/clear sky were found to lie between the two extreme cases shown in Figure 6, but were not shown for reasons of plot clarity. Figure 6 shows a general trend for short wavelengths of increased levels of radiance at look angles close to the sun, along with increased background radiance from a cloudy field-of-view. At the

Nd:YAG wavelength, background spectral radiance for all calculated cases is very high, ranging from $17 \text{ W m}^{-2} \text{ sr}^{-1} \mu\text{m}^{-1}$ to $83 \text{ W m}^{-2} \text{ sr}^{-1} \mu\text{m}^{-1}$.

Figure 7 shows the spectral radiance, calculated under the same conditions, for the $3\text{--}12 \mu\text{m}$ region, annotated with DF and CO_2 laser wavelengths. In comparison to the $1\text{--}3 \mu\text{m}$ band, background radiance in the $3\text{--}12 \mu\text{m}$ region is reduced by about one order of magnitude (note the scale change between figures). Although the cases for 70° look angle/cloudy sky, and 10° look angle/clear sky were again not shown for clarity, the presence of cloud at each look angle was found to affect radiance levels only slightly.

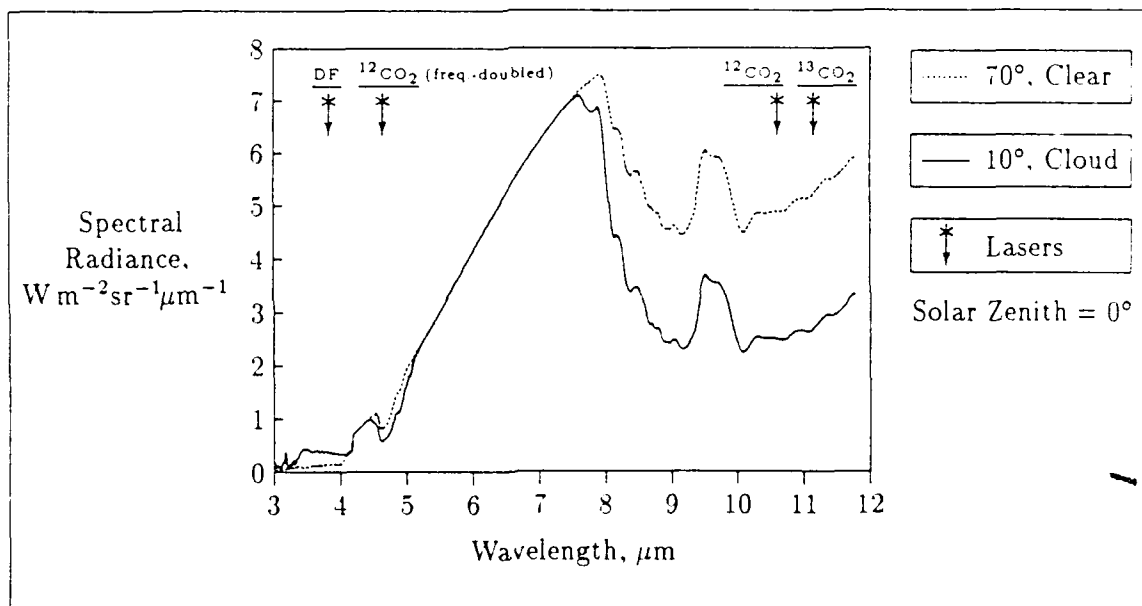


Figure 7. Background Spectral Radiance in the $3\text{--}12 \mu\text{m}$ Band, Calculated Using LOWTRAN7 for two Cases: 70° Look Angle From Sea-level Against a Clear Sky, and 10° Look Angle From Sea-level Against a Cloudy Sky

Compared to the small look-angle case, radiance levels in the far-IR were found to be higher at large look angles due to greater thermal sky emission. For a 300°K sky, this thermal emission peaks at around $10 \mu\text{m}$. The 'crossover' from domination by scattered solar radiance to domination by thermal sky radiance is at about $4.3 \mu\text{m}$. The DF and frequency-doubled CO_2 lasers radiate near the crossover point,

at wavelengths which correspond to the lowest level of background radiance for the five lasers under study. Average radiance levels at DF and frequency-doubled CO₂ wavelengths are only about $0.3 \text{ W m}^{-2}\text{sr}^{-1}\mu\text{m}^{-1}$ and $0.7 \text{ W m}^{-2}\text{sr}^{-1}\mu\text{m}^{-1}$, respectively, while ¹³CO₂ and ¹²CO₂ wavelengths encounter radiance levels which are an order of magnitude larger at $2.5 \text{ W m}^{-2}\text{sr}^{-1}\mu\text{m}^{-1}$ to $5 \text{ W m}^{-2}\text{sr}^{-1}\mu\text{m}^{-1}$, depending on look angle.

Atmospheric Transmission

Accurate FASCODE calculations for atmospheric transmittance of monochromatic radiation require precise specification of the laser wavelength to adequately account for the strong influence of line absorption. However, among the frequency-doubled and isotopically-substituted CO₂ LADAR systems reported in the literature, different laser transitions are used from system to system. For example, different frequency-doubled systems reported by Harney (27:99) and Miller et al. (56:6) use the R(20) and R(14) CO₂ transitions, respectively. Among ¹³CO₂ systems, several transitions are reportedly used, including P(24) (27:99), P(20) (88:82; 31:5), and P(18) transitions (57:103).

Due to the diversity of laser transitions in use for the CO₂-variant systems, four different ¹³CO₂ transitions were selected for analysis, along with five separate ¹²CO₂ transitions for the frequency-doubled system. Table 5 shows the resultant laser wavelengths selected for FASCOD2 calculations. All CO₂ transition frequencies were taken from Witteman (86:24-26).

Although all ¹²CO₂ systems found in the literature use the P(20) line, no reports of single-line DF systems were found. For FASCOD2 calculations, a DF wavelength of $3.83 \mu\text{m}$ was selected as a representative value, after multiple calculations showed no nearby strong absorption lines (implying negligible amounts of DF in the atmosphere). Finally, the strongest Nd:YAG transition at $1.06 \mu\text{m}$ was selected to complete the list of candidate LADAR wavelengths.

Table 5. Laser Transition Wavelengths used in FASCOD2 Calculations

<i>Laser</i>	<i>Transition</i>	<i>Wavelength (μm)</i>	<i>Frequency (cm^{-1})</i>
$^{13}\text{CO}_2$	P(24)	11.19354451	893.37206747
	P(22)	11.17130499	895.15056754
	P(20)	11.14939715	896.90947969
	P(18)	11.12781727	898.64883264
$^{12}\text{CO}_2$	P(20)	10.59104346	944.19402961
$^{12}\text{CO}_2$ (frequency-doubled)	R(14)	4.65269281	2149.29298016
	R(16)	4.64689275	2151.97564042
	R(18)	4.64122185	2154.60504026
	R(20)	4.63567900	2157.18128846
	R(22)	4.63026305	2159.70451160
DF	average	3.83	2610.96605744
Nd:YAG	$^4\text{F}_{3/2} \rightarrow ^4\text{I}_{11/2}$	1.0642	9396.72993841

Reduction of the number of candidate $^{13}\text{CO}_2$ wavelengths was carried out by performing preliminary transmittance calculations for all selected transitions over a vertical path from ground (sea level) to space through various reference atmospheres. Atmospheric profiles for the four GEODSS locations were modeled using either mid-latitude or tropical reference atmospheres, with corresponding aerosol profiles modeled as rural or maritime, respectively. All four $^{13}\text{CO}_2$ transitions exhibited similar transmittance characteristics through all atmospheric models; hence, the P(22) transition was arbitrarily chosen as a representative $^{13}\text{CO}_2$ operating wavelength for all subsequent calculations.

Table 5 was further reduced by performing a second comparison between transitions of frequency-doubled $^{12}\text{CO}_2$ for the same transmission path. Figure 8 shows the FASCOD2 results for three cases: mid-latitude summer model with rural aerosol, mid-latitude winter model with rural aerosol, and tropical model with maritime aerosol. Visibility of 23 km and clear skies were selected for all cases.

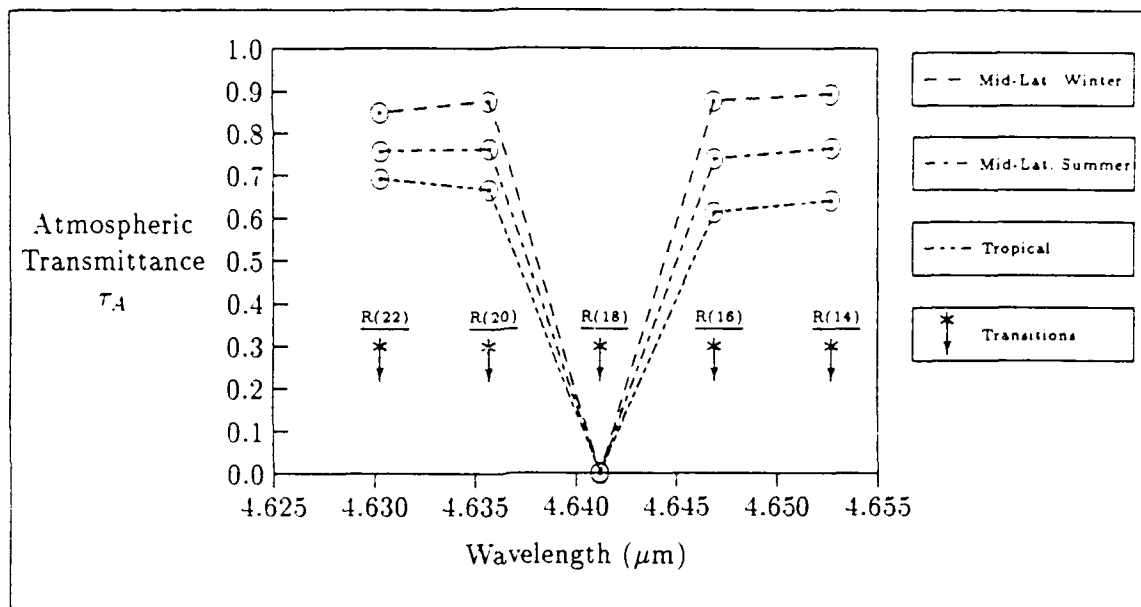


Figure 8. Atmospheric Transmittance of Frequency-Doubled CO₂ Laser Transitions over a Vertical Path from Ground to Space for three cases: Mid-Latitude Summer and Winter Atmospheres with Rural Aerosol, and Tropical Atmosphere with Maritime Aerosol

Of the three cases, poorest transmission occurs through a tropical atmosphere, with best transmission through a mid-latitude winter atmosphere. This variation may be attributed to different humidity profiles in each model, which cause different amounts of water-vapor attenuation of the laser radiation. An additional feature of Figure 8 is the strong absorption line which occurs in the vicinity of the R(18) transition, so that transmittance in all atmospheric cases is virtually extinguished around 4.641 μm. Transmittance at all four remaining wavelengths is reasonably high; consequently, the R(20) wavelength was arbitrarily chosen as representative for subsequent calculations.

A comparison of atmospheric transmittance characteristics was then performed between the reduced list of five candidate wavelengths from Table 5, for the same transmission path and models, with the results plotted in Figure 9. As expected, strong self-absorption is evident at the ¹²CO₂ wavelength, while the remaining four laser wavelengths display generally high transmittance. Figure 9 also shows the

adverse effect that water vapor has on transmission in the 8–12 μm band, with transmittance through a tropical atmosphere only about 50% of the value calculated for a mid-latitude winter atmosphere.

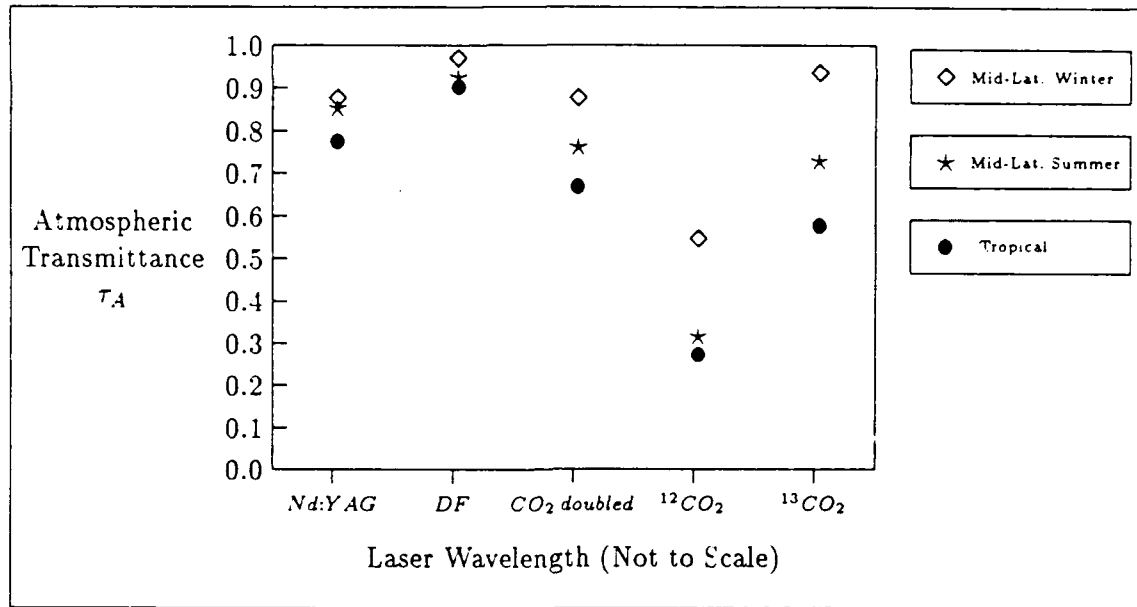


Figure 9. Atmospheric Transmittance of Five Selected Laser Wavelengths over a Vertical Path from Ground to Space for three cases: Mid-Latitude Winter and Summer Atmospheres with Rural Aerosol, and Tropical Atmosphere with Maritime Aerosol

The effect of different atmospheric models on DF transmittance is seen from Figure 9 to be only slight. These excellent transmittance characteristics of DF radiation, combined with the high power possible from multi-line DF operation, are strong reasons for the continued development of high-efficiency, single-line DF LADAR transmitters.

Look Angle. The influence of look angle on transmittance for the likely range of geographic and atmospheric conditions was then examined. Viewing conditions were modeled in FASCOD2 by selecting GEODSS locations at Socorro and Diego Garcia as indicative of two extreme geographic/atmospheric combinations. Accordingly, the two cases considered were: Socorro — slant path from 1.53 km altitude to space,

through a mid-latitude winter atmosphere and rural aerosol with 23 km visibility — and Diego Garcia — slant path from sea level to space, through a tropical atmosphere and maritime aerosol with 23 km visibility. Additionally, to reduce computational effort, wavelengths of only the three CO₂-variant lasers were examined.

Figures 10 and 11 show the results of FASCOD2 calculations for the three laser wavelengths. Comparing transmittance at large look angles with vertical transmission, both figures show higher relative attenuation losses with ¹²CO₂ than with the ¹³CO₂ and frequency-doubled lasers. For example, ¹²CO₂ transmittance from Socorro at a 60° look angle is 40% lower than vertical transmittance. Conversely, frequency-doubled CO₂ transmittance at 60° from Socorro falls off by 5%, while ¹³CO₂ transmittance is reduced by only 3%. In the Diego Garcia case, the transmittance degradation at 60° look angle for ¹²CO₂, frequency-doubled CO₂, and ¹³CO₂ is 57%, 21%, and 17%, respectively.

Since two-way atmospheric transmittance is required for LADAR signals, the degradation in one-way transmittance at large look angles has drastic effects on LADAR signals. For example, the 57% reduction in ¹²CO₂ laser transmittance from Diego Garcia at a 60° look angle has the effect of attenuating LADAR signals by a further 82% when compared to two-way vertical transmission. This sharp reduction in two-way ¹²CO₂ transmittance at large look angles would limit LADAR coverage to a small range of look angles unless extra transmitter power was available to compensate for the higher signal attenuation. Therefore, the ¹²CO₂ laser is rejected as a LADAR transmitter candidate in favor of the ¹³CO₂ and frequency-doubled lasers.

Cloud and Rain. The effect on transmittance of clouds and rain can also be analyzed using FASCOD2. However, software anomalies associated with the available copy of both FASCOD2 and LOWTRAN7 prevented execution using these options.

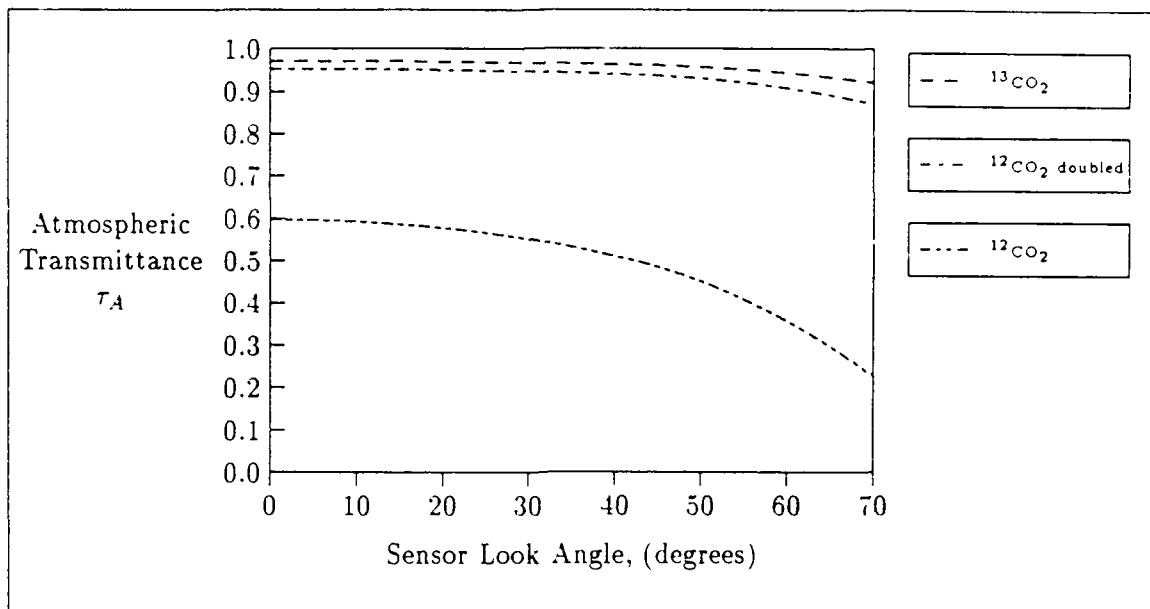


Figure 10. Atmospheric Transmittance at Socorro — Slant Path from 1.53 km Altitude to Space, Through a Mid-Latitude Winter Atmosphere and Rural Aerosol with 23 km Visibility

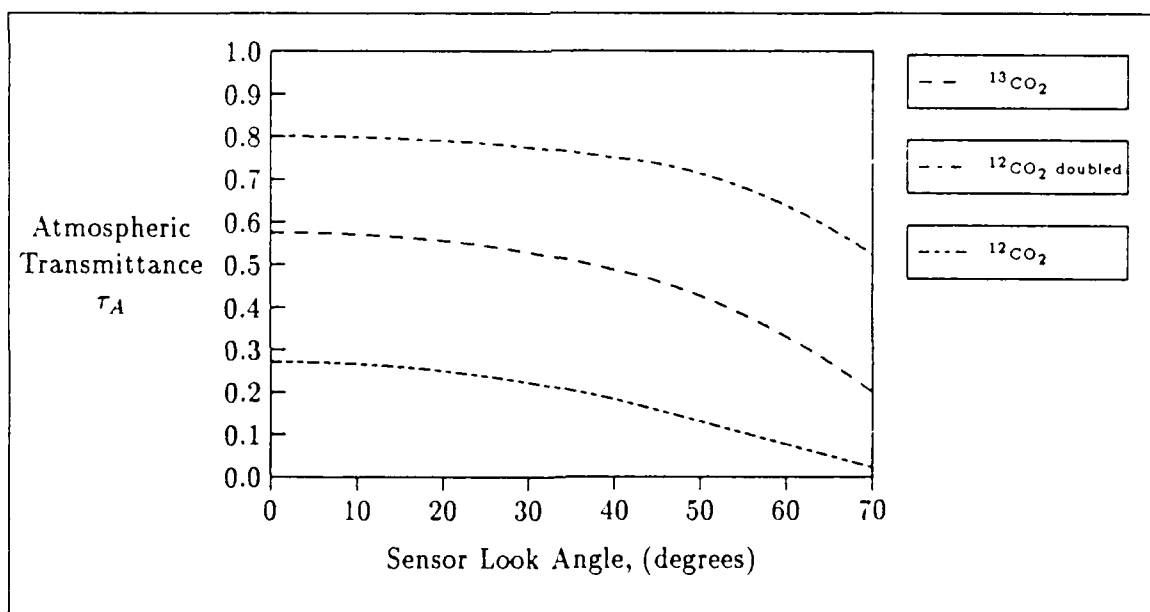


Figure 11. Atmospheric Transmittance at Diego Garcia — Slant Path from Sea-Level to Space, Through a Tropical Atmosphere and Maritime Aerosol with 23 km Visibility

Nonetheless, an estimate of the effects of cloud and rain may be gained by considering the algorithms used in LOWTRAN and FASCOD to determine cloud and rain attenuation. Although details of the LOWTRAN7 algorithms were unavailable for this analysis, LOWTRAN6 algorithms were used instead.

The primary model used in LOWTRAN6 for cloud attenuation is the cirrus cloud model. Other models for cumulus and stratus profiles have been added to LOWTRAN7 and FASCOD2, but details of these were also unavailable for this study. Based on empirical data, attenuation by cirrus has been found to be "proportional to the cloud thickness and independent of wavelength from ...0.317 μm to 10 μm " (45:58). The expression used to calculate cirrus transmittance is given by Kneizys et al. as (45:66)

$$\tau = e^{-0.14 L^2} \quad (3)$$

where L is the cloud thickness in km.

Based on measured cloud statistics, cirrus thickness was found by Kneizys et al. to follow a truncated log-normal distribution, with a median cirrus thickness of 1.0 km (45:60). The average height of the cirrus cloud base was also defined for tropical and mid-latitude winter atmospheres as 11 km and 8 km, respectively (45:67). Using the median thickness value in Equation (3) yields an average IR cirrus transmittance of 0.87 *for vertical propagation*. Assuming a plane-parallel atmosphere and an ideal cirrus cloud of constant thickness and uniform density, Equation (3) may be modified to include the effect of look angle as

$$\tau = e^{-0.14 \sec \psi, L^2} \quad (4)$$

where ψ , is the sensor look angle.

The assumption of a plane-parallel atmosphere allows the use of sensor look angle to approximate the zenith angle at which laser radiation enters the cloud. Considering the range of cloud-base altitudes under study, exact calculations show

that the approximation of the cloud-entry angle is in error by less than 0.4% for look angles as large as 70°. Equation (4) also neglects refraction, which is a valid assumption for cloud-entry zenith angles of less than 80° (45:13).

The rain attenuation algorithm used in LOWTRAN6 relates transmittance to rain-rate, and is also independent of wavelength over the IR region. The expression used to calculate rain transmittance is given by Kneizys et al. as (45:69)

$$\tau = e^{-0.365 s r^{0.63}} \quad (5)$$

where s is the path length, in km, through rain falling at a rate r , in mm/hr.

Calculation of the path length, s , can be written in terms of look angle and altitude of the cloud tops causing the rain, z_c , as $s = z_c \sec \psi$. Therefore, Equation (5) may be re-written as

$$\tau = e^{-0.365 z_c \sec \psi r^{0.63}} \quad (6)$$

Rain rate is categorized in LOWTRAN6 and FASCOD2 as *drizzle* (2 mm/hr), *light rain* (5 mm/hr), *moderate rain* (12.5 mm/hr), *heavy rain* (25 mm/hr), and *extreme rain* (75 mm/hr) (46:25-26). Figure 12 shows Equation (6) plotted for the Socorro site through drizzle, light rain, and moderate rain, and also shows Equation (4) plotted for median cirrus conditions. Note that the transmittance values plotted in Figure 12 can be applied to all IR wavelengths, but only include the attenuation caused by cirrus or rain. A total atmospheric transmittance value for the entire ground-to-space path through cloud or rain can be obtained by multiplying the appropriate Figure 12 transmittance value by the corresponding clear-weather transmittance from Figure 10 or 11.

Figure 12 cirrus transmittance was calculated with a median cirrus profile existing between 8 km and 9 km altitude. For the rain conditions, rain rate was modeled as constant between ground level and 2 km altitude (470 m above the Socorro site). Attenuation from rain clouds was not included in the rain calculation

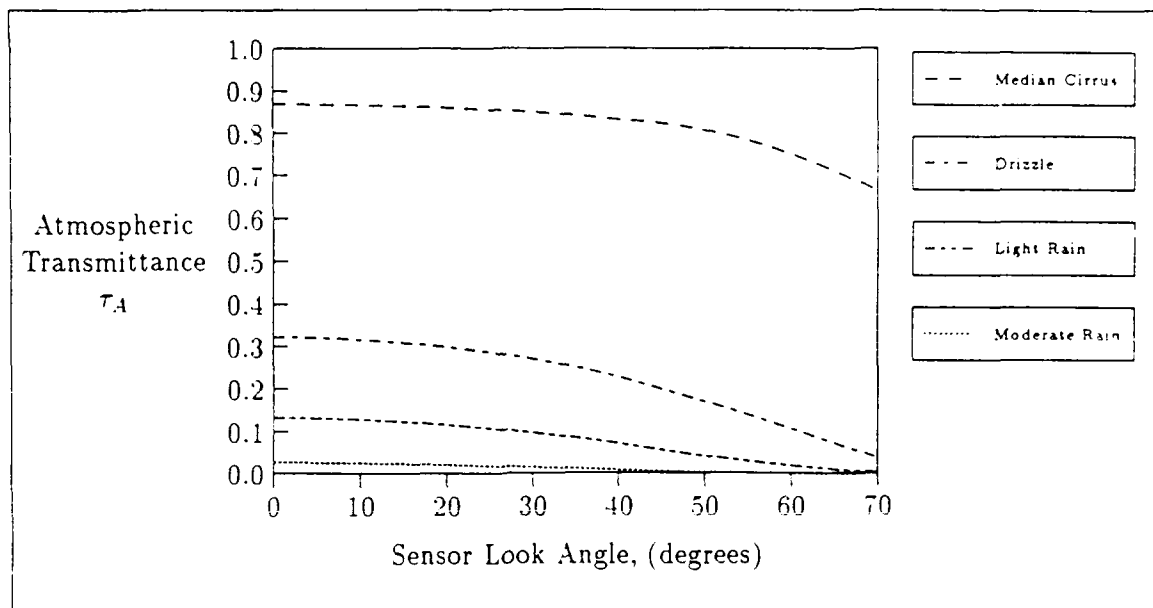


Figure 12. Transmittance Component due to Cloud and Rain from Socorro for Three Cases: Cirrus Cloud from 8 km to 9 km Altitude, Drizzle Originating from 2 km, Light Rain from 2 km, and Moderate Rain from 2 km

since a suitable low-altitude cloud model was unavailable, and cloud attenuation is small compared to rain attenuation. The corresponding LOWTRAN6 model for these conditions uses a gradually decreasing rain rate from ground level up to a final rain altitude of 2 km or 3 km altitude, depending on rain rate. Therefore, the conditions used in Figure 12 account for higher rain attenuation than the equivalent LOWTRAN6 model.

Although use of a constant rain-rate model is a simplification, some idea of the severity of rain attenuation at IR wavelengths may be gained from the resultant data. A rain rate of only 2 mm/hr results in a 68% reduction in total transmittance for a vertical path. This reduction corresponds to a 90% decrease in two-way total transmittance.

Attenuation effects at higher rain rates and larger look angles are more severe, and indicate that LADAR operation through rain is impractical due to the extreme

amount of attenuation for two-way signal propagation. For example, if a $^{13}\text{CO}_2$ transmitter is used from Socorro at a moderate look angle of 30° through drizzle, total two-way atmospheric transmittance amounts to only 7%. For lower-altitude sites, such as Diego Garcia, transmittance becomes negligible for even trace precipitations.

On the positive side, however, attenuation due to cirrus appears acceptable for continued LADAR operation. Using the same example of a $^{13}\text{CO}_2$ signal at 30° , total two-way transmittance is about 70% for Socorro, and 50% for Diego Garcia. Although the attenuating effects of lower-altitude clouds such as stratus and cumulus have not been considered, operation of an IR LADAR through cirrus cloud seems practical.

Other Effects

Turbulence. Apart from scattering and absorption, laser transmission through the atmosphere is likely to be influenced by several other effects produced by atmospheric turbulence. Turbulence induces random variations in the atmospheric index of refraction, via fluctuations in temperature, pressure, and humidity. Theory developed by Kolmogorov models the turbulent atmosphere as consisting of mobile parcels of air, or *eddies*, of differing indices of refraction (87:6-9). While these eddies range in size from sub-centimeter at the earth's surface, to global scale in the open atmosphere, the size range of interest in laser propagation lies from a few millimeters to a few meters, known as the *inertial sub-range* (87:6-9).

Turbulence effects experienced by LADAR signals include beam steering, image dancing, beam spreading, spatial coherence degradation, and scintillation (40:18-71; 69:3295). *Beam steering* occurs when the laser beam diameter is smaller than the turbulence eddies, and can result in deviation of the beam so that, in extreme cases, the target or receiver aperture is completely missed (40:18-71). Conversely, when the beam diameter is larger than the eddies, *beam spreading* occurs, resulting in lower irradiance values at the target or receiver.

Turbulence-induced modulation in the angle-of-arrival of the received wave can also occur, resulting in shifting of the image focus, or *image dancing*. Smaller turbulence eddies cause phase changes across the wavefront, resulting in *loss of spatial phase coherence*, and also induce interference effects within the beam which cause random power fluctuations, or *scintillation*, across the wavefront.

Beam steering and image dancing can both be reduced by increasing the receiver aperture. Since prospective LADAR locations such as the GEODSS sites are characterized by low turbulence, the most serious turbulence effects remaining for coherent IR reception are scintillation and coherence losses. Description of these turbulence effects is best expressed in terms of the *refractive-index structure coefficient*, C_n^2 . Values of C_n^2 vary widely according to prevailing atmospheric conditions, and are a complex function of altitude and wind speed (87:6-14; 40:18-72). Several models of C_n^2 have been developed from empirical data, with one of the simplest given by (87:6-14)

$$C_n^2(z) = \begin{cases} \frac{1.5 \times 10^{-13}}{z} & \text{below 20 km above sea level} \\ 0 & \text{above 20 km above sea level} \end{cases} \quad (7)$$

where z is altitude above local ground, in meters.

Scintillation effects at the receiver are described by the variance in the log-amplitude of the received plane wave, given by (27:92)

$$\sigma_x^2 = 0.56 k^{7/6} \int_0^s C_n^2(z) (s-z)^{5/6} \left(\frac{z}{s}\right)^{5/6} dz \quad (8)$$

where s is the path length.

Scintillation also affects the transmitted laser beam, which can cause non-uniform irradiance of the target, depending on its size. The combined effect of scintillation over both transmit and receive paths (which may be correlated (14:514)) makes

estimation of σ_v^2 difficult. Typically, a signal-to-noise ratio 'scintillation margin' is added to design calculations to account for power fluctuations (87:23-16).

Signal coherence losses are usually described in terms of r_o , the *transverse phase coherence length*, which measures the lateral distance over which the radiation remains constant (40:18-71; 87:6-29). In the transmitter case, when the primary aperture exceeds r_o , "the effective transmitter beamwidth will be turbulence-limited rather than diffraction-limited" (69:3295); for the receiver case, when the primary aperture exceeds r_o , heterodyne efficiency is reduced, thereby reducing signal-to-noise ratio (87:6-30). Harney expresses the transverse coherence length for the transmitter-to-target path, r_{ot} , as (27:92)

$$r_{ot} = \left[2.91 k^2 \int_0^{z_t} C_n^2(z) \left(1 - \frac{z}{z_t} \right)^{5/3} dz \right]^{-3/5} \quad (9)$$

where $k = 2\pi/\lambda$, and z_t is the target altitude above local ground.

Similarly, Harney gives the transverse coherence length for the target-to-receiver path, r_{or} , as (27:92)

$$r_{or} = \left[2.91 k^2 \int_0^{z_t} C_n^2(z) \left(\frac{z}{z_t} \right)^{5/3} dz \right]^{-3/5} \quad (10)$$

Using the simplified model of C_n^2 from Equation (7) in Equations (9) and (10) allows a simplified calculation of r_o for selected LADAR site elevations and wavelengths. Figure 13 shows the results for r_{ot} and r_{or} , calculated over the 1-13 μm band for the Diego Garcia site elevation. The figure shows that coherence lengths for the receive path are generally about five times longer than for the transmit path. At the $^{13}\text{CO}_2$ wavelength, the r_{ot} value — and hence, maximum transmitter-aperture diameter — is about 0.9 m, while the maximum receiver-aperture diameter is about 4.5 m. For the frequency-doubled CO_2 wavelength, maximum aperture diameters are one-third of the size, at 0.3 m and 1.5 m, respectively.

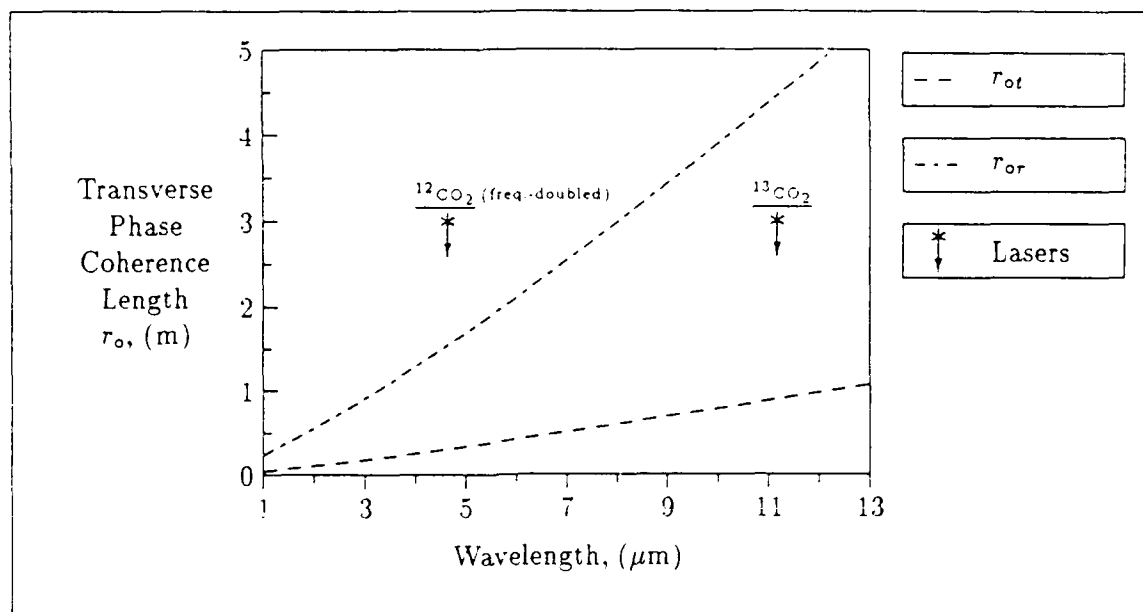


Figure 13. Transverse Phase Coherence Length for Transmit and Receive Paths versus Wavelength

Site elevations of up to 2 km yield virtually the same curves since the simplified expression used for C_n^2 corresponds to a turbulence profile commencing from local ground rather than sea level. Thus, an increase in site elevation causes the 20 km altitude turbulence-cutoff to reduce turbulence from the 'weak' higher end of the model profile. In reality, reduced thermal effects and increased wind at higher site elevations leads to lower turbulence than that predicted by this simplified model. Therefore, higher site elevations will generally allow larger values of r_o . Also, since turbulence is random in nature, there will always be a finite probability that coherence lengths will exceed the calculated values, no matter how accurate the model. Wolfe et al. state that, typically, atmospheric turbulence limits the transmitter beam divergence to about $10 \mu\text{rad}$ at a wavelength of $10 \mu\text{m}$ (87:23-12).

High-Power Beam Effects. Two additional propagation factors need to be considered when the transmitted laser beam is of high power. The first factor is *thermal blooming*, which occurs when the beam contains enough power to significantly heat

the atmosphere (87:6-35). Although serious for high-power CW signals, thermal blooming may become significant in pulsed systems which use long pulse widths or high repetition rates. The second high-power effect, *air breakdown*, occurs when the laser pulse interacts with aerosol particles which lower the air-breakdown threshold. This phenomenon depends on particle size, beam diameter, and pulse width; for example, at 10.6 μm , breakdown has been shown to occur at an irradiance level of 100-200 MW/cm², which is attributed to aerosol particles of 4-10 μm diameter (5:1421).

Summary

Analysis of the environment in which a deep-space IR LADAR must operate has highlighted several factors which influence wavelength selection, including atmospheric transmission, background radiance, and turbulence effects. The LOWTRAN7 and FASCOD2 computer programs were used to compare transmittance and radiance conditions at Socorro and Diego Garcia. Nd:YAG and DF laser wavelengths were included in the comparison to demonstrate their excellent transmission performance. However, due to the poor output characteristics of Nd:YAG and DF, the final transmitter comparison was confined to CO₂-variant lasers.

The final comparison showed that poorest transmission occurs through the tropical atmosphere at Diego Garcia, with transmittance decreasing with larger look angles in all cases. In particular, the P(22) wavelength of ¹³CO₂ at 11.17 μm exhibited the best transmittance under all conditions, closely followed by the frequency-doubled R(20) wavelength of ¹²CO₂ at 4.64 μm . These two laser candidates represent the best examples from the 3-5 μm and 8-12 μm bands in terms of transmittance. All other candidate CO₂ laser wavelengths were rejected as potential LADAR transmitters due to poor atmospheric transmittance over the range of conditions examined.

The effects of cloud and rain were found to be independent of wavelength, based on the cloud and rain models in LOWTRAN6. Transmittance was found

to be severely degraded by even a small amount of rain; hence, LADAR operation through rain appears impractical. However, LADAR operation through average cirrus conditions was shown to be theoretically feasible, with only minor attenuation effects.

Background radiance levels at medium to far-IR wavelengths were determined to be generally low compared to levels at shorter wavelengths. Of the two laser candidates, radiance at $4.64\text{ }\mu\text{m}$ is much lower than at $11.17\text{ }\mu\text{m}$.

Several effects of turbulence on signal propagation were also examined, with scintillation and coherence degradation highlighted as the most serious effects for long-range LADAR applications. Compensation of scintillation can be adequately performed by the addition of a scintillation margin to system signal-to-noise calculations. Loss of phase coherence, on the other hand, may be minimized by limiting the size of the transmitter and receiver apertures to the value of r_o , the transverse phase coherence length. r_o is wavelength-dependent and generally allows larger receiver apertures than transmitter apertures. Figure 13 provides rough estimates of aperture size limits using a simplified atmospheric model.

V. Parametric Analysis

Introduction

The design of a ground-based LADAR which is designed to detect small, moving, deep-space targets while 'looking' through a turbulent, hazy, sunlit atmosphere requires high performance specifications. Careful design of all sensor elements is essential, from telescope mount to processing electronics, so that maximum laser energy is deposited on target, and maximum reflected signal is collected at the detector for processing. Once the target is detected, estimates of target range, angular position, and radial velocity are obtained from the detected pulse. Detection of successive pulse returns also allows estimation of target angular rates and lateral velocity, which may be used to derive an orbital element set for the target.

With these overall design goals in mind, a comprehensive set of equations is required which relate laser, telescope, and detector characteristics to LADAR performance parameters. This equation set can then be used for the specification and evaluation of a candidate ground-based deep-space LADAR design; the LADAR configuration used as the basis for this parametric analysis is the candidate system outlined in Chapter III, with the transmitted signal consisting of a train of M rectangular pulses. Detection analysis concentrates initially on a single square detector element, but is then optimized for two-dimensional FPA detection with arbitrary pixel and gap dimensions. Analysis of the heterodyne process examines beam misalignment effects and also considers different LO characteristics and their effect on receiver efficiency.

Detection Probability

The process of detecting a LADAR signal in the presence of noise is statistical in nature due to the randomly fluctuating noise component (73:2-7). This detection process is conventionally described using two parameters — the *probability of*

detection, p_d , which represents the probability of detecting a real target, and the probability of false-alarm, p_{fa} , which represents the probability of mistakenly identifying a noise fluctuation as a real target (68:253; 73:2-7). Both parameters are specified prior to system design calculations, and are examined first since they form the basis from which minimum system performance specifications are derived.

To enable further analysis of the detection process, Figure 14 depicts a block diagram of typical LADAR detection circuitry (6:38). The received signal is heterodyne detected before passing through a matched filter. The output of the filter is envelope detected and compared to a threshold reference, providing a true/false output. The threshold reference is set by combining a measurement of the noise photocurrent with a specified p_{fa} (6:39).

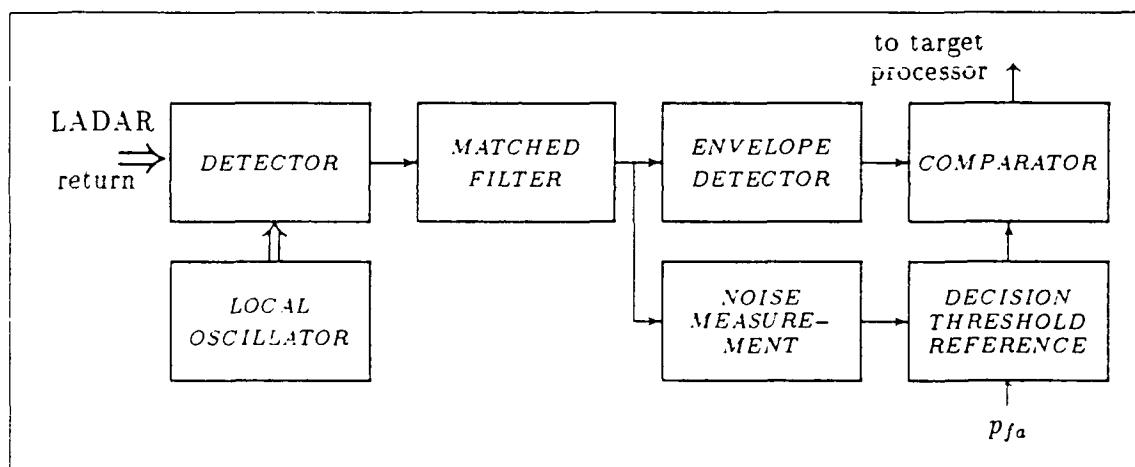


Figure 14. LADAR Detection Circuitry (Adapted from Bachman (6:39))

The sources of noise in a heterodyne LADAR include dark current, thermal noise, background photocurrent, and local oscillator-induced shot noise (41:141). However, if the local oscillator (LO) power is adjusted so that the weak received signal is mixed with a strong LO signal, the LO-induced shot noise can be made to dominate all other noise sources (6:39). Operation of the LADAR in this manner is said to be *shot-noise limited*. This mode of operation is preferable to *background limited* operation since background noise generally fluctuates in an unpredictable

fashion and is difficult to model. Due to the random nature of shot noise, however, Gaussian statistics may be used to model the detection process. In this case the noise current can be written as

$$n(t) = r(t)e^{j\phi(t)} \quad (11)$$

where $n(t)$ is the time-dependent noise current, and $r(t)$ and $\phi(t)$ are the amplitude and phase of the current, respectively, at time t .

The Gaussian joint probability density function of r and ϕ can then be written as (6:39)

$$p(r, \phi) = \frac{r}{2\pi\sigma_n^2} e^{-\frac{r^2}{2\sigma_n^2}} \quad (12)$$

where σ_n^2 is the average noise power.

The corresponding noise envelope at the output of the envelope detector with no signal present can then be found by integrating Equation (12) to remove the phase term (8:59):

$$p(r) = \frac{r}{\sigma_n^2} e^{-\frac{r^2}{2\sigma_n^2}} \quad (13)$$

This Rayleigh-distributed probability density function can then be used to provide an expression for the *probability of false alarm*, p_{fa} (6:40):

$$p_{fa} = \int_{r_t}^{\infty} p(r) dr = e^{-\frac{r_t^2}{2\sigma_n^2}} \quad (14)$$

where r_t is the decision threshold.

A typical value of p_{fa} for radar detection is 10^{-6} . However, a more practical representation of false-alarm occurrence is the *mean time between false-alarms*, t_{fa} . If a train of M received pulses is detected with range gates, and then integrated by

post-detection circuitry, the mean time between false-alarms is given by (73:2-17)

$$t_{fa} = \frac{Mt_g}{p_{fa}(1 - \delta_{off})} \quad (15)$$

where t_g is the range gate on-time, and δ_{off} is the fraction of the time for which no gates are open (dead time).

For example, for $M = 10$, $t_g = 10 \mu s$, $p_{fa} = 10^{-6}$, and $\delta_{off} = 0.99$, the theoretical mean time between false-alarms is 2.8 hours.

From Equation (14), p_{fa} is seen to depend on the decision threshold and the noise power. The *probability of detection*, on the other hand, is influenced by the threshold, noise power, and signal power. Some knowledge of the reflected signal characteristics from the target is therefore necessary to adequately model the detection process. Since the targets under consideration have generally diffuse surfaces, the reflected signal is described by Bachman as

... the sum of the field scattered from each of the individual elementary scatterers, each of which has a uniformly distributed random phase as a consequence of the random spatial distribution of the surface.

Hence, by the central limit theorem, in-phase and phase-quadrature components of the field, as well as the photocurrents they induce, have independent Gaussian distributions with a common variance, σ_d^2 [σ_d^2 is the average signal power received from a diffuse target], and zero mean. (6:40)

Since the Gaussian signal distribution is added to the Gaussian noise distribution, the envelope detector output with both signal and noise present follows a Rayleigh probability distribution given by

$$p(r') = \frac{r'}{\sigma_t^2} e^{-\frac{r'^2}{2\sigma_t^2}} \quad (16)$$

where $\sigma_t^2 = \sigma_n^2 + \sigma_d^2$.

In a similar manner to Equation (14), the probability of detection can be described as

$$p_d = \int_{r_t}^{\infty} p(r') dr' = e^{-\frac{r_t^2}{2\sigma_t^2}} \quad (17)$$

Figure 15 provides a pictorial representation of p_{fa} and p_d . The value of σ_n^2 is easily obtained via the noise measurement process shown in Figure 14, but the value of σ_t^2 relies on information concerning both noise *and* signal and can be written as (6:40)

$$\sigma_t^2 = \sigma_n^2 + \sigma_d^2 = \sigma_n^2(1 + SNR) \quad (18)$$

where SNR is the *signal-to-noise power ratio from a diffuse target*.

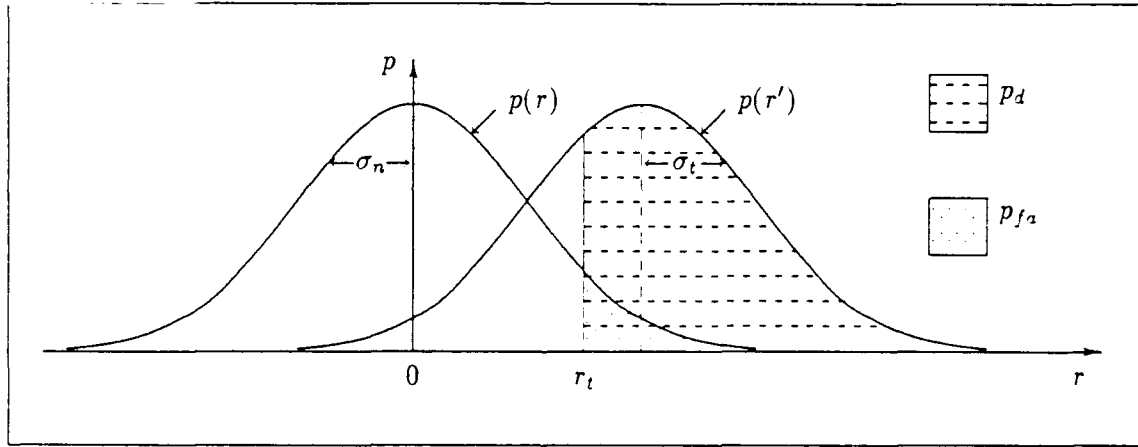


Figure 15. Graphical Representation of p_d and p_{fa}

SNR is now the only unknown variable in relating p_d , p_{fa} , and r_t . Equations (14), (17), and (18) can be combined to obtain an explicit expression for minimum SNR as follows:

$$SNR_{min} = \frac{\ln p_{fa}}{\ln p_d} - 1 \quad (19)$$

From Equation (19), p_d and p_{fa} are seen to be related via SNR to measurable system parameters — received signal and noise powers. For multi-pulse detection, significant improvement in SNR can be achieved through pulse integration, where

the magnitude of improvement is dictated by target characteristics and pulse integration techniques. Calculation of p_d and p_{fa} in this event is complicated since the distribution of noise and signal powers at the integrator output is required (73:2-18). For a non-fluctuating received signal and post-detection integration, Figure 16 shows the minimum SNR requirement for $p_d = 0.95$ and three values of p_{fa} (73:2-21).

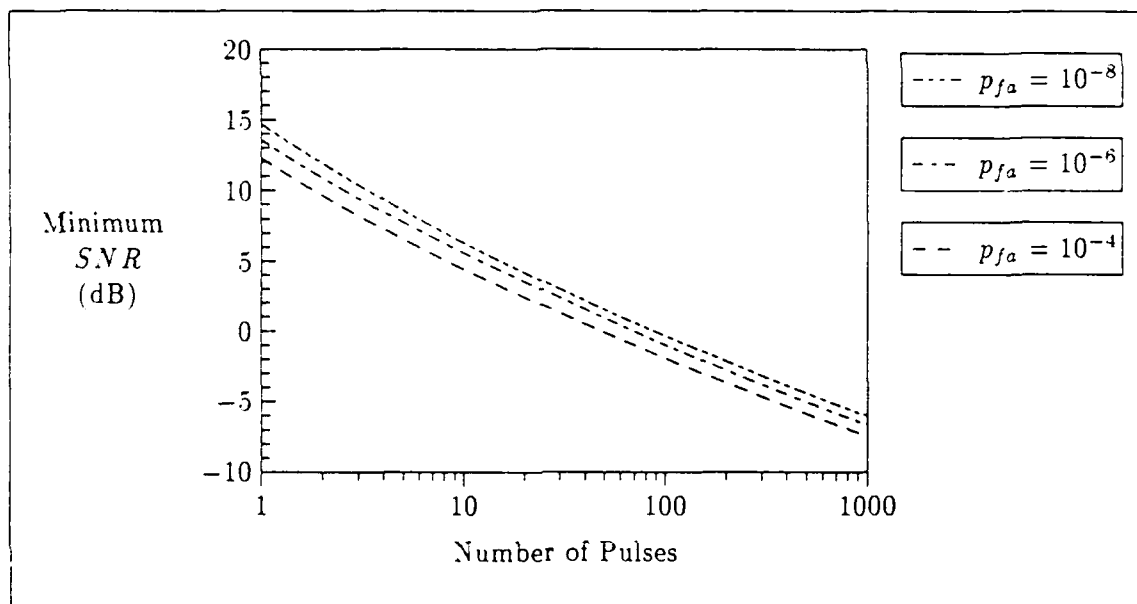


Figure 16. Minimum SNR Requirement using Post-Detection Multi-Pulse Integration, and $p_d = 0.95$ for various p_{fa} (Extracted from Skolnik (73:2-21))

A relation between SNR and system parameters is required so that design variables can be adjusted to achieve a desired p_d and p_{fa} . Assuming that the noise contributions are uncorrelated, SNR at the detector can be defined in terms of generated photocurrent (19:2399):

$$SNR = \frac{\langle i_s \rangle^2}{\sum_n \langle i_n \rangle^2} \quad (20)$$

where $\langle i_s \rangle$ is the mean photocurrent generated by the detected IF signal, and $\langle i_n \rangle$ is the mean photocurrent generated by the n^{th} noise process.

In a shot-noise limited system, SNR reduces to

$$SNR = \frac{\langle i_s \rangle^2}{\langle i_q \rangle^2} \quad (21)$$

where $\langle i_q \rangle$ is the mean photocurrent generated by LO-induced shot noise.

The shot noise current term of Equation (21) can be determined by considering the amount of LO power converted to noise photocurrent over the detector and IF passband. Therefore, $\langle i_q \rangle^2$ may be written as (8:111, 73:37-37)

$$\langle i_q \rangle^2 = \frac{\langle P_{lo} \rangle \eta_q \lambda B q^2}{hc} \quad (22)$$

where

$\langle P_{lo} \rangle$ is the mean LO power,

η_q is the detector quantum efficiency,

λ is the photon wavelength,

B is the detector and IF bandwidth,

q is the charge per electron,

h is Planck's constant, and

c is the speed of light.

The signal photocurrent term of Equation (21) can be determined by using the IF component of the photo-mixed received and LO signals. Thus, $\langle i_s \rangle^2$ may be written as (19:2399; 73:37-38)

$$\langle i_s \rangle^2 = \langle P_{if} \rangle^2 \left(\frac{q \eta_q \lambda}{hc} \right)^2 \quad (23)$$

or

$$\langle i_s \rangle^2 = \langle P_{lo} \rangle \langle P_r \rangle \left(\frac{q \eta_q \lambda}{hc} \right)^2 \quad (24)$$

where $\langle P_{if} \rangle$ and $\langle P_r \rangle$ are the mean IF power and mean received signal powers, respectively.

Therefore, using Equations (21), (22), and (24), SNR may be expressed by

$$SNR = \frac{\langle P_r \rangle \lambda \eta_q}{hcB} \quad (25)$$

Equation (25) implies that, for selected detector hardware and wavelength in a shot-noise limited system, the SNR value is determined solely by received power. In this situation, p_d and p_{fa} now depend directly on $\langle P_r \rangle$. The value of $\langle P_r \rangle$ is commonly expressed in terms of transmitter and receiver parameters, target characteristics, and transmission properties using the *LADAR Equation* (73:1-4; 37-4).

The LADAR Equation

Several forms of the LADAR Equation are used in the literature (41; 88; 8; 6), their primary differences being related to detection of either a 'resolved' target (transmitted beamwidth smaller than the target dimension), or 'unresolved' target (beamwidth larger than the target). Since the extremely long ranges considered in this analysis mean that targets will be unresolved, the following form of the LADAR Equation from Lange and Evans will be used (48:156):

$$\langle P_r \rangle = \left[\frac{P_t G_t \tau_{lo} \tau_A}{4\pi R^2} \right] \sigma_{lc} \left[\frac{\tau_A \lambda^2 G_r \tau_{ro}}{(4\pi R)^2} \right] \quad (26)$$

where

P_t is the transmitter power,

G_t is the transmitter power gain,

τ_{to} is the transmitter optics transmittance,

τ_A is the one-way atmospheric transmittance,

R is the range to the target,

σ_{lcs} is the target LADAR cross-section,

G_r is the receiver power gain, and

τ_{ro} is the receiver optics transmittance.

Equation (26) has been expressed for co-located transmitter and receiver, but with possibly different transmitter and receiver optics. The first term in Equation (26) represents the amount of power in the transmitted antenna pattern at the target's range. The last term represents the amount of power reflected from the target which is detected by the receiver.

Variations in $\langle P_r \rangle$ will occur from detection to detection due to differences in target and atmospheric characteristics. These variations will appear in the terms τ_A , σ_{lcs} , and R . Additional variations arise in the antenna gain terms, G_t and G_r , depending on the location of the target within the antenna beamwidth. Selection of a suitable transmitter laser and optics will serve to define the 'fixed' terms in the LADAR Equation — P_t , λ , τ_{to} , and τ_{ro} . However, expressions for transmitter and receiver antenna power gain require further analysis.

Transmitter Antenna Gain

The characteristics of the antenna which explicitly affect LADAR performance are represented by the gain term of the LADAR Equation, which is analogous to the gain of conventional microwave radars. Gain describes the ability of an antenna to concentrate transmitter energy in a given direction and, in particular, *power gain* also accounts for *all losses* associated with the antenna (73:9-5). Antenna power

gain may then be written as (73:9-12)

$$G_t = \frac{4\pi A_t}{\lambda^2} \eta_t \quad (27)$$

where A_t is the transmitter antenna primary aperture area, and η_t is the transmitter antenna efficiency.

The term $4\pi A_t/\lambda^2$ is the ideal gain term formulated by Silver for a uniformly irradiated, unobscured circular aperture with no losses (71:177). Since ideal gain represents the maximum possible gain, η_t represents all losses associated with truncation of the transmitted laser beam by the antenna aperture, obscuration by secondary telescope elements, and diffraction effects in the radiated pattern (43:2134-2135).

Determination of η_t requires analysis of the radiated antenna power pattern. This radiation pattern can be characterized by the Poynting vector, \mathbf{S} , which represents the irradiance on any surface perpendicular to the direction of electric and magnetic fields (10:9). This irradiance has a magnitude which is proportional to the square of the magnitude of the scalar field derived using the Fresnel-Kirchoff diffraction formula (73:9-7), and has an average value of (50:465)

$$\langle S \rangle = \frac{1}{2} c \epsilon_0 E^2 \quad (28)$$

where ϵ_0 is the permittivity of free-space, and E is the peak amplitude of the electric field.

For this analysis, the Poynting vector definition may be used in the development of an expression for the far-field radiation pattern resulting from laser beam transmission through an optical telescope. To assist with this development, consider an aperture irradiated by a wave, $E(\xi, \eta)$, generated from point P_0 on the telescope axis, as shown in Figure 17. The resultant scalar diffraction field at point P , $U(P)$, is found by integration over the aperture area of all area elements, $d\xi d\eta$, which com-

prise the aperture field. $U(P)$ is given by the Fresnel-Kirchoff diffraction integral as (10:382; 73:9-7)

$$U(P) = -\frac{j}{2\lambda} \iint_{\text{AREA}} E(\xi, \eta) \frac{e^{jks}}{s} [\cos(\hat{n}, \hat{r}) - \cos(\hat{n}, \hat{s})] d\xi d\eta \quad (29)$$

where

$$k = 2\pi/\lambda,$$

s is the distance from the aperture to the observation point.

(\hat{n}, \hat{r}) is the angle between the aperture normal and the \hat{r} direction, and

(\hat{n}, \hat{s}) is the angle between the aperture normal and the \hat{s} direction.

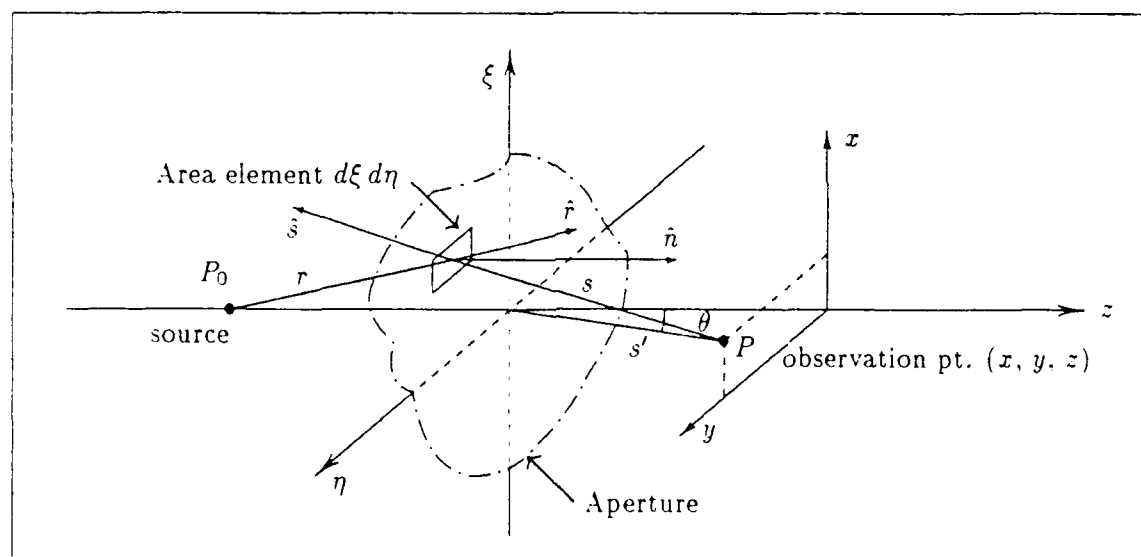


Figure 17. LADAR Transmitter Aperture Geometry

Several simplifications to Equation (29) can be made when considering LADAR applications. First, the far-field regime of an antenna pattern is conventionally defined as starting from a range of $2D^2/\lambda$ to infinity, where D is the primary aperture diameter (73:9-9). For the range of values of D and λ under consideration, the far field region extends outward from a range of between 20 and 250 kilometers. These values allow confinement of the analysis to far-field radiated power, so that

$(\hat{n}, \hat{s}) \approx \pi$. Additionally, since LADAR telescopes concentrate energy along the z axis, $(\hat{n}, \hat{r}) \approx 0$. Therefore, Equation (29) reduces to

$$U(P) = -\frac{j}{\lambda} \iint_{AREA} E(\xi, \eta) \frac{e^{jks}}{s} d\xi d\eta \quad (30)$$

Furthermore, the distances s and s' can be written in terms of Cartesian coordinates as

$$\left. \begin{aligned} s &= [(x - \xi)^2 + (y - \eta)^2 + z^2]^{1/2} \\ s' &= (x^2 + y^2 + z^2)^{1/2} \end{aligned} \right\} \quad (31)$$

Hence

$$s = (s'^2 + \eta^2 + \xi^2 - 2x\xi - 2y\eta)^{1/2} \quad (32)$$

In the far-field regime, the binomial expansion can be used to obtain the following approximation for s and $1/s$ (13:20,10:383):

$$\left. \begin{aligned} s &\approx s' - (x\xi + y\eta)/s' \\ 1/s &\approx 1/s' \end{aligned} \right\} \quad (33)$$

where the approximation for s is used in the exponential term and $1/s$ is used for the amplitude term. Note that s cannot be approximated by s' in the exponential transverse-phase term since the effect of neglecting the smaller terms is amplified through multiplication and the exponential power effect (13:20). Using these approximations, Equation (30) may be written as

$$U(P) = -\frac{j e^{jks'}}{\lambda s'} \iint_{AREA} E(\xi, \eta) \exp \left[-\frac{jk}{s'} (x\xi + y\eta) \right] d\xi d\eta \quad (34)$$

As outlined in Chapter III, the candidate system under consideration includes a secondary telescope element which partly obscures the transmitted and received signal. An example of such a design is illustrated in Figure 4 in Chapter III, showing

a typical Cassegrainian arrangement. Since this analysis assumes diffraction at an obscured circular aperture, polar coordinates are appropriate in representing points in the radiation pattern. The following substitutions will be used for the points (ρ, ψ) in the aperture, and (ρ', ψ') in the observation plane:

$$\left. \begin{aligned} \xi &= \rho \cos \psi & \eta &= \rho \sin \psi \\ x &= \rho' \cos \psi' & y &= \rho' \sin \psi' \end{aligned} \right\} \quad (35)$$

Using Equation (34), and replacing s' by $\rho'/\sin \theta$ in the argument of the integral's exponential function, the scalar field becomes

$$U(P) = -\frac{j e^{jks'}}{\lambda s'} \int_0^{2\pi} \int_b^a E(\rho, \psi) e^{-jk\rho \sin \theta \cos(\psi - \psi')} \rho d\rho d\psi \quad (36)$$

where a is the primary aperture radius, b is the secondary aperture radius, and the difference-of-cosines identity has been used to simplify the exponential argument.

The form of Equation (36) can be further simplified by using the Bessel function integral relation (10:395):

$$\frac{j^{-n}}{2\pi} \int_0^{2\pi} e^{jx \cos \beta} e^{jn\beta} d\beta = J_n(x) \quad (37)$$

where the Bessel function of the first kind of order zero, $J_0(x)$, is required.

Additionally, if the incident field amplitude is circular symmetric and, therefore, independent of ψ , Equation (36) becomes

$$U(P) = -\frac{jk e^{jks'}}{s'} \int_b^a E(\rho) J_0(k\rho \sin \theta) \rho d\rho \quad (38)$$

This expression represents the scalar field at a point in the far-field of an obscured circular aperture. The incident field, $E(\rho)$, can be described by a Gaussian amplitude function corresponding to the fundamental TEM₀₀ laser mode. The

following representation of $E(\rho)$ is taken from Klein and Degnan and is corrected to include the free-space impedance term, $1/(c\epsilon_0)$, in the normalization constant (43:2135):

$$E(\rho) = C_0 \exp\left(\frac{\rho^2}{\omega^2}\right) \exp\left(-\frac{jk\rho^2}{2R_s}\right) \quad (39)$$

where

$C_0 = 2/(\pi\omega^2 c\epsilon_0)^{1/2}$ is the normalization constant,

ω is the beam radius, measured from the axis to the $1/\epsilon^2$ power point, and

R_s is the phase-front curvature at the aperture.

The normalization constant is chosen so that the incident power, P_{inc} , over the entire aperture plane is unity. This may be expressed mathematically using the following expression — also taken from Klein and Degnan and corrected for free-space impedance (43:2135):

$$P_{inc} = \frac{c\epsilon_0}{2} \int_0^{2\pi} \int_0^a |E(\rho)|^2 \rho d\rho d\psi = 1 \quad (40)$$

Using Equation (39), the propagating field distribution can be determined at a distance s' from the aperture to be

$$E(\rho) = C_0 \exp\left(-\frac{\rho^2}{\omega^2}\right) \exp\left[-\frac{jk\rho^2}{2} \left(\frac{1}{s'} + \frac{1}{R_s}\right)\right] \quad (41)$$

Combining this result with Equation (38) provides the field distribution at a distant observation point, P , resulting from irradiation of an obscured circular aperture by a Gaussian field. This distribution is given by

$$U(P) = -\frac{j2k e^{jk s'}}{s'(\pi\omega^2 c\epsilon_0)^{1/2}} \int_0^a \exp\left(-\frac{\rho^2}{\omega^2}\right) \exp\left[-\frac{jk\rho^2}{2} \left(\frac{1}{s'} + \frac{1}{R_s}\right)\right] J_0(k\rho \sin \theta) \rho d\rho \quad (42)$$

Based on the Poynting vector definition of Equation (28), the irradiance distribution at P can now be expressed by

$$I(P) = \frac{c\epsilon_0}{2} |U(P)|^2 \quad (43)$$

The antenna power gain can then be expressed in terms of irradiance using Klein and Degnan's definition as follows (43:2135):

$$G_t(s', \theta) = \frac{I(s', \theta)}{I_o} \quad (44)$$

where I_o is defined as the irradiance at a distance s' from a unit power isotropic radiator (since the incident field has been normalized to unit power), and is given by (43:2135)

$$I_o = \frac{1}{4\pi s'^2} \quad (45)$$

Combining Equations (42), (43), (44), and (45), the transmitter antenna gain can be written as

$$G_t(s', \theta) = \frac{8k^2}{\omega^2} \left| \int_b^a \exp\left(-\frac{\rho^2}{\omega^2}\right) \exp\left[-\frac{jk\rho^2}{2} \left(\frac{1}{s'} + \frac{1}{R_z}\right)\right] J_0(k\rho \sin \theta) \rho d\rho \right|^2 \quad (46)$$

This result agrees with the gain expression given by Klein and Degnan, since the free-space impedance terms cancel. Equation (46) can be further simplified for the far-field by setting $(1/s' + 1/R_z)$ to zero, since phase-front curvature has infinite radius in the far-field. This simplifies Equation (46) to

$$G_t(X) = \frac{4\pi A_t}{\lambda^2} 2\alpha^2 \left| \int_{\gamma^2}^1 e^{-\alpha^2 u} J_0(Xu^{1/2}) du \right|^2 \quad (47)$$

where

$$X = ka \sin \theta = \text{off-axis parameter,}$$

$A_t = \pi a^2$ = area of primary aperture,

$\alpha = a/\omega$,

$\gamma = b/a$ = obscuration ratio, and

$u = \rho^2/a^2$.

Comparison between Equations (27) and (47) allows transmitter efficiency to be written as

$$\eta_t = 2\alpha^2 \left| \int_{\gamma^2}^1 e^{-\alpha^2 u} J_0(Xu^{1/2}) du \right|^2 \quad (48)$$

Depending on the laser beam radius used, different values of gain can be achieved. This variable can be eliminated from Equation (48) by finding the α value corresponding to maximum on-axis gain as a function of γ . Setting X equal to zero and performing the Equation (47) integration to determine an expression for on-axis gain yields

$$G_t(0) = \frac{4\pi A_t}{\lambda^2} 2\alpha^2 (e^{-\alpha^2} - e^{-\alpha^2 \gamma^2})^2 \quad (49)$$

Equation (49) can be differentiated and set to zero to find an optimum expression for α in terms of γ . Using second order perturbation theory, Klein and Degnan obtained the following solution, accurate to within $\pm 1\%$ for $\gamma \leq 0.4$ (43:2136):

$$\alpha \approx 1.12 - 1.30\gamma^2 + 2.12\gamma^4 \quad (50)$$

Using this expression for α in Equation (48) allows transmitter efficiency to be determined as a function of the off-axis parameter, X , for a specific obscuration ratio. Figure 18 shows Equation (48) plotted for three values of γ . Efficiency is seen to be degraded significantly for values of X above 0.5. For example, a transmitter aperture of 60 cm diameter with 20% obscuration, and a wavelength of 5 μm , will have a radiated power pattern which is theoretically degraded from boresight gain by about 6 dB at 3 microradians off-axis.

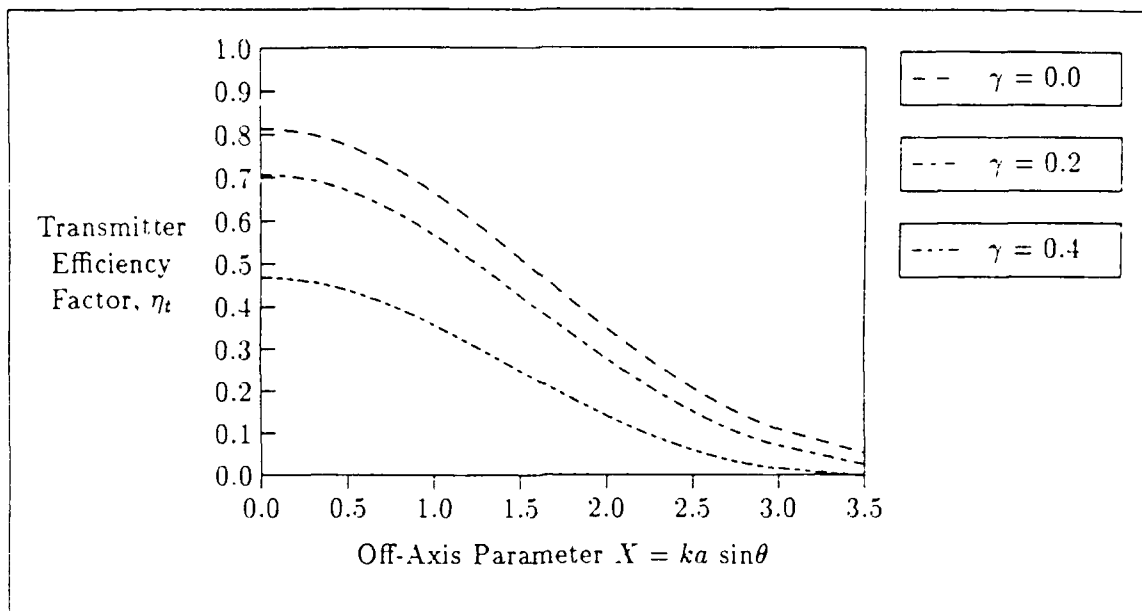


Figure 18. Transmitter Efficiency Variation against Off-Axis Parameter

Receiver Antenna Gain

Using the reciprocity theorem of Helmholtz (10:381), gain for a given antenna is the same for receiving or transmitting operations, provided the same source is used. In this analysis, however, the transmitter source function follows a Gaussian amplitude distribution, whereas the received signal from a far-field point source consists of plane waves at the aperture. Therefore, assuming aberration-free optics with perfect transmission (since optics transmittance is already included in the τ_{to} and τ_{ro} terms of the LADAR Equation), the only losses in a receiver antenna are those due to obscuration and photon detection efficiency at the focal plane. This may be expressed mathematically as

$$G_r = \frac{4\pi A_r}{\lambda^2} \eta_r = \frac{4\pi A_r}{\lambda^2} (1 - \gamma^2) \eta_H \quad (51)$$

where A_r is the receiver antenna primary aperture area, η_r is the receiver antenna efficiency factor, and η_H is the heterodyne detection efficiency.

In a similar manner to transmitter efficiency, receiver efficiency can be analyzed by considering the radiation pattern at the focal plane. Using the geometry of Figure 19, the incident signal at the receiver aperture consists of infinite plane waves of the form

$$E(z) = E_{r_0} e^{jkz} \quad (52)$$

where z is the distance along the telescope axis, and E_{r_0} is the peak amplitude.

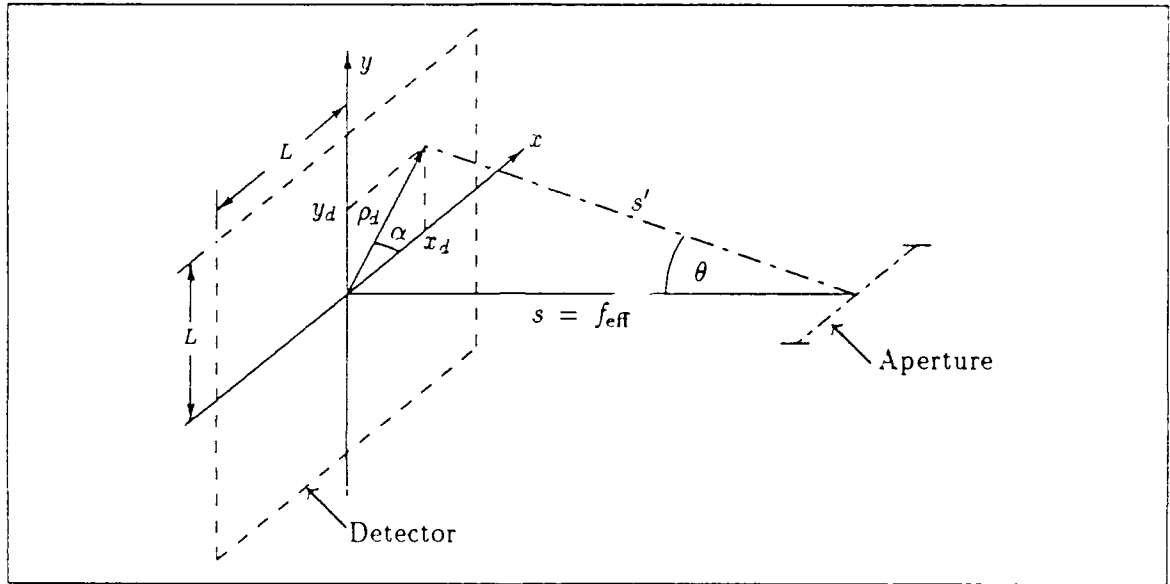


Figure 19. Detector Geometry

Equation (38) can then be used to obtain an expression for the field incident on the focal plane as follows:

$$E_r(\rho) = -\frac{jkE_{r_0} e^{jk(s' + z)}}{s'} \int_b^a J_0(k\rho \sin \theta) \rho d\rho \quad (53)$$

where ρ is the radial coordinate in the aperture plane.

Integration can be completed using the following recurrence relation for Bessel functions (10:395):

$$\frac{d}{dx} \{x^{n+1} J_{n+1}(x)\} = x^{n+1} J_n(x) \quad (54)$$

Thus, Equation (53) produces

$$E_r(\rho) = -\frac{jkEr_o e^{jk(s' + z)}}{s'} \left[\frac{a J_1(ka \sin \theta)}{k \sin \theta} - \frac{b J_1(kb \sin \theta)}{k \sin \theta} \right] \quad (55)$$

where J_1 is the Bessel function of the first kind of order one.

Using the nomenclature of Figure 19, where ρ_d is the radial coordinate in the detector plane located at the effective focal length, f_{eff} , from the aperture, the scalar field magnitude at the detector can be written as

$$|E_r(\rho_d)| = \frac{Er_o}{\rho_d} \left[a J_1 \left(\frac{ka\rho_d}{f_{\text{eff}}} \right) - b J_1 \left(\frac{kb\rho_d}{f_{\text{eff}}} \right) \right] \quad (56)$$

or, in Cartesian coordinates:

$$|E_r(x_d, y_d)| = \frac{Er_o}{(x_d^2 + y_d^2)^{1/2}} \left\{ a J_1 \left[\frac{ka(x_d^2 + y_d^2)^{1/2}}{f_{\text{eff}}} \right] - b J_1 \left[\frac{kb(x_d^2 + y_d^2)^{1/2}}{f_{\text{eff}}} \right] \right\} \quad (57)$$

where x_d and y_d are the Cartesian coordinates in the detector plane.

The form of Equation (57) is seen to be that of an Airy pattern modified by the diffraction pattern due to the central obscuration. The resultant Airy disk radius, R_A , is defined as the distance from the center of the Airy pattern to the first null. That is, substituting R_A for $(x_d^2 + y_d^2)^{1/2}$ in Equation (57) produces the condition of zero field magnitude, which can be written as

$$J_1(\sigma) - \gamma J_1(\gamma\sigma) = 0 \quad (58)$$

where $\sigma = \frac{k R_A}{2F_s}$, with $F_s = \frac{f_{\text{eff}}}{2a}$ = antenna F-number.

Equation (58) relates Airy disk radius, antenna F-number, and obscuration ratio, which is expressed graphically in Figure 20. For a constant F-number, the size

of the central Airy disk decreases as the size of the secondary telescope element is enlarged.

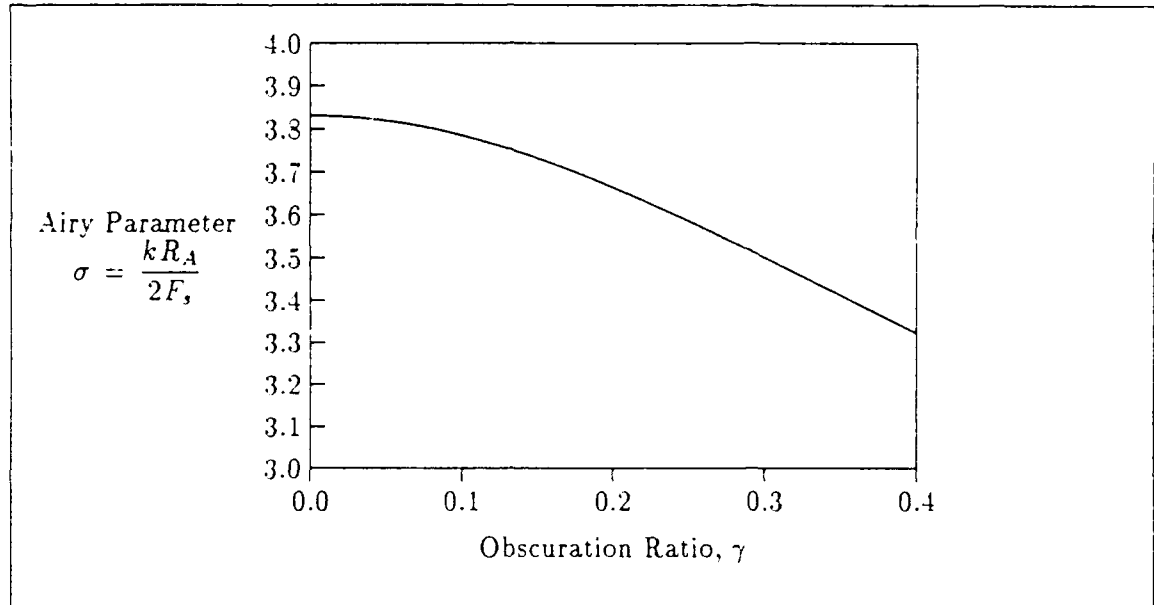


Figure 20. Airy Size Parameter Variation with Obscuration Ratio

The incident field described by Equation (57) mixes with the LO field at the detector face. The irradiance on the detector surface is given by the superposition of received and LO fields, and can be expressed using the time-varying representation of the incident fields (19:2398) as follows:

$$I(\rho_d, t) = \frac{c\epsilon_o}{2} \left[\Re \left\{ E_r(\rho_d) e^{j\omega_t t} \right\} + \Re \left\{ E_l(\rho_d) e^{j(\omega_l t - \phi)} \right\} \right]^2 \quad (59)$$

where $\Re\{\dots\}$ denotes the real component, ω_t and ω_l are the approximately-equal transmitter and LO angular frequencies, and ϕ is an arbitrary phase difference between the two signals.

Note that Equation (59) is a simplistic model since perfect phase-front alignment between the two signals is assumed. In practice, this assumption may be difficult to realize, particularly at short wavelengths, since the maximum allowable

'lag angle' between the two beams for efficient coherent detection is directly proportional to wavelength (82:3427). Therefore, the assumption of perfect alignment will be relaxed in a later section so that misalignment effects can be examined separately. With this assumption, Equation (59) may be expressed, after some algebra, as

$$I(\rho_d, t) = \frac{c\epsilon_o}{2} \left\{ \frac{E_r^2(\rho_d)}{2} + \frac{E_l^2(\rho_d)}{2} + E_r(\rho_d) E_l(\rho_d) \cos [(\omega_t - \omega_l) t + \phi] \right. \\ \left. + \frac{E_r^2(\rho_d)}{2} \cos(2\omega_l t) + \frac{E_l^2(\rho_d)}{2} \cos [2(\omega_l t - \phi)] \right. \\ \left. + E_r(\rho_d) E_l(\rho_d) \cos [(\omega_t + \omega_l) t - \phi] \right\} \quad (60)$$

The first term in Equation (60), which represents the amplitude of the received signal, may be neglected in comparison to the amplitude of the LO signal. The last three terms in Equation (60), which represent signal components of about $2\omega_l$, can also be neglected since they are outside the detector bandpass. Therefore, Equation (60) can be simplified to

$$I(\rho_d, t) = \frac{c\epsilon_o}{2} \left\{ \frac{E_l^2(\rho_d)}{2} + E_r(\rho_d) E_l(\rho_d) \cos [(\omega_t - \omega_l) t + \phi] \right\} \quad (61)$$

The instantaneous signal power corresponding to this irradiance can be expressed as four times the power from one detector quadrant. That is,

$$P(t) = 4 \int_0^L \int_0^L I(x_d, y_d, t) dx_d dy_d \quad (62)$$

where the detector dimensions are $2L \times 2L$, or

$$P(t) = c\epsilon_o \int_0^L \int_0^L |E_l(x_d, y_d)|^2 dx_d dy_d \\ + 2c\epsilon_o \int_0^L \int_0^L |E_r(x_d, y_d) E_l(x_d, y_d)| \cos [(\omega_t + \omega_l)t + \phi] dx_d dy_d \quad (63)$$

The first term in Equation (63) can be interpreted as the mean LO power, while the second term is the instantaneous IF power. That is,

$$P(t) = \langle P_{lo} \rangle + P_{if}(t) \quad (64)$$

The power equations presented thus far are sufficient to determine an expression for receiver heterodyne efficiency, η_H . Heterodyne efficiency can be defined as the *actual* signal detected, divided by the maximum possible signal. The maximum signal possible is achieved with perfect mixing of the LO beam and the power received at the aperture. This received aperture power may be described by (19:2398)

$$\langle P_r \rangle = \frac{c\epsilon_o}{2} E_{r_o}^2 (\pi a^2)(1 - \gamma^2) \quad (65)$$

If the actual detected signal power is characterized by the IF power, then the heterodyne efficiency may be expressed in a dimensionless form as follows:

$$\eta_H = \frac{\langle P_{if} \rangle^2}{\langle P_r \rangle \langle P_{lo} \rangle} \quad (66)$$

Using Equations (63) and (64), the mean square IF power is extracted as

$$\langle P_{if} \rangle^2 = \frac{1}{2} \left[2c\epsilon_o \int_0^L \int_0^L |E_r(x_d, y_d) E_l(x_d, y_d)| dx_d dy_d \right]^2 \quad (67)$$

The explicit expression for $E_r(x_d, y_d)$ may now be substituted from Equation (57), and terms re-arranged to obtain

$$\begin{aligned} \langle P_{if} \rangle^2 = \langle P_r \rangle \frac{4c\epsilon_o}{\pi(1 - \gamma^2)} & \left| \int_0^L \int_0^L \frac{E_l(x_d, y_d)}{(x_d^2 + y_d^2)^{1/2}} \left[J_1 \left(\frac{k(x_d^2 + y_d^2)^{1/2}}{2F_s} \right) \right. \right. \\ & \left. \left. - \gamma J_1 \left(\gamma \frac{k(x_d^2 + y_d^2)^{1/2}}{2F_s} \right) \right] dx_d dy_d \right|^2 \quad (68) \end{aligned}$$

Heterodyne efficiency may then be found from Equation (66) using the $\langle P_o \rangle$ term from Equations (63) and (64), and the term $\langle P_{if} \rangle^2 / \langle P_r \rangle$ from Equation (68). Using a generalized form for the LO distribution, the expression for η_H is now

$$\eta_H = \left| \int_0^L \int_0^L \frac{E_l(x_d, y_d)}{(x_d^2 + y_d^2)^{1/2}} \left\{ J_1 \left[\frac{k(x_d^2 + y_d^2)^{1/2}}{2F_s} \right] - \gamma J_1 \left[\gamma \frac{k(x_d^2 + y_d^2)^{1/2}}{2F_s} \right] \right\} dx_d dy_d \right|^2 \times \frac{4}{\pi(1 - \gamma^2) \left| \int_0^L \int_0^L E_l(x_d, y_d) dx_d dy_d \right|^2} \quad (69)$$

Equation (69) is similar in form to that of Degnan and Klein (19:2399), except that a circular detector and polar coordinates led to a simpler expression in their analysis. A choice of normalized variables in similar vein to Degnan and Klein provides a simpler form of Equation (69) for further analysis and plotting, as follows:

$$\eta_H = \left| \int_0^{\sigma r} \int_0^{\sigma r} \frac{E_l(x, y)}{(x^2 + y^2)^{1/2}} \left\{ J_1 \left[(x^2 + y^2)^{1/2} \right] - \gamma J_1 \left[\gamma (x^2 + y^2)^{1/2} \right] \right\} dx dy \right|^2 \times \frac{4}{\pi(1 - \gamma^2) \left| \int_0^{\sigma r} \int_0^{\sigma r} E_l(x, y) dx dy \right|^2} \quad (70)$$

where

$$x = kx_d/(2F_s),$$

$$y = ky_d/(2F_s), \text{ and}$$

$$r = L/R_A.$$

Equation (70) shows that careful selection of an LO distribution will optimize heterodyne efficiency. Maximum efficiency is obtained when the spatial distribution of the LO signal exactly matches the received signal (82:3422). This situation could only be realized for the case under study by enlarging the LO beam and focusing it through a centrally obscured aperture onto the detector (19:2401).

Two other LO distributions, which are simpler to implement, are the Gaussian and uniform profiles (82, 19, 41). The Gaussian LO distribution would be used in LADARs where a single detector, or quadrant tracking detector, is used in the focal plane. The LO beam irradiance on the detector would then be adjusted so that the LO beam diameter is of the same order of magnitude as the detector width.

The uniform LO distribution represents the case where either the LO beam diameter is much greater than the single detector width, or where a mosaic focal plane array is used. In order to adequately irradiate the entire array, the LO beam diameter is increased to cover all array pixels, thereby causing the LO distribution over each pixel to be approximately uniform. For the FPA case, a Gaussian LO distribution for each pixel would more closely match the received Airy pattern than a uniform LO beam, but would be difficult to implement. The difference in performance between the two cases will be examined more closely, using Equation (70) as the basis.

Gaussian LO Distribution. For the Gaussian case, the LO beam can be described in a similar fashion to Equation (39). Using an arbitrary peak amplitude of C_1 , the LO amplitude is

$$|E_l(x, y)| = C_1 e^{-\frac{(x^2 + y^2)}{\omega_L^2}} \quad (71)$$

where ω_L is the LO beam radius, measured from the axis to the $1/e^2$ power point. Assuming that the Gaussian LO beam and the Airy disk share the same center, η_H may then be written as

$$\eta_H = \left| \int_0^{\sigma r} \int_0^{\sigma r} \frac{e^{-\frac{t^2(x_1^2 + y_1^2)}{\sigma^2}}}{(x_1^2 + y_1^2)^{1/2}} \left\{ J_1 \left[(x_1^2 + y_1^2)^{1/2} \right] - \gamma J_1 \left[\gamma (x_1^2 + y_1^2)^{1/2} \right] \right\} dx_1 dy_1 \right|^2 \times \frac{4}{\pi(1 - \gamma^2) \left| \int_0^{\sigma r} \int_0^{\sigma r} e^{-\frac{2\gamma^2(x_1^2 + y_1^2)}{\sigma^2}} dx_1 dy_1 \right|^2} \quad (72)$$

where $t = R_A/\omega_L$.

Note that η_H only depends on distribution of the LO signal, and is independent of LO amplitude.

The solution to Equation (72) may be found numerically for a given ratio of detector dimension to Airy disk radius, r , and a specific obscuration ratio, γ . Knowing γ enables the determination of σ via Equation (58). However, in calculating η_H using Equation (72), the ratio of Airy disk radius to LO beam radius, t , must be optimized for maximum heterodyne efficiency. Therefore, an iterative technique is required to determine the optimum value of t for each combination of r and γ , so that maximum heterodyne efficiency can then be calculated.

Variation in the optimum t value is shown against r in Figure 21 for different obscuration ratios. As r increases, corresponding to increasing detector size for fixed Airy radius, the LO beam radius, ω_L , must decrease for optimum heterodyne efficiency. This is because more of the Gaussian tail is being captured by the detector, which increases shot noise, but not the signal level.

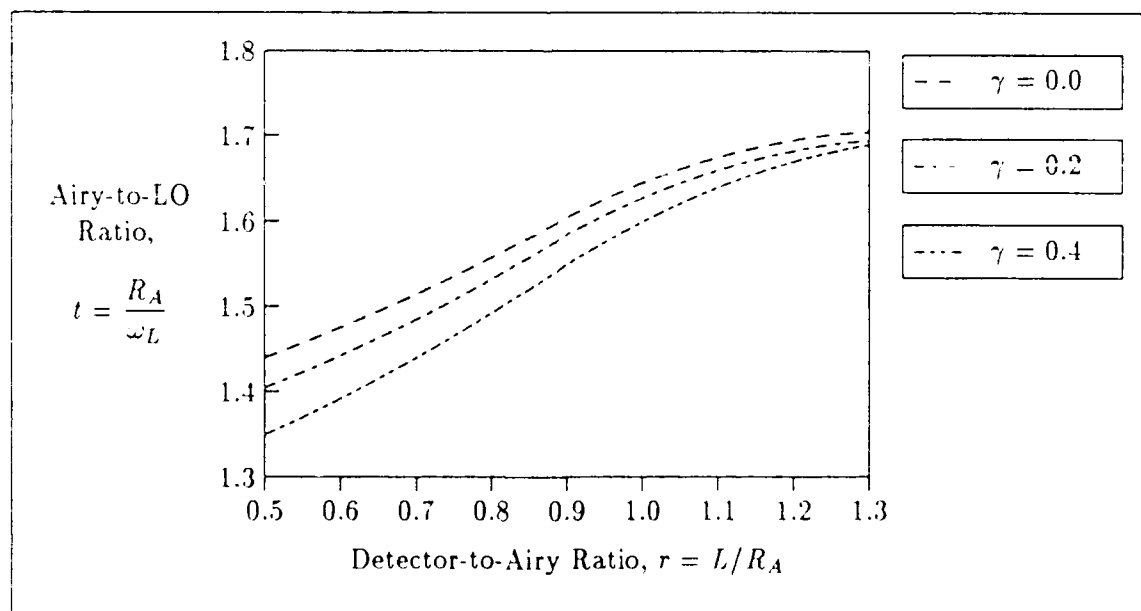


Figure 21. Optimum Airy-to-LO Ratio versus Detector-to-Airy Ratio for Gaussian LO Distribution

The corresponding curves for η_H are shown in Figure 22. As the detector size increases, more of the Airy pattern is received, which increases efficiency. As L/R_A increases above 0.835, however, the additional shot noise generated from capturing more LO irradiance tends to dominate any gain in received Airy signal. This is due to the more rapid fall-off in Airy pattern power as opposed to the Gaussian LO distribution.

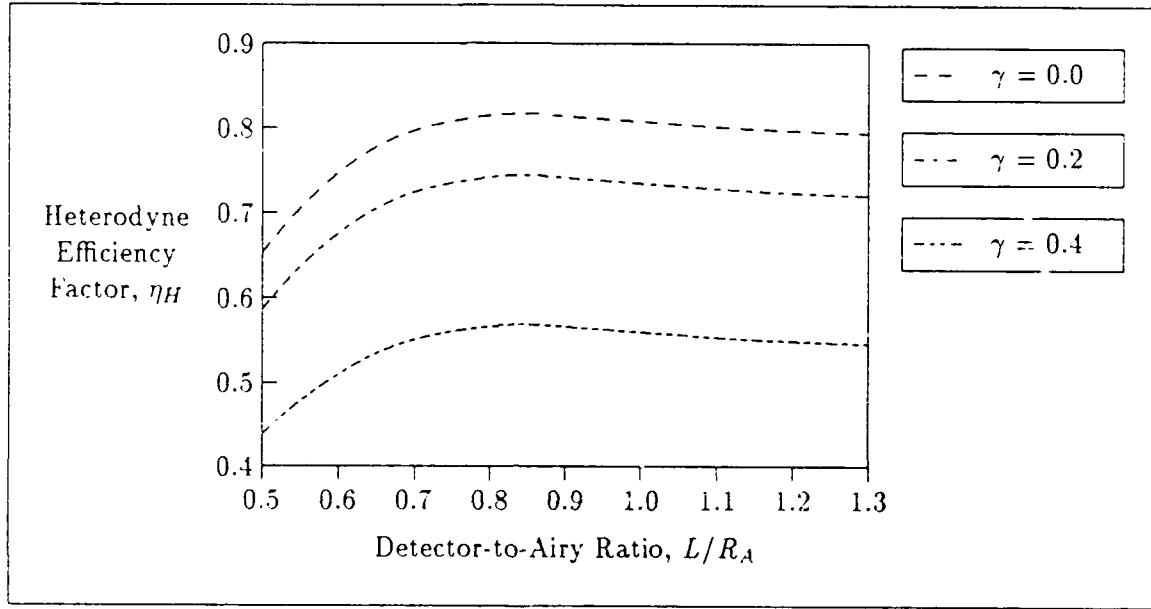


Figure 22. Heterodyne Efficiency versus Detector-to-Airy Ratio for Gaussian LO

Uniform LO Distribution. For the case of a uniform LO distribution, Equation (70) becomes

$$\eta_H = \frac{4 \left| \int_0^{\sigma r} \int_0^{\sigma r} \frac{J_1 \left[(x_1^2 + y_1^2)^{1/2} \right] - \gamma J_1 \left[\gamma (x_1^2 + y_1^2)^{1/2} \right]}{(x_1^2 + y_1^2)^{1/2}} dx_1 dy_1 \right|^2}{\pi(1 - \gamma^2)\sigma^2 r^2} \quad (73)$$

Figure 23 shows η_H plotted against r for specific values of γ . The optimum ratio of detector-to-Airy size is seen to be approximately 0.635. This value can be interpreted similarly to the Gaussian case as a trade-off between signal power and

LO-induced shot noise. As the detector size is increased from $r = 0.3$, more Airy pattern irradiance is available to mix with LO irradiance, thereby providing higher efficiency. However, as the detector size is increased beyond $r = 0.635$ to capture the much lower irradiance in the 'wings' of the central Airy disk, additional shot noise generated from the uniform LO irradiance starts to degrade performance. This effect is more pronounced in a square detector when compared to a circular detector, such as that analyzed by Degnan and Klein (which yielded an optimum r value of 0.75), due to the growing 'bare' corner areas on the square detector which receive predominantly LO irradiance.

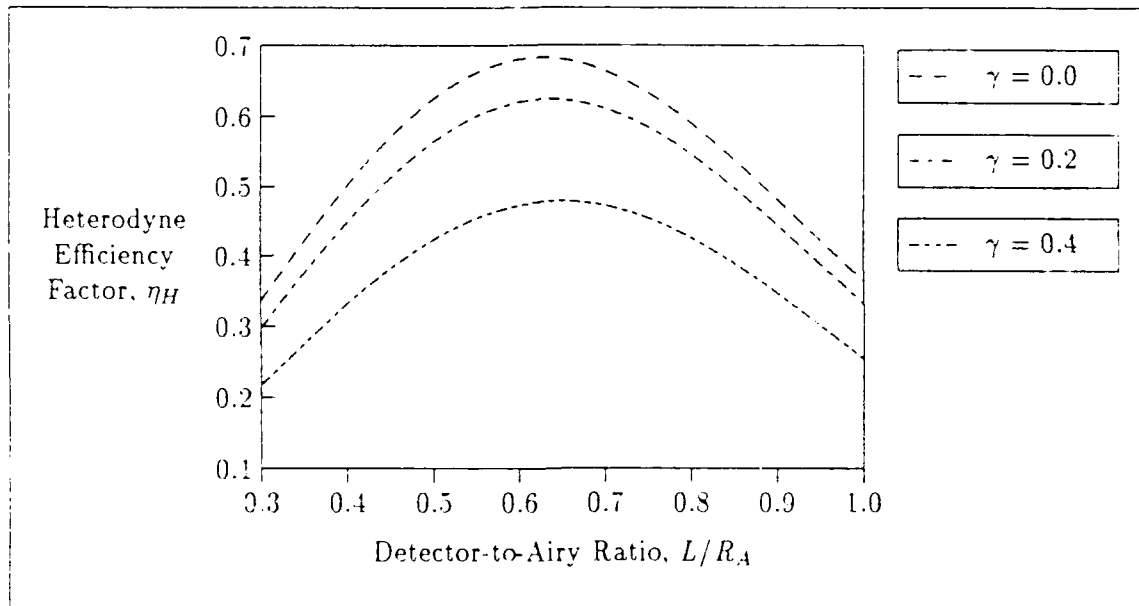


Figure 23. Heterodyne Efficiency versus Detector-to-Airy Ratio, for Uniform LO

Comparison of Figures 22 and 23 shows that, for optimum detector size and obscuration ratio, use of a uniform LO distribution will decrease heterodyne efficiency to a level of about 85% of the efficiency gained from using a Gaussian LO. This represents a loss of about 0.7 dB in receiver gain.

Phase Front Misalignment. The preceding efficiency equations developed for both Gaussian and uniform LO distributions have assumed perfect alignment be-

tween received beam and LO beam phase fronts. As discussed previously, close physical alignment of optics and detector is difficult, but possible. However, misalignment may also occur in a normal detection event, depending on target location. Energy reflected from targets located off the boresight axis may still be successfully detected, due to the width of the receiver antenna beam in the far-field. This energy will arrive back at the receiver aperture as a plane wave inclined at an angle to the aperture plane. Figure 24 shows the resultant relationship between the LO beam incident on the detector surface, and the incoming signal (82:3422). The wave vector, \mathbf{k} , represents the received beam with a different phase to the LO beam, where the LO beam is parallel to the z axis. When the returned signal is received from a diffuse target, the detection efficiency is independent of the angle Δ (82:3422).

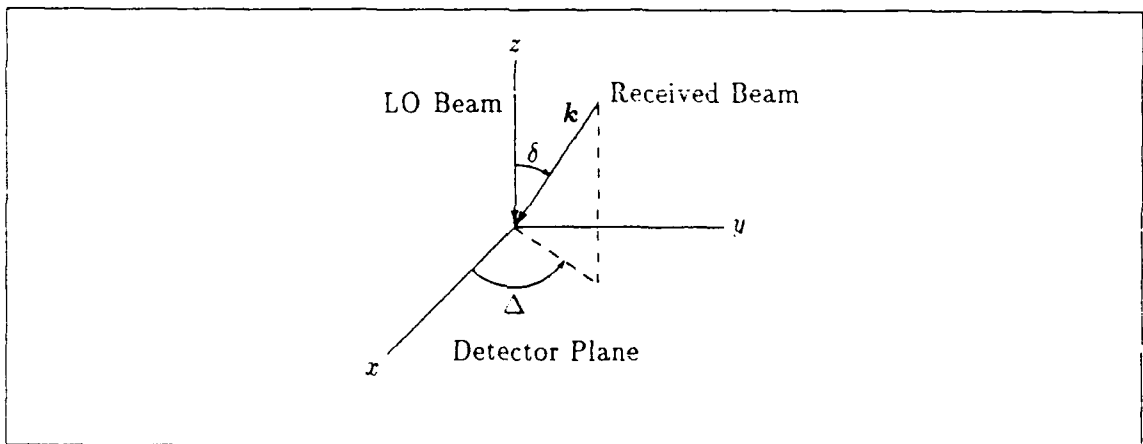


Figure 24. LO-Received Beam Misalignment Geometry (Reproduced from Wang (82:3422))

The misalignment factor may be included in Equation (53) for the field incident on the focal plane as follows:

$$E_r(\rho) = -\frac{jkEr_o e^{jk(s'+z)}}{s'} \int_b^a e^{j\mathbf{k} \cdot \boldsymbol{\rho}} J_0(k\rho \sin\theta) \rho d\rho \quad (74)$$

where $e^{j\mathbf{k} \cdot \boldsymbol{\rho}}$ represents the misalignment between the two beams, and ρ is the radial coordinate in the receiver aperture. The mixing process, and hence, misalignment,

can be considered to occur in the receiver aperture due to the antenna theorem for heterodyne reception (69:3293).

Using Equation (67), the mean square IF power is now

$$\begin{aligned} \langle P_{if} \rangle^2 &= \langle P_r \rangle \frac{c \epsilon_o k^2}{\pi F_s^2 (1 - \gamma^2)} \left| \int_0^L \int_0^L E_l(x_d, y_d) \right. \\ &\quad \times \left. \left\{ \int_{\gamma}^1 e^{-j a k \rho \sin \delta} J_0 \left[\frac{k \rho (x_d^2 + y_d^2)^{1/2}}{2 F_s} \right] \rho d\rho \right\} dx_d dy_d \right|^2 \end{aligned} \quad (75)$$

For a generalized distribution, the equation for heterodyne efficiency can then be written as

$$\eta_H = \frac{4 \left| \int_0^L \int_0^L E_l(x_d, y_d) \left\{ \int_{\gamma}^1 e^{-j \beta \rho} J_0 \left[\frac{k \rho (x_d^2 + y_d^2)^{1/2}}{2 F_s} \right] \rho d\rho \right\} dx_d dy_d \right|^2}{\pi F_s^2 (1 - \gamma^2) \left| \int_0^L \int_0^L E_l(x_d, y_d) dx_d dy_d \right|^2} \quad (76)$$

where $\beta = k a \sin \delta$.

Using a uniform LO distribution, and expanding the exponential misalignment term with Euler's Formula, Equation (76) yields

$$\begin{aligned} \eta_H &= \frac{4}{\pi \sigma^2 r^2 (1 - \gamma^2)} \left\{ \left| \int_0^L \int_0^L dx_d dy_d \int_{\gamma}^1 \cos(\beta \rho) J_0 \left[\rho (x_d^2 + y_d^2)^{1/2} \right] \rho d\rho \right|^2 \right. \\ &\quad \left. + \left| \int_0^L \int_0^L dx_d dy_d \int_{\gamma}^1 \sin(\beta \rho) J_0 \left[\rho (x_d^2 + y_d^2)^{1/2} \right] \rho d\rho \right|^2 \right\} \end{aligned} \quad (77)$$

Equation (77) can be evaluated for various obscurations using numerical techniques, provided values of r and σ are specified. The optimum value of $r = 0.635$ can be taken from Equation (73) (plotted in Figure 23) for a uniform LO distribution and no misalignment. The σ value is set from the specified obscuration using Equation (58) (plotted in Figure 20). Using these values of r and σ , Equation (77) is

plotted in Figure 25 against the misalignment parameter, β , for various obscurations. A general decrease in heterodyne efficiency is observed as misalignment increases. Interestingly, higher obscuration ratios are not as sensitive to misalignment, possibly due to additional diffraction effects from the secondary element. The transmitter efficiency factor, η_t , can now be easily obtained from Equations (73) and (77) by using the following relation:

$$\eta_t = (1 - \gamma^2)\eta_H \quad (78)$$

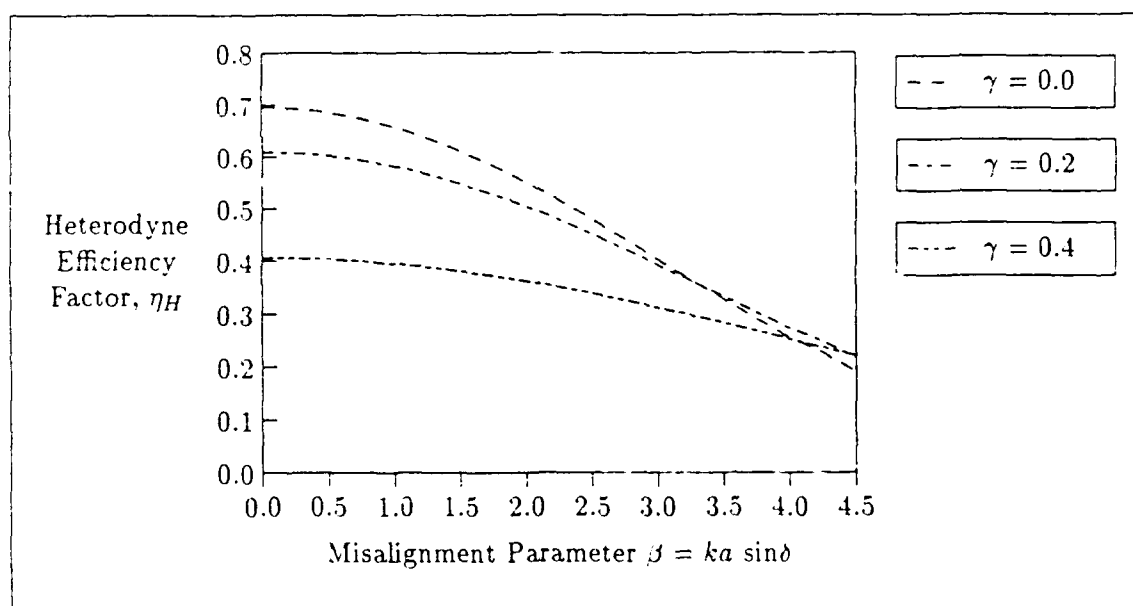


Figure 25. Heterodyne Efficiency versus Misalignment Parameter, $\beta = ka \sin \delta$

Having finally developed the expressions for transmitter and receiver gain in terms of efficiency factors, all LADAR Equation variables are now defined in terms of system design parameters. However, the calculated value of received power, $\langle P_r \rangle$, cannot then be used with Equation (25) to find SNR , since not all received power is actually detected. This loss of power is due to finite detector size and the FPA detection process.

FPA Detection Analysis

As already described, the detected signal is compared to a decision threshold which is set, in turn, by combining a noise measurement with a desired p_{fa} . For FPA detection, this process is repeated for every pixel in the array. If the received image falls over many FPA elements, signal power from several pixels could conceivably cross the threshold. Of the pixels which *have* crossed the threshold, the element with the largest signal is discriminated so that the target location is confined to one pixel field-of-view.

This method contributes to the high angular resolution of FPAs, but is only practical if the maximum signal fraction falling on any single pixel is sufficient to reliably cross the threshold. Calculation of the maximum signal fraction for each likely detection event is required to determine an expected value of $\langle P_r \rangle$ for FPA detection. Therefore, determination of the expected image location, and resultant maximum signal fractions is required before the expected mean received power, $E\{\langle P_r \rangle\}$, can be derived.

To simplify the analysis of image detection on an FPA, the received Airy pattern can be approximated by a disk of uniform irradiance. The radius of the approximating disk can be set by considering the distribution of Airy image power. From Equation (56), the expression for Airy power normalized to peak power may be written as

$$\frac{|E(\rho_A)|^2}{|E(0)|^2} = \left[\frac{J_1(\sigma\rho_A/R_A) - \frac{J_1(\gamma\sigma\rho_A/R_A)}{\gamma}}{\sigma(\rho_A/R_A)} \right]^2 \quad (79)$$

where ρ_A is the Airy image radial coordinate at the detector.

Figure 26 shows normalized Airy disk power plotted against normalized image radius, ρ_A/R_A , for various obscurations. The point at which the power falls to $1/e$ of the peak value is a common definition for the 'edge' of a beam or image (59:14). This $1/e$ radius, denoted by ω_A , can be seen from Figure 26 to correspond to an image radius of approximately 50% to 53% of the Airy radius, depending on obscuration.

Therefore, the ω_A disk approximation represents a smaller amount of received power than R_A since the Airy disk tail is trimmed off.

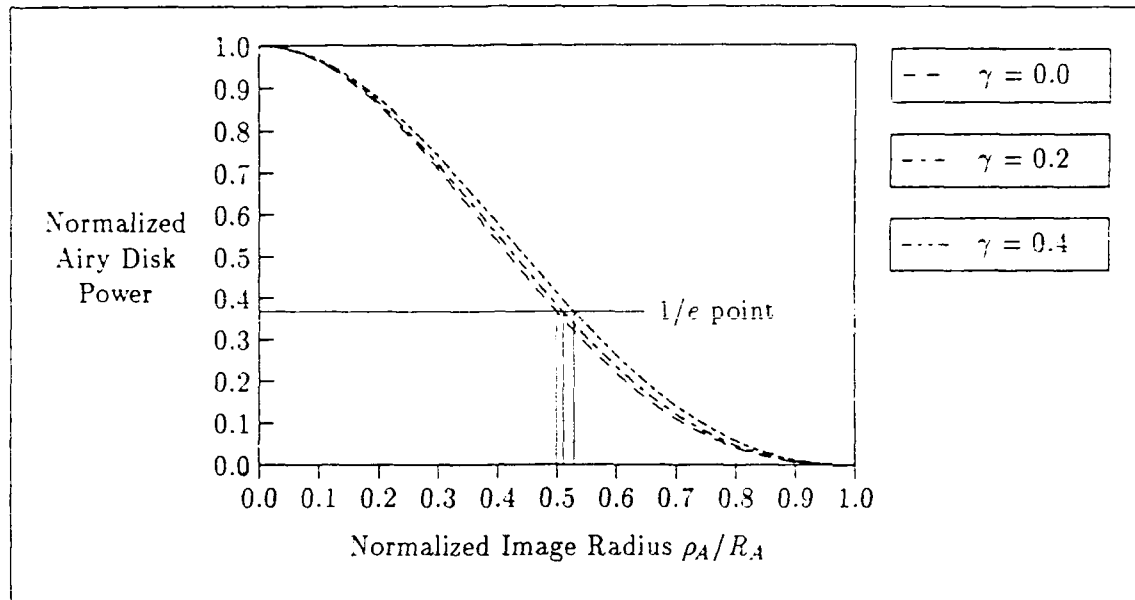


Figure 26. Normalized Airy Disk Power versus Normalized Image Radius

The actual fraction of signal power contained within a radius of ω_A can be determined through consideration of the integrated Airy pattern power as a function of image radius. Figure 27 shows the normalized Airy power, integrated from the central peak (lower integration limit) outwards, and plotted as a function of outer radius, ρ_A (upper integration limit). The Airy disk radii are marked for each obscuration, and represent approximately 84%, 73%, and 49% of the total image power for obscurations of 0, 0.2, and 0.4, respectively. Conversely, Figure 27 also shows that the ω_A radii represent only 58.4%, 51.5%, and 35.2% of the power, respectively.

An additional FPA characteristic which can cause a high false-alarm rate or poor detection capability is detector responsivity, as described in Chapter III. Assuming that each pixel has been individually calibrated to achieve uniform responsivity, and that no 'dead' pixels exist, the fraction of power encircled by ω_A will now be used to determine the expected maximum signal power for FPA signal detection. Recall-

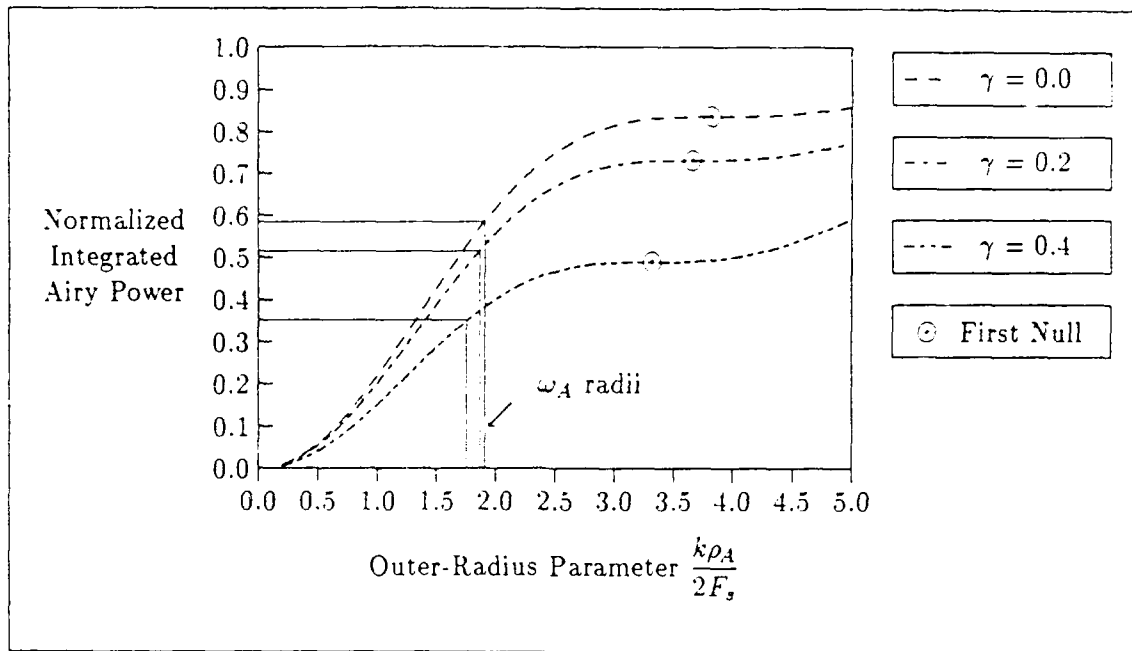


Figure 27. Normalized Integrated Airy Power as a Function of Outer Image Radius

ing the optimum detector-to-Airy size ratio for a uniform LO of $r = L/R_A = 0.635$, an optimum ratio of ω_A to L can be determined as follows:

$$\begin{aligned} \frac{\omega_A}{L} &= \frac{\omega_A}{R_A} \cdot \frac{R_A}{L} = \frac{\omega_A}{R_A} \cdot \frac{1}{0.635} \\ &= \left\{ \begin{array}{ll} 0.787 & \text{for } \gamma = 0 \\ 0.804 & \text{for } \gamma = 0.2 \\ 0.834 & \text{for } \gamma = 0.4 \end{array} \right\} \quad (80) \end{aligned}$$

The assumption that the Airy disk can be characterized by a circular disk of uniform irradiance with radius ω_A allows the ratio ω_A/L to be fixed for each obscuration. FPA detection analysis may now proceed by considering a two-dimensional FPA with pixel dimensions $2L \times 2L$ and a gap between pixels of width g . Figure 28 depicts possible image locations on a section of FPA, where the ratio ω_A/L has

been fixed for an obscuration ratio of 0.2, and the gap width has been set at $0.6L$. Clearly, the image can overlap a maximum of four pixels. Therefore, assuming that the image falls randomly on the FPA, the expected maximum received signal is given by (53:5)

$$E\{S_R\} = \sum_{n=1}^4 S_n p_n \quad (81)$$

where S_n is the maximum power possible from a single pixel within a group of n pixels which contain all of the image disk, p_n is the probability that all power is contained within n pixels, and $E\{S_R\}$ is the expected value of the maximum received signal.

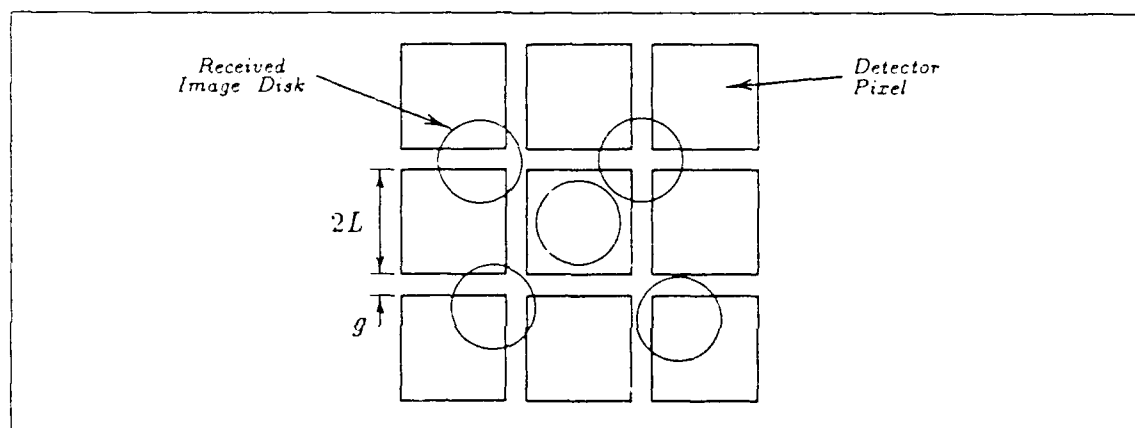


Figure 28. Possible Image Locations on an FPA for $\gamma = 0.2$ and $L/g = 1.67$

The total power contained in the disk and Airy image, which both vary with obscuration ratio, will be denoted by $P_{disk}(\gamma)$ and $P_{im}(\gamma)$, respectively. The value of S_n when all of $P_{disk}(\gamma)$ is received by n pixels can then be calculated geometrically, by considering the maximum fraction of an image disk overlapping a pixel. This maximum fraction depends on the disk location, which can be uniquely specified in terms of the location of the disk center, since ω_A/L is fixed. Figure 29 gives the distribution and geometry of image centers in terms of array and image dimensions, and is valid for $g \leq \omega_A$.

The *expected* location of the image center is the centroid of each area of image centers. Therefore, for $n = 1$, the expected image center is the center of the pixel,

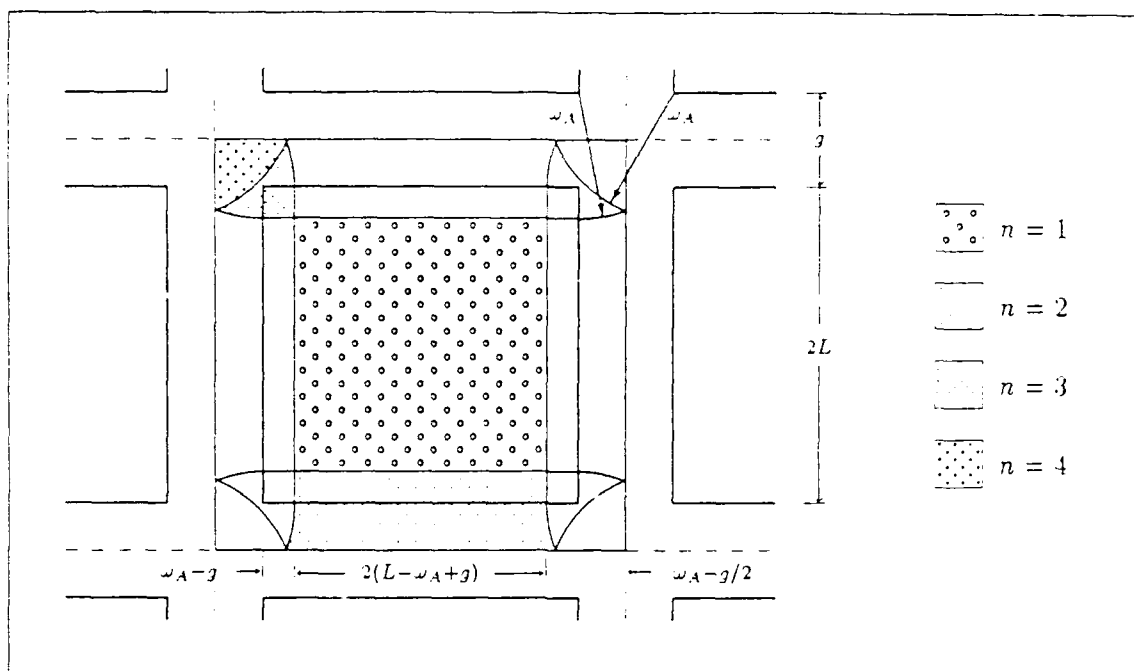


Figure 29. Distribution of Image Center Locations for n overlapped pixels

and $S_1 = P_{disk}(\gamma)$ for all values of $g \leq \omega_A$. The expressions for S_2 , S_3 , and S_4 are considerably more complicated and are developed in Appendix A. Figure 30 displays the expressions graphically as $S_n/P_{disk}(\gamma)$ plotted against the detector dimension parameter, L/g , for an obscuration ratio of 0.2. Graphs for other obscurations appear in Appendix A, and show similar general trends. Since the expressions are only valid for $g \leq \omega_A$, the graphs are only valid for the range $L/g \geq 1.2$ to 1.3, depending on γ . Figure 30 shows that the maximum signal fraction increases as L/g increases, as expected, and that less signal is detected as the image overlays more pixels.

The corresponding p_n values can also be obtained geometrically by dividing the area of all possible image center locations shown in Figure 29 by the total area of a detector element. In this case, the area of a detector element consists of the pixel area plus half of the adjoining gap area, because each pixel can be considered to 'own' half of the surrounding gap. From Figure 29, p_1 is therefore

$$p_1 = \frac{[2(L - \omega_A + g)]^2}{(2L + g)^2} \quad (82)$$

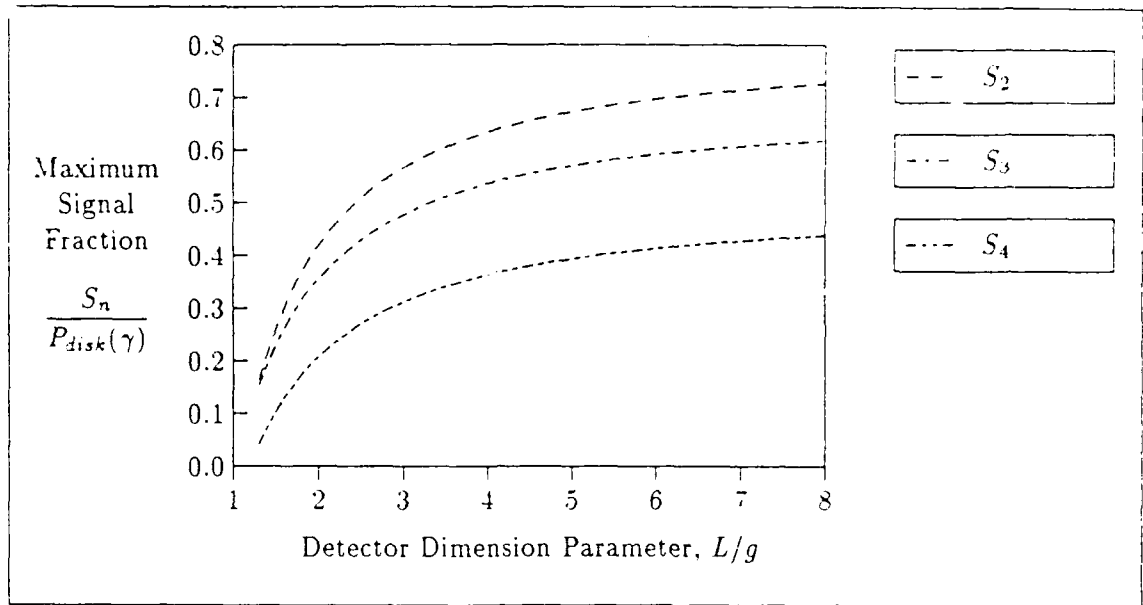


Figure 30. Maximum Signal Fraction when Image Overlays n Pixels and $\gamma = 0.2$

The remaining p_n expressions are also developed in Appendix A, accompanied by graphs corresponding to $\gamma = 0$ and $\gamma = 0.4$. Figure 31 is plotted for an obscuration ratio of 0.2. The major variation with L/g involves p_1 and p_4 . As L/g increases, corresponding to a smaller gap, the probability of the disk falling on only one pixel decreases sharply, since the disk is more likely to overlap adjacent elements. Since a shrinking gap also sharply reduces the dead area situated at the 'crossroads' of four pixels (proportionally with g^2), p_4 increases much faster than p_3 , and at the expense of p_2 .

From Equation (81), both S_n and p_n are needed to determine the expected maximum received signal, $E\{S_R\}$. Expressing $E\{S_R\}$ as a fraction of $P_{im}(\gamma)$, Figure 32 shows $E\{S_R\}$ as a function of L/g , for various obscurations.

The resultant overall trend for signal fraction to increase as L/g increases is as expected. The 'dip' in the curves at values of $L/g < 2$ can be explained by the effect of a sharply decreasing p_1 combined with a signal fraction, $\frac{S_1}{P_{disk}(\gamma)} = 1$. Since the higher order signal fractions are much lower in this region, the overall signal 'dips' before rising again as lower order signal fractions become significant.

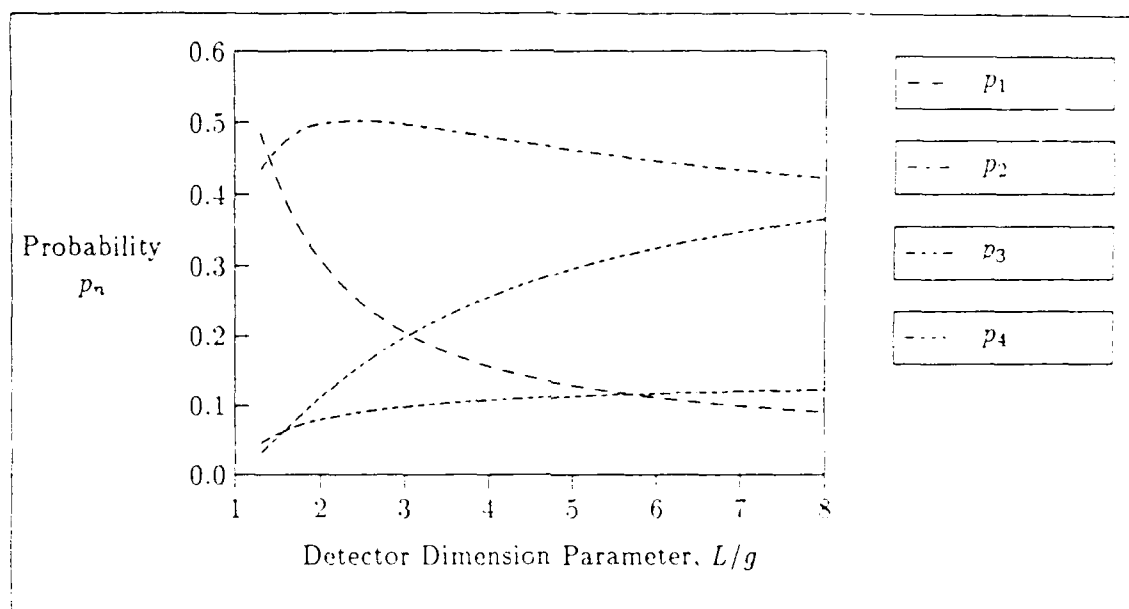


Figure 31. Probability of Image Overlaying n Pixels with $\gamma = 0.2$

As obscuration increases, the lower expected signal can be attributed to a smaller Airy disk containing less power. As an example, choosing an arbitrary L/g value of 2 and an obscuration ratio of 0.2, the expected maximum fraction of $P_{im}(\gamma)$ received is about 29.4%. This fraction of $\langle P_r \rangle$ can then be used to calculate SNR , and hence, p_d and p_{fa} .

The preceding analysis has developed the theory necessary to determine the major LADAR design parameters, including transmitter gain, receiver gain, expected received power, SNR , p_d , and p_{fa} . These equations will provide an estimate of whether detection is possible, and with what likelihood. Other degrading effects such as mild turbulence, atmospheric scintillation, target depolarization, target scintillation, weather, variations in manufacturers' specifications, component deterioration, optics misalignment, and signal processing losses are difficult to quantify, with some factors exhibiting wide variation between detection events. Common design practice leads to the addition of a SNR system margin to account for such factors.

Several other limitations exist which can cause complete loss of signal under certain conditions. They include strong atmospheric turbulence, telescope pointing

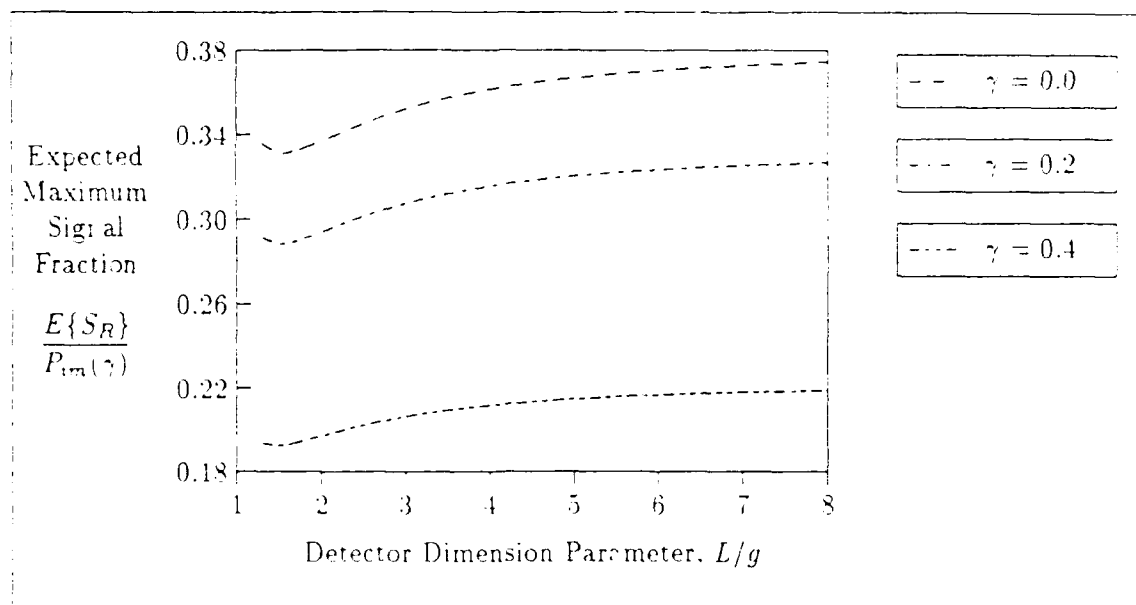


Figure 32. Expected Maximum Signal Fraction for FPA detection

accuracy, telescope mount stability, and high power beam effects such as thermal blooming. These factors have been discussed in Chapters III and IV, and must be included in any comprehensive LADAR design analysis; however, many of the deleterious effects can be minimized considerably by careful selection of LADAR site, wavelength, and specification of high-performance hardware.

LADAR Accuracy

Although reliable signal detection is the primary LADAR design goal, simply knowing that a target is 'out there' is insufficient information for surveillance purposes. The target's position must be identified accurately by determining its spatial coordinates and velocity so that an orbital element set can be calculated. The accuracy with which this can be performed is characterized by the detector element size and the transmitted waveform.

Since a target can be positioned only to within one detector element on the FPA, the angular field-of-view of the pixel *plus half of the surrounding gap* determines the system's *angular accuracy*. Conversely, the transmitter pulse width can

be thought of as a travelling wave of length $c\tau$, where c is the speed of light, and τ is the pulse width. Neglecting the effects of pulse dispersion, a target of large spatial extent can generate signal reflections from anywhere within the distance $c\tau$ and can therefore only be positioned with a *range accuracy* of $c\tau/2$.

Additionally, the measurement accuracy of the target's radial velocity is determined by the magnitude of the Doppler shift and the performance of the post-detection circuitry. For a target with radial velocity component v_r , the Doppler shift is given by $2v_r/\lambda$. The measurement of lateral velocity, or angular rate, is performed by successive detections — assuming no target maneuvering — with a measurement accuracy determined by the time between independent detections, and the post-detection circuit performance.

LADAR Resolution

An additional detection problem arises when two or more targets are located closely together in angle, range and velocity. The LADAR's ability to discriminate between targets is described by the LADAR's *angular resolution*, *range resolution*, and *velocity resolution*.

LADAR resolution may be specified in terms of design parameters and is normally fixed as a result of trade-off between waveform and circuit complexity, and the parameters which affect *SNR*, such as optics diameter, obscuration ratio, wavelength, and pulse width. As for system accuracy calculations, the parametric equations for resolution will be presented for the case of a simple pulse-modulated sinusoid of constant frequency.

Using the same argument as for range accuracy, range resolution is limited to $c\tau/2$. For a transmitter pulse width of $1\ \mu\text{s}$, two targets can be resolved in range as close as 150 m apart. The velocity resolution for a heterodyne system is given by Bachman as approximately $\lambda/2T$, where T is the duration of the entire transmitted waveform (6:31).

Angular Resolution Angular resolution is commonly specified using the *Rayleigh* definition, which states that two point images are resolved if the center of the diffraction pattern generated by the first image falls at the first null of the second image's pattern (68:188). Without considering other limitations, this definition sets the lower resolution limit, and systems operating at this limit are said to be *diffraction-limited*. Adopting the Rayleigh definition, the angular resolution for a diffraction-limited system, Θ_{diff} , may be written as

$$\Theta_{\text{diff}} = \frac{R_A}{f_{\text{eff}}} = \frac{\sigma}{ka} \quad (83)$$

For example, an obscuration ratio of 0.2, wavelength of 5 μm , and receiver aperture primary radius of 30 cm yields an angular resolution of approximately 9.7 microradians. This system would theoretically be able to discriminate between two targets as close as 350 m apart at geosynchronous orbit.

Two other limitations to angular resolution which may dominate for systems not diffraction-limited are atmospheric turbulence and detector size. The scintillation effects of turbulence can be estimated from the transverse phase coherence length described in Chapter IV. For example, a wavelength of 10 μm and coherence length, r_0 , of 3.6 m yields a resolution of 2.4 microradians, while for $\lambda = 0.5 \mu\text{m}$, and $r_0 = .1 \text{ m}$, the resolution limit is 4.8 microradians (87:6-29).

The effect of detector size is more severe, since each Airy pattern must not only be imaged on separate pixels for successful detection, but must also be resolved in a separate range and/or Doppler cell to differentiate between a single Airy pattern overlapping two pixels, and two separate patterns on adjacent pixels. Assuming both conditions are successfully discriminated, then the system resolution can be defined in terms of the detector instantaneous field-of-view (IFOV). If the IFOV of a square detector element is defined as the IFOV of a pixel *plus half of the surrounding gap*, then the resolution limit for a detector-limited system, Θ_{det} , is identical to the

system's angular accuracy, and is given by

$$\Theta_{\text{det}} = \frac{2L + g}{f_{\text{eff}}} \quad (84)$$

For example, a pixel size of $50\mu\text{m} \times 50\mu\text{m}$ and a gap of $12.5\mu\text{m}$, combined with a 3 m focal length, yields a resolution limit and angular accuracy of only 20.8 microradians.

Clearly, minor variations in detector or telescope parameters may cause the angular resolution to be limited by either diffraction or detector factors, with turbulence becoming dominant only under extremely strong turbulence conditions.

Summary

Parametric analysis of the LADAR detection problem has produced a set of equations which can be used as the basis for a first-level theoretical design of a candidate ground-based deep-space LADAR. The effects of beam truncation and diffraction, heterodyne misalignment, off-boresight detection, optics transmittance, and atmospheric transmittance are included in the analysis. However, the effects of atmospheric turbulence and scintillation, target scintillation, telescope mount stability, and high power beam effects are not included.

A summary of the parametric relationships is now outlined for the case of M transmitted pulses, obscured circular transmitter and receiver apertures, heterodyne receiver configuration, FPA detection, and uniform LO distribution over the FPA surface. The FPA consists of a two-dimensional array of square pixels, with gaps between each pixel.

For a specified *mean time between false alarms*, t_{fa} , the probability of false alarm, p_{fa} , is

$$p_{fa} = \frac{Mt_g}{t_{fa}(1 - \delta_{\text{off}})} \quad (85)$$

where M , t_g , and δ_{off} are chosen by the designer and are constrained by transmitter performance and receiver complexity. With M , p_{fa} , and p_d set, Figure 16 is then used to find the minimum required $S.N.R$ to meet detection specifications. An arbitrary system margin is then added to $S.N.R$ to cover miscellaneous system losses.

Minimum average received power is then calculated to meet $S.N.R$ requirements using

$$\langle P_r \rangle = \frac{S.N.R \ h \ c \ B}{\lambda \ \eta_d} \quad (86)$$

where the wavelength and bandwidth are fixed from the selection of laser and detector/IF hardware.

With minimum required $\langle P_r \rangle$ determined, the LADAR Equation is then used in an iterative process to determine the optimum combination of transmitter, telescope, and detector characteristics which will meet performance specifications, with consideration given to complexity, cost, and technology availability. The final form of the LADAR Equation is

$$\langle P_r \rangle = \frac{E\{S_R\}}{P_{im}(\gamma)} \cdot \frac{P_t A_t A_r \tau_{lo} \tau_{ro} \tau_A^2 \sigma_{lcs} (1 - \gamma^2) \eta_t \eta_H}{4\pi \lambda^2 R^4} \quad (87)$$

where the value of $\frac{E\{S_R\}}{P_{im}(\gamma)}$ is determined from Figure 32, based on detector dimensions and telescope obscuration. The value of η_t used in the LADAR Equation is determined using

$$\eta_t = 2\alpha^2 \left| \int_{\gamma^2}^1 e^{-\alpha^2 u} J_0(Xu^{1/2}) du \right|^2 \quad (88)$$

which is plotted in Figure 18. The value of η_H used in the LADAR Equation is

calculated for a uniform LO distribution *with no misalignment* from

$$\eta_H = \frac{4 \left| \int_0^{\sigma r} \int_0^{\sigma r} \frac{J_1[(x_1^2 + y_1^2)^{1/2}] - \gamma J_1[\gamma(x_1^2 + y_1^2)^{1/2}]}{(x_1^2 + y_1^2)^{1/2}} dx_1 dy_1 \right|^2}{\pi(1 - \gamma^2)\sigma^2 r^2} \quad (89)$$

which is plotted in Figure 23. Misalignment effects can be included in the heterodyne efficiency term, and are determined using

$$\eta_H = \frac{4}{\pi\sigma^2 r^2(1 - \gamma^2)} \left\{ \left| \int_0^L \int_0^L dx_d dy_d \int_{\gamma}^1 \cos(\beta\rho) J_0[\rho(x_d^2 + y_d^2)^{1/2}] \rho d\rho \right|^2 + \left| \int_0^L \int_0^L dx_d dy_d \int_{\gamma}^1 \sin(\beta\rho) J_0[\rho(x_d^2 + y_d^2)^{1/2}] \rho d\rho \right|^2 \right\} \quad (90)$$

which is plotted in Figure 25 using the optimum L/R_A ratio of 0.635.

Based on a specified detection probability, the preceding equation set allows theoretical analysis of detailed LADAR design feasibility, subject to the assumptions already outlined. LADAR performance in terms of accuracy and resolution is then calculated using the following equations:

$$\left. \begin{aligned} \text{Range Accuracy} &= \frac{c\tau}{2} \\ \text{Doppler Shift} &= \frac{2v_r}{\lambda} \\ \text{Range Resolution} &= \frac{c\tau}{2} \\ \text{Velocity Resolution} &= \frac{\lambda}{2T} \\ \text{Angular Resolution} &= \frac{R_A}{f_{eff}} = \frac{\sigma}{ka} \quad ; \text{ diffraction-limited} \\ &= \frac{2L + g}{f_{eff}} \quad ; \text{ detector-limited} \end{aligned} \right\} \quad (91)$$

The parametric analysis summarized by this set of design equations has examined the losses associated with the transmitting and receiving telescopes, and detection efficiency for a wide range of detector arrangements, LO configurations, and beam misalignment conditions. These equations allow calculation of the primary LADAR performance parameters in terms of the LADAR hardware specifications, and include optimization factors for detector dimensions, LO beam size, and telescope dimensions.

VI. Candidate Design

Introduction

This chapter applies the LADAR theory presented in Chapter V to the problem of deep-space satellite detection. LADAR component specifications are based on current technology as outlined in Chapter III, using the two candidate laser wavelengths drawn from Chapter IV. Calculation results are presented for two LADAR sites, using both wavelengths, with detection under ideal and worst-case conditions. Calculations are performed for two transmitter waveforms: an unmodulated pulse train, and a linear-FM chirp pulse train. Two alternative design concepts are then discussed which are aimed at greatly increasing the amount of received power.

Design Calculations

The fundamental question in this analysis is whether deep space objects can be detected by a ground-based LADAR and, if so, under what conditions. Design feasibility depends not only on successful detection of deep-space objects, but on reliable detection of most likely targets over a wide range of viewing geometries and 'seeing' conditions. If overall LADAR performance cannot be demonstrated to be significantly better than existing systems such as GEODSS, then further development is not justified. 'Significantly better', in this case, means that substantial improvements in weather-tolerance and daylight operation must be achieved while maintaining a detection capability comparable to GEODSS.

The diversity in conditions at the various GEODSS sites is an indication of the range of weather and atmospheric conditions likely to affect LADAR operation. For each GEODSS location, two extreme detection cases are considered for design feasibility calculations. The 'best' detection case is defined as LADAR detection of a geosynchronous target at a 36,000 km range which is positioned on the telescope

boresight and located at the sensor zenith. Other best-case conditions include clear skies and perfect heterodyne alignment.

Similarly, the 'worst' case is defined as detection of a geosynchronous target located off-boresight at a look angle of 60° and range of 40,000 km. Since a typical beamwidth for a long-range LADAR is about $10 \mu\text{rad}$ (77:153), the worst-case off-boresight angle is set at $5 \mu\text{rad}$ to coincide with the beam 'edge'. For the receive path, the corresponding worst-case heterodyne misalignment is also set at $5 \mu\text{rad}$. Operation through rain is not considered due to the associated severe attenuation; however, cirrus-cloud attenuation is included in the worst-case scenario.

Since atmospheric attenuation varies between GEODSS sites, Socorro and Diego Garcia are used as two examples of typical seeing conditions. Therefore, design calculations are required for four combinations of detection conditions at each of the two candidate wavelengths selected in Chapter IV.

The general methodology used in design calculations is shown in Table 6 as a sequence of design steps aimed at determining two values for comparison: (1) the required minimum received power for successful target detection, and (2) the calculated received power from the candidate design. The overall methodology is based on the procedure summarized in Chapter V, which is constrained by target characteristics, atmospheric effects, and available technology as summarized in previous chapters. In particular, the maximum size of telescope apertures is limited by both turbulence effects and available technology. Also, transmitter power is limited by both available technology and atmospheric effects, and is restricted to operation at $11.17 \mu\text{m}$ or $4.64 \mu\text{m}$.

In addition to hardware constraints, input specifications are required for p_d and p_{fa} . Equation (85) in Chapter V may be used to calculate a value of p_{fa} from a desired t_{fa} after selecting a transmitter waveform and receiver range-gate characteristics.

Table 6. Candidate LADAR Design Sequence

<i>Design Step</i>	<i>Relationship</i>	<i>Parameters</i>
<u>Performance Requirements</u>		
1. Set p_d and t_{fa}		p_d, t_{fa}
2. Choose Transmitter		λ, P_t , rep. rate
3. Choose Waveform		$M, \tau, t_g, \delta_{off}$
4. Calculate p_{fa}	Eq (85)	p_{fa}
5. Determine SNR	Figure 16 or (73:2-22)	
6. Set System Margin		
7. Calculate Minimum SNR	SNR+margin	
8. Define Target Characteristics		$v_r, \sigma_{lcs}, R,$ ψ_s, θ, δ
9. Calculate Bandwidth	Doppler+chirp+linewidth	B
10. Choose Detector		$\eta_q, L, L/g$
11. Calculate Minimum Power	Eq (86)	Required P_r
<u>LADAR Equation Calculations</u>		
12. Determine Maximum Signal Fraction	Figure 32	$\frac{E\{S_R\}}{P_{im}(\gamma)}$
13. Estimate Coherence Lengths	Figure 13	τ_{ot}, τ_{or}
14. Choose Optics		$A_t, A_r, \tau_{to},$ $\tau_{ro}, \gamma, f_{eff}$
15. Optimize L/R_A for max η_H (repeat from Steps 10/14 if needed)	Figure 23	L/R_A
16. Define Weather along Signal Path	Figures 10, 11, 12	τ_A
17. Calculate Transmitter Efficiency	Figure 18	η_t
18. Calculate Heterodyne Efficiency	Figure 25	η_H
19. Calculate Design Power	Eq (87)	Design P_r
20. Check for Power Ratio > 1 (repeat from Step 1 if needed)	Design/Required P_r	
21. Calculate Accuracy and Resolution	Eq (91)	

Unmodulated Pulse Train

For the first candidate design, a transmitter waveform consisting of M rectangular pulses of constant frequency is considered. Choosing a transmitter pulse repetition rate of 300 pulses per second, pulse width of $1\ \mu\text{s}$, and range-gate on-time, t_g , of $20\ \mu\text{s}$ implies a receiver dead-time fraction, δ_{off} , of 0.994. For a transmitted pulse train of $M = 110$ pulses, and a time between false-alarms of one hour, Equation (85) yields a p_{fa} value of 10^{-4} . These specifications are combined with an arbitrary p_d value of 0.95 to obtain an SNR value from Figure 16 in Chapter V of $-3\ \text{dB}$.

An arbitrary system margin of 3 dB is then added to compensate for scintillation and miscellaneous losses. The resultant minimum SNR value of 0 dB is used in Equation (85) to calculate the minimum required received power. Other input parameters required are IF bandwidth and detector quantum efficiency. Since geosynchronous targets will have only small radial components of velocity, bandwidth will be limited to 100 MHz to cover expected Doppler shifts. Based on available technology, η_q is set to 0.85. Table 7 summarizes the design specifications assumed for all detection cases. Depending on which wavelength is used, the minimum required received power can then be calculated. This value must be met or exceeded by the value of expected received power calculated by the LADAR Equation in Chapter V.

The first input parameter for the LADAR Equation is the expected maximum signal fraction received using FPA detection, $\frac{E(S_R)}{P_{\text{im}}(\gamma)}$. For an obscuration ratio of 0.2 and detector dimension ratio of 4, a signal fraction of 0.32 is obtained from Figure 32 in Chapter V. Secondly, the transmitter power must be defined. Considering the pulse repetition rate and pulse width selected, a laser transmitter capable of 5 MW output is probably the limit of current or near-future technology.

Telescope characteristics must now be specified by trading off beam divergence and aperture area with loss of phase-coherence and available technology. Figure 13 in Chapter IV provides rough estimates for maximum aperture sizes based on turbu-

Table 7. Candidate Design Specifications for all Detection Cases Using an Unmodulated Transmitter Pulse Train

<i>Parameter</i>	<i>Value</i>	<i>Parameter</i>	<i>Value</i>
Target Cross-Section, σ_{tcs}	4 m ²	Pulse Repetition Rate	300 pps
Probability of Detection, p_d	0.95	Number of Pulses, M	110
Probability of False-Alarm, p_{fa}	10 ⁻⁴	Range-Gate On-Time, t_g	20 μ s
Obscuration Ratio, γ	0.2	Receiver Dead-Time, δ_{off}	0.994
IF Bandwidth, B	100 MHz	Pulse Width, τ	1 μ s
Detector Dimension Ratio, L/g	4	Optics Transmittance	0.85
Received Signal Fraction, $\frac{E(S_R)}{P_{im}(\tau)}$	0.32	System Margin	3 dB
Detector Quantum Efficiency, η_q	0.85	Minimum SNR Required	0 dB

lence effects, but current technology and high manufacturing costs suggest a practical upper limit for aperture size of about 1.5 – 2 meters in diameter. Therefore, maximum transmitter aperture size is limited by turbulence, while maximum receiver aperture size is limited by technology. Apart from telescope elements, several other elements exist in the optical train which can attenuate the LADAR signal. A combined one-way transmittance factor of 0.85 for the optical system will account for these losses.

The atmospheric transmittance value used in the LADAR Equation is taken from Figures 10, 11, and 12 in Chapter IV, depending on LADAR site and cloud conditions. The remaining input parameters — transmitter efficiency and heterodyne efficiency — are derived from Figures 18 and 25 in Chapter V, which include off-boresight and misalignment effects. Tables 8 and 9 summarize the viewing conditions and remaining input parameters for calculation of the expected received power at wavelengths of 11.17 μ m and 4.64 μ m, respectively.

As can be seen from the tables, heterodyne and transmitter efficiencies are more sensitive at shorter wavelengths to off-boresight detection and misalignment. The transmitter power at 4.64 μ m is set to 40% of the ¹³CO₂ output, based on

Table 8. Received Power Calculations at 11.17 μm Using an Unmodulated Pulse Train

	Diego Garcia		Socorro	
	Best	Worst	Best	Worst
Sky Conditions	Clear	Cirrus	Clear	Cirrus
Look Angle, ψ ,	0°	60°	0°	60°
Target Range, R	36,000 km	40,000 km	36,000 km	40,000 km
Boresight Angle, θ	0 μrad	5 μrad	0 μrad	5 μrad
Atmospheric Transmittance, τ_A	0.58	0.25	0.98	0.71
Misalignment Angle, δ	0 μrad	5 μrad	0 μrad	5 μrad
Transmitter Aperture Diameter	1 m	1 m	1.4 m	1.4 m
Receiver Aperture Diameter	1.75 m	1.75 m	1.75 m	1.75 m
Transmitter Power, p_t	5 MW	5 MW	5 MW	5 MW
Transmitter Efficiency, η_t	0.71	0.45	0.71	0.38
Heterodyne Efficiency, η_H	0.61	0.5	0.61	0.47
Design Received Power, P_r (W)	5×10^{-16}	3×10^{-17}	3×10^{-15}	4×10^{-16}
Required Received Power (W)	2×10^{-12}	2×10^{-12}	2×10^{-12}	2×10^{-12}
Power Ratio: Design/Required	2.2×10^{-4}	1.4×10^{-5}	1.2×10^{-3}	9.8×10^{-4}

reported conversion efficiencies for frequency-doubling. The LADAR Equation was then used to calculate the expected received power from each design. The ratio of 'design' received power to 'required' received power must equal or exceed unity for the candidate design to meet the specified probability-of-detection and probability-of-false-alarm criteria.

Both tables show that reliable LADAR detection of geosynchronous targets using an unmodulated pulse train is theoretically infeasible, even for best-case detection conditions. Calculated values of received power at 11.17 μm are about four orders of magnitude smaller than the required minimum, and about five orders of magnitude below minimum at 4.64 μm . Since efficiency and transmittance factors for best-case

Table 9. Received Power Calculations at $4.64 \mu\text{m}$ Using an Unmodulated Pulse Train

	Diego Garcia		Socorro	
	Best	Worst	Best	Worst
Sky Conditions	Clear	Cirrus	Clear	Cirrus
Look Angle, ψ ,	0°	60°	0°	60°
Target Range, R	36.000 km	40.000 km	36.000 km	40.000 km
Boresight Angle, θ	$0 \mu\text{rad}$	$5 \mu\text{rad}$	$0 \mu\text{rad}$	$5 \mu\text{rad}$
Atmospheric Transmittance, τ_A	0.8	0.48	0.96	0.68
Misalignment Angle, δ	$0 \mu\text{rad}$	$5 \mu\text{rad}$	$0 \mu\text{rad}$	$5 \mu\text{rad}$
Transmitter Aperture Diameter	0.3 m	0.3 m	0.4 m	0.4 m
Receiver Aperture Diameter	1 m	1 m	1.2 m	1.2 m
Transmitter Power, p_t	2 MW	2 MW	2 MW	2 MW
Transmitter Efficiency, η_t	0.71	0.58	0.71	0.47
Heterodyne Efficiency, η_H	0.61	0.35	0.61	0.25
Design Received Power, P_r (W)	2×10^{-16}	3×10^{-17}	1×10^{-15}	1×10^{-16}
Required Received Power (W)	5×10^{-12}	5×10^{-12}	5×10^{-12}	5×10^{-12}
Power Ratio: Design/Required	4.8×10^{-5}	5.3×10^{-6}	2.1×10^{-4}	1.9×10^{-5}

conditions are close to the maximum possible, large variations in received power can only be achieved by altering transmitter power or aperture sizes. However, scaling transmitter power up by four orders of magnitude for LADAR applications cannot be done with current technology, and is impractical due to possible optics damage and air breakdown. Also, the aperture sizes used in design calculations are close to the maximum practical for acceptable coherence losses and manufacturing cost.

Some improvement may be gained by relaxing the probability-of-detection criterion; however, the huge increase in received power required would result in a value of p_d which is too low for practical sensor operation.

Alternative Designs

Examination of the LADAR Equation shows that three other major parameters affect received power: wavelength, range, and target cross-section. Extensive analysis has already shown that the two selected wavelengths are the optimum choices available for LADAR applications. Therefore, range and target cross-section are the only remaining design variables. By altering these variables, two methods of improving detection performance are possible: range reduction by using a space-based sensor, and enhancement of target cross-section by using a corner-cube reflector.

Space-Based LADAR. Free-space loss over the two-way signal path is expressed by the R^4 term in the LADAR Equation, and represents an *extremely* large power loss for the range to geosynchronous orbit. Reduction of range can only be accomplished through the use of a space-based LADAR sensor, which has added advantages such as removal of turbulence, aerosol, and weather effects on signal propagation.

For space-based detection under the same best-case detection conditions as in the ground-based case, a minimum-altitude sensor orbit can be determined which will provide the desired minimum received power. Setting both transmitter and receiver aperture diameters to a more conservative value of 1.4 m, a power ratio exceeding unity is achieved at both wavelengths with a range of 6,000 km. This corresponds to a sensor orbit of 30,000 km, which means that one sensor could be used for surveillance of the entire geosynchronous ring due to a shorter orbital period. Since both apertures are the same size, a single telescope could be used, with automatic detection carried out according to, say, a search/track schedule which is updated daily from a single ground-control station. Also, space-based LADAR transmitter candidates could include the $^{12}\text{CO}_2$ laser at $10.6\text{ }\mu\text{m}$ since transmittance is no longer a selection criterion. Further reductions in transmitter power, and relaxation of alignment and aperture-size requirements would be possible at higher sensor orbits.

Several major hurdles must be overcome before such a scheme can be implemented. Sophisticated search and track techniques would be required for autonomous operation of the sensor platform. A large-capacity power supply, efficient thermal control system, and stable platform are also required for sensor support. Probably the two most critical requirements for a space-based sensor platform of this type are pointing accuracy and platform stability. Some method of relating telescope look angle to an inertial or earth-centered reference frame is required, along with isolation of the telescope mount from equipment vibration and platform movement, so that pointing accuracies on the order of a few microradians are maintained. Further analysis of space-based sensor performance is beyond the scope of this study.

Target Enhancement. The majority of geosynchronous objects are unenhanced, with relatively small LADAR cross-sections. However, if a corner-cube reflector designed to reflect IR radiation is attached to the object and faces earthward, target cross-section can be increased by several orders of magnitude. Although military satellites would not normally be fitted with such devices for obvious reasons, the majority of geosynchronous objects consist of communications satellites and rocket stages of commercial origin. Therefore, it is conceivable that future commercial satellites could be fitted with reflectors to assist in their detection and tracking.

The LADAR cross-section of a corner-cube reflector is expressed by Skolnik as (73:37-55)

$$\sigma_{lcs} = \frac{4\pi d^4}{3\lambda^2} \quad (92)$$

where d is the length of an edge of the corner-cube reflector.

For a reflector of dimension $d = 5$ cm, the corresponding cross-sections are $2 \times 10^5 \text{ m}^2$ and $1 \times 10^6 \text{ m}^2$, for wavelengths of $11.17 \text{ } \mu\text{m}$ and $4.64 \text{ } \mu\text{m}$, respectively. Table 10 shows the resultant received power for all detection cases and both candidate wavelengths. The power ratio values show that target enhancement can easily provide the required received power in most detection cases by using a relatively

small reflector. Since reflector cross-section scales proportionally with d^4 , a small increase in reflector size allows successful detection for all cases and wavelengths. With larger reflectors, smaller transmitters and apertures can be used to improve cost efficiency.

Table 10. Received Power for Enhanced Target and an Unmodulated Pulse Train

	Diego Garcia		Socorro	
	Best	Worst	Best	Worst
<u>$\lambda = 11.17\mu\text{m}$</u>				
Target Cross-Section, σ_{TC} (m^2)	2.10×10^5	2.10×10^5	2.10×10^5	2.10×10^5
Design Received Power, P_r (W)	2×10^{-11}	2×10^{-12}	1×10^{-10}	2×10^{-11}
Required Received Power (W)	2×10^{-12}	2×10^{-12}	2×10^{-12}	2×10^{-12}
Power Ratio: Design/Required	11.62	0.74	65.05	9.50
<u>$\lambda = 4.64\mu\text{m}$</u>				
Target Cross-Section, σ_{TC} (m^2)	1.22×10^6	1.22×10^6	1.22×10^6	1.22×10^6
Design Received Power, P_r (W)	7×10^{-11}	8×10^{-12}	3×10^{-10}	3×10^{-11}
Required Received Power (W)	5×10^{-12}	5×10^{-12}	5×10^{-12}	5×10^{-12}
Power Ratio: Design/Required	14.51	1.61	63.98	5.71

FM-Chirp Pulse Train

As discussed in Chapter III, pulse compression using an FM-chirp pulse train provides high range-resolution due to an effective reduction in the pulse width by τB_{FM} , the compression ratio. Another useful characteristic of pulse compression is that peak power of the compressed pulse is also increased by τB_{FM} . The level of power amplification/pulse compression is limited by the practical bandwidth of the FM chirp and the transmitter pulse width.

Due to the narrow linewidth of CO_2 laser transitions, FM bandwidths of up to 600 MHz appear to be practical (6:92). Pulse widths, on the other hand, depend on

laser excitation and cavity design (66:63). Moody et al. report a $^{13}\text{CO}_2$ amplifier with $\tau = 30 \mu\text{s}$, pulse power of 7 MW, and pulse repetition rate of 10 Hz (57:102). Based on this level of technology, $^{13}\text{CO}_2$ amplifier characteristics with $\tau = 50 \mu\text{s}$, pulse power of 6 MW, and pulse repetition rate of 100 Hz appear feasible now or in the near-future.

Using these specifications, design calculations were repeated for the two sites under ideal and worst-case conditions. Table 11 shows the results of these calculations for $B_{FM} = 600 \text{ MHz}$ and $\tau = 50 \mu\text{s}$. IF bandwidth was set at 650 MHz to allow for expected Doppler shifts in the reflected signal, and transmitter power at $4.64 \mu\text{m}$ was again reduced to 2 MW due to conversion efficiency. Aperture sizes and all other specifications are identical to those listed in Tables 8 and 9.

Table 11. Received Power Calculations Using a Linear-FM Chirp Pulse Train

	Diego Garcia		Socorro	
	Best	Worst	Best	Worst
<u>$\lambda = 11.17 \mu\text{m}$</u>				
Transmitter Power, p_t	6 MW	6 MW	6 MW	6 MW
Design Received Power, P_r (W)	2×10^{-11}	1×10^{-12}	9×10^{-11}	1×10^{-11}
Required Received Power (W)	1×10^{-11}	1×10^{-11}	1×10^{-11}	1×10^{-11}
Power Ratio: Design/Required	1.23	0.08	6.87	1.01
<u>$\lambda = 4.64 \mu\text{m}$</u>				
Transmitter Power, p_t	2 MW	2 MW	2 MW	2 MW
Design Received Power, P_r (W)	7×10^{-12}	8×10^{-13}	3×10^{-11}	3×10^{-12}
Required Received Power (W)	3×10^{-11}	3×10^{-11}	3×10^{-11}	3×10^{-11}
Power Ratio: Design/Required	0.22	0.02	0.92	0.08

Although detection using pulse compression at $4.64 \mu\text{m}$ is still unsuccessful, received power is within two orders of magnitude of the required minimum. At $11.17 \mu\text{m}$, Table 11 shows that detection is successful under most conditions, with

insufficient received power only under worst-case conditions at Diego Garcia. Recalling that worst-case conditions correspond to off-boresight detection of a target through cirrus at 60° look-angle with significant heterodyne misalignment, the calculations show that the pulse compression method leads to reliable target detection under most realistic operational conditions. The high GEODSS site elevations at Taegu and Maui could also be expected to exhibit similar atmospheric transmittance and turbulence characteristics to Socorro, implying that detection performance at these sites is likely to be similar to the calculations shown for Socorro.

Resolution and Accuracy. Using Equation (91) from Chapter V, the resolution and accuracy of the successful pulse compression LADAR design can be calculated. For an obscuration ratio of 0.2, primary aperture diameter of 1.75 m. and $\lambda = 11.17 \mu\text{m}$, the diffraction-limited angular accuracy and resolution is $7.4 \mu\text{rad}$. Conversely, for a detector dimension ratio $L/g = 4$, $L = 25 \mu\text{m}$, and an effective receiver-telescope focal-length of 4 meters, the detector-limited angular accuracy and resolution is $14.1 \mu\text{rad}$.

Assuming average turbulence conditions, the angular performance of this design is detector-limited. That is, the design will theoretically be able to differentiate between two targets which are only 500 m apart at geosynchronous orbit, and be able to determine their angular position to within 500 m. If the FPA consists of 128×128 elements, the linear FOV at 36,000 km range is about 65 km. This small 'footprint' means that search rates will be slow, necessitating a reasonably accurate *a priori* estimate of target orbital elements.

Since pulse compression is used, the effective pulse width is given by $1/B_{FM}$, which corresponds to 1.7 ns. This extremely short pulse width provides a range resolution and accuracy of 25 cm — more than enough for satellite detection requirements. Also, since many long pulses are transmitted at a low repetition rate, the velocity resolution given by $\lambda/2T$ is extremely small at about $5 \mu\text{m/s}$.

However, the long duration of the transmitted waveform and the resolution of Doppler-filter circuits would probably be limiting factors to velocity and range resolution. During the 1.1-second period in which the transmitted waveform is interacting with the target, the target may move significantly, causing inaccurate measurement of instantaneous Doppler-shift and range.

Sensitivity and Coverage. The sensitivity of LADAR detection depends on target characteristics, viewing geometry, atmospheric conditions, turbulence, and site elevation. With good conditions, target cross-sections considerably smaller than 4 m^2 could theoretically be detected, especially from high elevations.

The calculation of SNR and, hence, received power, is based on the underlying assumption of shot-noise limited detection. This condition occurs if enough LO power is provided so that the background signal is negligible in comparison to the LO-induced shot noise. Background power may be calculated using Figure 7 in Chapter V. The expected worst-case background spectral radiance at $11.17 \text{ } \mu\text{m}$, assumed constant across the IF bandwidth, is about $5 \text{ W m}^{-2}\text{sr}^{-1}\mu\text{m}^{-1}$. For the FPA dimensions used, the receiver FOV is about 2.54 micro-steradians, while the receiver aperture area is 2.4 m^2 and IF bandwidth is 650 MHz. These values yield an expected background signal power of about 8 nW. Therefore, providing LO power above about $1 \text{ } \mu\text{W}$ will ensure shot-noise limited operation.

The maximum look angle used in worst-case design calculations was 60° , corresponding to GEODSS maximum angular coverage. Apart from Diego Garcia, all other sites should be capable of geosynchronous coverage equal to or better than GEODSS. The Diego Garcia site may be restricted to smaller look angles under worst-case conditions.

Summary

Design calculations show that reliable detection of unenhanced geosynchronous objects using an unmodulated pulse train from a ground-based IR LADAR is currently not possible at either of the candidate wavelengths. State-of-the-art LADAR performance parameters were used to calculate received signal power under both ideal and worst-case detection conditions for the GEODSS sites at Socorro and Diego Garcia. Worst-case conditions included maximum look-angle viewing through cirrus cloud, with a target located $5 \mu\text{rad}$ off-boresight and heterodyne misalignment of $5 \mu\text{rad}$. These calculations show that an increase in received power by at least four orders of magnitude is necessary for reliable detection of a typical geosynchronous object. The low level of received power is primarily due to the extremely large amount of free-space loss experienced by a LADAR signal reflected from a range of 36,000 km.

Two alternative design concepts using an unmodulated pulse train were presented which are aimed at increasing received power. The first entails location of the LADAR sensor in a deep-space orbit to reduce the target range. Calculations show that successful detection is possible for a sensor located at an altitude of at least 30,000 km. Although pointing accuracy and platform stability are critical to the success of the space-based sensor, a comprehensive analysis of space-based satellite detection is beyond the scope of this research.

The second alternative design concept assumes that the target is fitted with a small corner-cube reflector which is reflective at IR wavelengths. Calculations show that the resultant dramatic increase in target cross-section allows successful target detection under nearly all conditions for both candidate wavelengths.

Finally, design calculations were performed for an unenhanced target using the original ground-based IR LADAR with pulse compression. The results show that successful detection is possible under most operational conditions at $11.17 \mu\text{m}$, while received power at $4.64 \mu\text{m}$ is two orders of magnitude below the required

minimum. Resolution and accuracy of the 11.17 μm system is very good, and deep-space LADAR coverage is at least as good as GEODSS.

VII. Conclusions

The purpose of this research was to determine the minimum performance requirements for a ground-based, IR LADAR for deep-space satellite detection, and to select a candidate sensor design using available technology. The first stage of research included a review of typical deep-space target characteristics and long-range IR LADAR techniques. A typical target cross-section of 4 m^2 and range of 36,000 - 40,000 km was selected for design calculations, along with LADAR design architecture based on heterodyne FPA detection, a MOPA transmitter configuration, and a Ritchey-Chretien telescope design.

Two transmitter waveforms were considered for the LADAR application: an unmodulated rectangular pulse train, and a linear-FM 'chirp' pulse train. The FM-chirp pulse train was emphasized since it allows use of pulse compression techniques in the receiver to compress the effective pulse width, and increase the effective pulse amplitude, by several orders of magnitude. A target acquisition scheme using separate transmit and receive telescopes was also presented which greatly reduces acquisition time and improves system sensitivity.

Characteristics of several high-power pulsed lasers were then reviewed, including Nd:YAG, DF, $^{12}\text{CO}_2$, $^{13}\text{CO}_2$, and frequency-doubled $^{12}\text{CO}_2$. Of these, the CO_2 -variant lasers were selected for further study, based on their technological maturity, high power, narrow linewidth, and small chirp characteristics.

The second stage of research involved calculation of background radiance, atmospheric transmission, and turbulence effects for typical operational conditions across the IR band. Of the candidate CO_2 lasers, the $^{13}\text{CO}_2$ laser using the P(22) transition at $11.17 \mu\text{m}$ and the frequency-doubled $^{12}\text{CO}_2$ laser using the R(20) transition at $4.64 \mu\text{m}$ were selected as optimum in terms of transmission under a wide range of atmospheric conditions.

Other results derived were that average cirrus cloud conditions have relatively minor effects on transmission, while rain attenuation is severe at all IR wavelengths. Two turbulence effects — scintillation and coherence loss — were highlighted as serious for LADAR applications. However, addition of a system signal-to-noise margin serves to overcome scintillation effects, while limiting the size of telescope apertures avoids coherence loss under most turbulence conditions.

The third stage of research consisted of parametric analysis of the LADAR detection problem using diffraction theory for obscured circular telescope apertures, a Gaussian-profile laser beam, heterodyne detection, and a two-dimensional array of square detector elements separated by finite gaps. The effects of Gaussian and uniform LO-irradiance over the detector were included in the analysis, along with beam truncation and obscuration, heterodyne misalignment, off-boresight detection, optics transmittance, atmospheric transmittance, and a diffuse target cross-section. Additional equations were presented to allow calculation of LADAR accuracy and resolution performance. Although the parametric analysis was carried out for ground-based deep-space IR LADAR applications, the resultant equation set is sufficiently general to be used for most LADAR designs using heterodyne detection.

The set of derived parametric equations was then used in the final stage of research to assess the performance of several candidate system designs. LADAR component specifications for the designs were based on current technology using the two final candidate laser wavelengths, with calculations performed for both ideal and worst-case detection conditions from two typical LADAR sites. Using the unmodulated pulse train waveform, the analysis shows that an increase in received power by at least four orders of magnitude is necessary for reliable detection of a typical geosynchronous object. The major reason for low received power is the amount of free-space loss incurred over the long range to deep-space. Additional limitations exist for transmitter power and aperture sizes due primarily to atmospheric effects such as turbulence and thermal blooming.

Two alternative design concepts using an unmodulated pulse train were presented which are aimed at increasing received power. The first concept entails location of the LADAR sensor in space at an altitude of at least 30,000 km to achieve successful detection; however, pointing accuracy, platform stability, sensor control, and power generation issues were not addressed in the analysis. The second alternative concept assumes that a small corner-cube reflector is fitted to the target, providing enhanced signal returns which allow successful detection under all conditions. Although both alternative concepts appear theoretically feasible, considerable problems exist with their practical implementation.

Finally, design calculations were performed for an unenhanced target using a ground-based IR LADAR with pulse compression. The results show that successful detection is possible under most operational conditions at 11.17 μm , while received power at 4.64 μm is two orders of magnitude below the required minimum. Resolution and accuracy of the 11.17 μm system is very good, and deep-space LADAR coverage is at least as good as GEODSS.

Selection of heterodyne detection and pulse compression techniques, combined with recent improvements in CO₂ laser and FPA technology has produced a 'first-level' LADAR system design which is theoretically feasible. Compared to GEODSS performance, a network of LADAR sites positioned at the same locations as GEODSS promises much-improved availability due to the capability of operation in daylight and cloudy-sky conditions. However, the narrow beamwidth and relatively long signal round-trip time to deep-space means that a reasonably accurate *a priori* estimate of the target orbital elements is required so that search-time is reduced.

Recommendations

Additional preliminary analyses and design calculations are required before implementation of the successful candidate design. More specific data concerning atmospheric seeing conditions at prospective LADAR sites is needed in order

to determine maximum aperture sizes, and to accurately assess the likely effect of haze and turbulence on system performance. Assuming co-location with GEODSS, much of this data may be available from previous GEODSS environmental studies. Additionally, a more comprehensive analysis of acquisition, tracking, and pointing performance is required in light of the large telescope size and narrow beamwidths required. Finally, further development of $^{13}\text{CO}_2$ laser technology is desirable so that pulse repetition rate is increased from the currently-reported levels, while high pulse power is maintained.

Appendix A. *FPA Detection Analysis*

The first objective of FPA detection analysis is to determine the maximum possible power, S_n , from a single pixel within a group of n pixels which contain all of the image disk. The image disk, in this case, is a disk of constant irradiance with radius ω_A , and is used to approximate the received Airy pattern. Exact values of ω_A for different obscuration ratios can be found in Chapter V. The location of the image disk center is confined to a finite region when the image overlaps n pixels, with the *expected* location of the image center given by the centroid of the area of possible image center locations. Therefore, S_n is found by first calculating the centroid of the area of image centers, and then evaluating the expected fraction of image disk which overlaps an active detector pixel.

The second objective is to find the corresponding probability, p_n , that all image power is contained within n pixels, so that S_n and p_n can then be combined to calculate the expected value of the maximum received signal, $E\{S_R\} = \sum_{n=1}^4 S_n p_n$. p_n is obtained by calculating the area of all regions which could contain the image center for n overlapped pixels, and then dividing by the total area of a detector element. Using Figure 29 in Chapter V, values of S_n and p_n for $n = 2, 3$, and 4 will now be developed. Values for $n = 1$ are given in Chapter V, while values for $n > 4$ are not required, since this analysis constrains the image disk size to values less than the pixel size.

Two Overlapped Pixels

Figure 33 provides the detector geometry for the case of two pixels overlapped by the received image. The pixels have dimensions of $2L \times 2L$, and are separated by a gap of width g . Only one of the four areas of possible image centers requires analysis since the other three have identical shape and size, and are symmetrically placed.

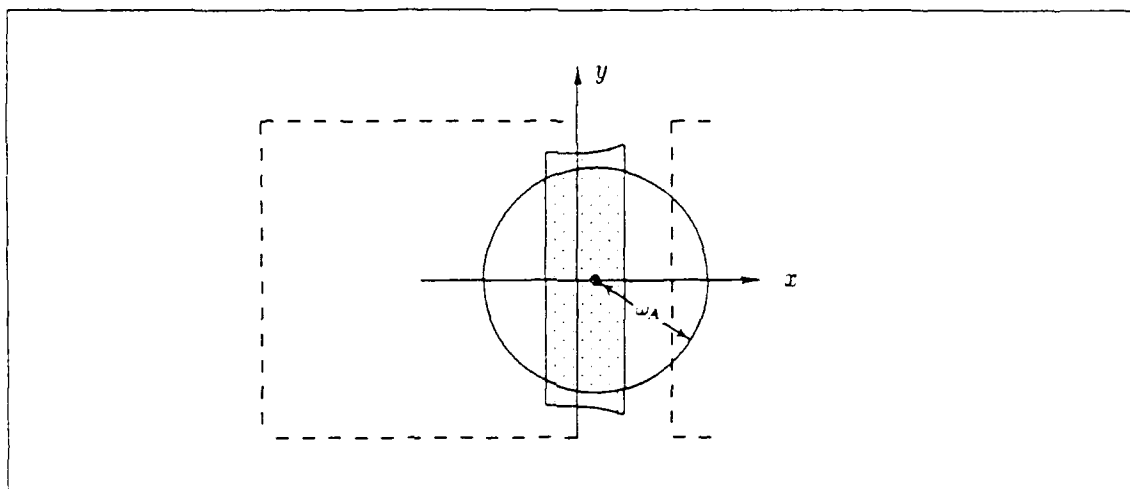


Figure 33. Image Center Geometry for the Case of Two Overlapped Pixels

The area of image centers, A_2 , shown in Figure 33 can be written as the area of a rectangle plus the area of two diverging wedge-shaped sections as follows:

$$\begin{aligned}
 A_2 &= \left(\omega_A - \frac{g}{2} \right) (2L - 2\omega_A + 2g) + 2 \int_0^{g/2} \left[\omega_A - (\omega_A^2 - x^2)^{1/2} \right] dx \\
 &= \left(\omega_A - \frac{g}{2} \right) (2L - 2\omega_A + 2g) - \frac{g}{2} \left(\omega_A^2 - \frac{g^2}{4} \right)^{1/2} - \omega_A^2 \arcsin \left(\frac{g}{2\omega_A} \right) + g\omega_A \quad (93)
 \end{aligned}$$

The centroid of the area of image centers is now required so that the expected location of the image can be fixed. Clearly, the y centroid coordinate is $\bar{y} = 0$. The \bar{x} value can be obtained by calculating $\bar{x} = M_y / A_2$, where M_y is the area moment with respect to the y axis. M_y can be written as:

$$\begin{aligned}
 M_y &= 2 \int_{g-\omega_A}^0 x(L - \omega_A + g) dx + 2 \int_0^{g/2} x \left[L + g - (\omega_A^2 - x^2)^{1/2} \right] dx \\
 &= \frac{g^2}{4} (L + g) - (g - \omega_A)^2 (L - \omega_A + g) - \frac{2\omega_A^3}{3} + \frac{2(\omega_A^2 - g^2/4)^{3/2}}{3} \quad (94)
 \end{aligned}$$

Therefore, the centroid coordinates are $(\bar{x}, \bar{y}) = (\frac{M_y}{A_2}, 0)$. The corresponding expected area of overlapped pixel, O_2 , when the image is centered at (\bar{x}, \bar{y}) , is:

$$\begin{aligned} O_2 &= 2 \int_{-\omega_A}^{-M_y/A_2} (\omega_A^2 - x^2)^{1/2} dx \\ &= \omega_A^2 \left[\frac{\pi}{2} - \arcsin \left(\frac{M_y}{\omega_A A_2} \right) \right] - \frac{M_y}{A_2} \left[\omega_A^2 - \left(\frac{M_y}{A_2} \right)^2 \right]^{1/2} \end{aligned} \quad (95)$$

Since the image disk area is $\pi\omega_A^2$, the expected fraction of total disk power can be expressed as:

$$\frac{S_2}{P_{disk}(\gamma)} = \frac{O_2}{\pi\omega_A^2} = \frac{1}{\pi} \left[\frac{\pi}{2} - \arcsin \left(\frac{M_y}{\omega_A A_2} \right) \right] - \frac{M_y}{\pi A_2 \omega_A^2} \left[\omega_A^2 - \left(\frac{M_y}{A_2} \right)^2 \right]^{1/2} \quad (96)$$

In a similar fashion to the calculation of p_1 in Chapter V, the value of p_2 can be found by dividing the area of all possible image center locations by the area of a detector element. In this case, the area of a detector element consists of the pixel area plus half of the adjoining gap area. That is,

$$p_2 = \frac{4A_2}{(2L + g)^2} \quad (97)$$

Equations (96) and (97) contribute to the calculation of $E\{S_R\}$ for the case of two overlapped pixels. The corresponding equations for the cases of three and four overlapped pixels are now developed in a similar manner.

Three Overlapped Pixels

Figure 34 depicts the image center geometry for the case of three overlapped pixels. The area of image centers, A_3 , can be written as the sum of areas formed from three vertical slices as follows:

$$\begin{aligned}
 A_3 = & \int_{g/2}^g \left\{ \left[\omega_A^2 - (x - g)^2 \right]^{1/2} - \left(\omega_A^2 - x^2 \right)^{1/2} \right\} dx \\
 & + \int_g^{\left(\omega_A^2 - \frac{g^2}{4} \right)^{1/2}} \left[\omega_A - \left(\omega_A^2 - x^2 \right)^{1/2} \right] dx \\
 & + \int_{\left(\omega_A^2 - \frac{g^2}{4} \right)^{1/2}}^{\omega_A} \left[\omega_A - g + \left(\omega_A^2 - x^2 \right)^{1/2} \right] dx
 \end{aligned}$$

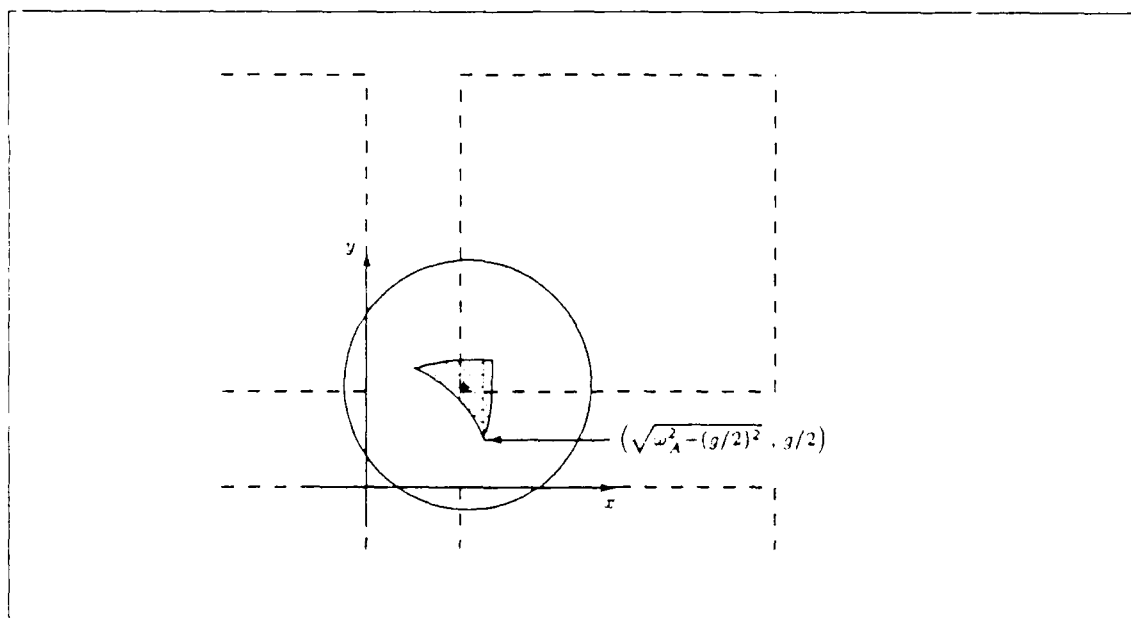


Figure 34. Image Center Geometry for the Case of Three Overlapped Pixels

After some algebra, the expression for A_3 reduces to:

$$A_3 = \omega_A^2 - 2g\omega_A + g \left(\omega_A^2 - \frac{g^2}{4} \right)^{1/2} + \frac{\omega_A^2}{2} \left\{ \frac{\pi}{2} + \arcsin \left(\frac{g}{2\omega_A} \right) - \arcsin \left[\frac{\left(\omega_A^2 - \frac{g^2}{4} \right)^{1/2}}{\omega_A} \right] \right\} \quad (98)$$

The centroid for the $n = 3$ case is located at $(\bar{x}, \bar{y}) = \left(\frac{M_y}{A_3}, \frac{M_x}{A_3} \right)$. However, $M_y = M_x \equiv M_3$ due to the region's symmetrical nature. Using three vertical slices again, the expression for M_3 is given by:

$$M_3 = \int_{g/2}^g x \left\{ \left[\omega_A^2 - (x-g)^2 \right]^{1/2} - \left(\omega_A^2 - x^2 \right)^{1/2} \right\} dx + \int_g^{\left(\omega_A^2 - \frac{g^2}{4} \right)^{1/2}} x \left[\omega_A - \left(\omega_A^2 - x^2 \right)^{1/2} \right] dx + \int_{\left(\omega_A^2 - \frac{g^2}{4} \right)^{1/2}}^{\omega_A} x \left[\omega_A - g + \left(\omega_A^2 - x^2 \right)^{1/2} \right] dx$$

After some algebra, the expression for M_3 reduces to:

$$M_3 = \frac{\omega_A^3}{6} - \frac{g^3}{24} - \frac{\omega_A g^2}{2} + \frac{g^2}{4} \left(\omega_A^2 - \frac{g^2}{4} \right)^{1/2} + \frac{g\omega_A^2}{2} \arcsin \left(\frac{g}{2\omega_A} \right) \quad (99)$$

The corresponding area of overlapped pixel, O_3 , for the image centered at $\left(\frac{M_1}{A_1}, \frac{M_1}{A_1} \right)$ can be found from two different cases of detection geometry corresponding to two different ranges of L/g ratio. Figure 35 shows both cases, where the centroid is located either on the pixel itself $\left(g - \frac{M_1}{A_3} < 0 \right)$, or in the gap region $\left(g - \frac{M_1}{A_3} > 0 \right)$.

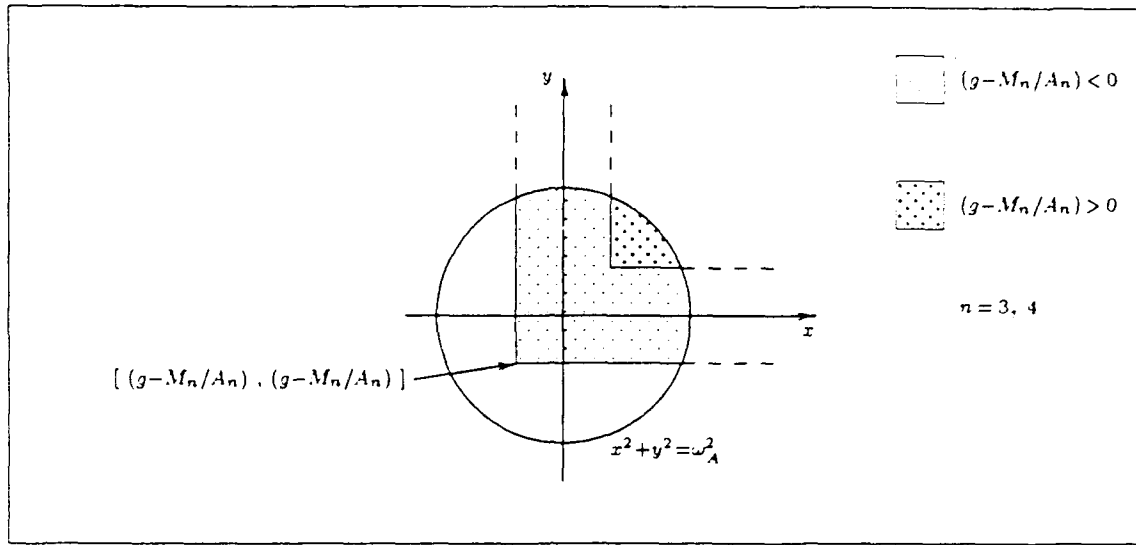


Figure 35. The Two Possible Image-Pixel Geometries for the Cases of Three and Four Overlapped Pixels

For the case of $g - \frac{M_1}{A_3} < 0$, O_3 is expressed as the sum of the four pixel areas separated by the x and y axes as follows:

$$O_3 = \frac{\pi \omega_A^2}{4} + \left(g - \frac{M_3}{A_3}\right)^2 + 2 \int_{\left(g - \frac{M_3}{A_3}\right)}^0 (\omega_A^2 - x^2)^{1/2} dx$$

which yields:

$$O_3 = \frac{\pi \omega_A^2}{4} + \left(g - \frac{M_3}{A_3}\right)^2 - \left(g - \frac{M_3}{A_3}\right) \left[\omega_A^2 - \left(g - \frac{M_3}{A_3}\right)^2 \right]^{1/2} - \omega_A^2 \arcsin \left(\frac{g - \frac{M_3}{A_3}}{\omega_A} \right) \quad (100)$$

while for $(g - \frac{M_3}{A_3} > 0)$, the expression for O_3 is:

$$\begin{aligned}
 O_3 &= \int_{\left(g - \frac{M_3}{A_3}\right)}^{\left[\omega_A^2 - \left(g - \frac{M_3}{A_3}\right)^2\right]^{1/2}} \left[\left(\omega_A^2 - x^2\right)^{1/2} - \left(g - \frac{M_3}{A_3}\right) \right] dx \\
 &= \left(g - \frac{M_3}{A_3}\right)^2 - \left(g - \frac{M_3}{A_3}\right) \left[\omega_A^2 - \left(g - \frac{M_3}{A_3}\right)^2 \right]^{1/2} \\
 &\quad + \frac{\omega_A^2}{2} \left[\arcsin \left\{ \frac{\left[\omega_A^2 - \left(g - \frac{M_3}{A_3}\right)^2 \right]^{1/2}}{\omega_A} \right\} - \omega_A^2 \arcsin \left(\frac{g - \frac{M_3}{A_3}}{\omega_A} \right) \right] \quad (101)
 \end{aligned}$$

The expected received fraction of total disk power is then found in a similar fashion to S_2 as:

$$\frac{S_3}{P_{disk}(\gamma)} = \frac{O_3}{\pi \omega_A^2} \quad (102)$$

where O_3 is determined from Equations (100) or (101), depending on FPA dimensions. The expression for p_3 is found in the same manner as for p_2 , with four areas of possible image center locations given by Equation (98). The p_3 expression is then written as:

$$p_3 = \frac{4A_3}{(2L + g)^2} \quad (103)$$

Four Overlapped Pixels

Figure 36 shows the image center geometry for the case of four overlapped pixels. Area A_4 can be written as follows:

$$A_4 = \int_{g/2}^{\left(\omega_A^2 - \frac{g^2}{4}\right)^{1/2}} \left[\left(\omega_A^2 - x^2\right)^{1/2} - \frac{g}{2} \right] dx \quad (104)$$

which reduces to

$$A_4 = \frac{g^2}{4} - \frac{g}{2} \left(\omega_A^2 - \frac{g^2}{4} \right)^{1/2} + \frac{\omega_A^2}{2} \left\{ \arcsin \left[\frac{\left(\omega_A^2 - \frac{g^2}{4} \right)^{1/2}}{\omega_A} \right] - \arcsin \left(\frac{g}{2\omega_A} \right) \right\} \quad (105)$$

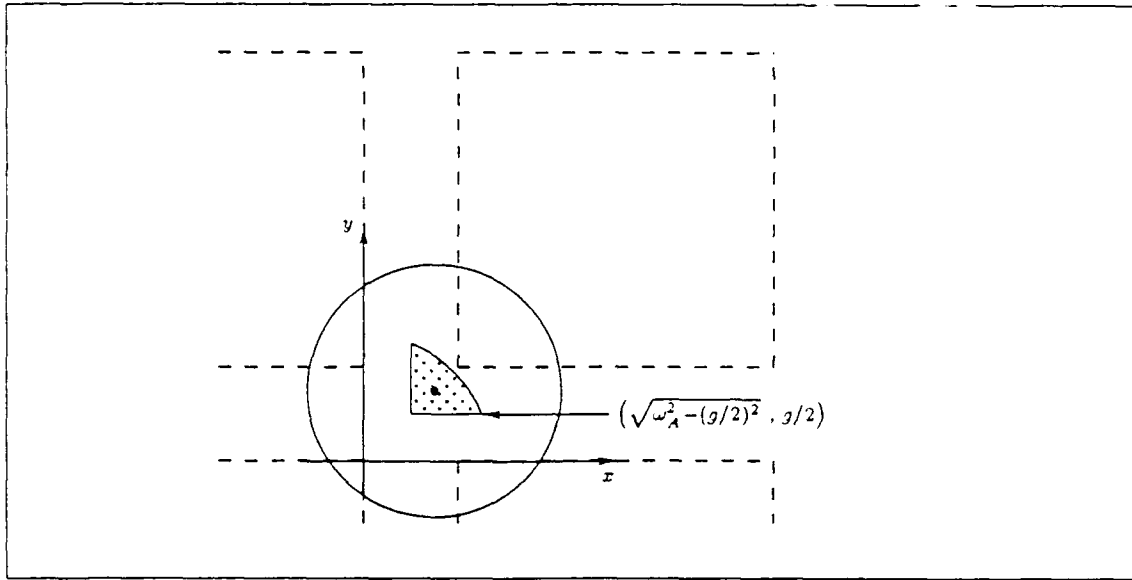


Figure 36. Image Center Geometry for the Case of Four Overlapped Pixels

As for the $n = 3$ case, $M_y = M_x \equiv M_4$ due to the symmetrical region, A_4 . M_4 is expressed as:

$$\begin{aligned} M_4 &= \int_{g/2}^{\left(\omega_A^2 - \frac{g^2}{4} \right)^{1/2}} x \left[\left(\omega_A^2 - x^2 \right)^{1/2} - \frac{g}{2} \right] dx \\ &= \frac{g^3}{12} - \frac{g\omega_A^2}{4} + \frac{\left(\omega_A^2 - \frac{g^2}{4} \right)^{3/2}}{3} \end{aligned} \quad (106)$$

The corresponding area of overlapped pixel, O_4 , is found to be identical in form to the case of three overlapped pixels. The image-pixel geometry used to calculate

O_4 is given by Figure 35 and the relevant expression for O_4 when $(g - \frac{M_4}{A_4} < 0)$ is written as

$$O_4 = \frac{\pi \omega_A^2}{4} + \left(g - \frac{M_4}{A_4}\right)^2 - \left(g - \frac{M_4}{A_4}\right) \left[\omega_A^2 - \left(g - \frac{M_4}{A_4}\right)^2 \right]^{1/2} - \omega_A^2 \arcsin \left(\frac{g - \frac{M_4}{A_4}}{\omega_A} \right) \quad (107)$$

and for $(g - \frac{M_4}{A_4} > 0)$, the expression is

$$O_4 = \left(g - \frac{M_4}{A_4}\right)^2 - \left(g - \frac{M_4}{A_4}\right) \left[\omega_A^2 - \left(g - \frac{M_4}{A_4}\right)^2 \right]^{1/2} + \frac{\omega_A^2}{2} \left[\arcsin \left\{ \frac{\left[\omega_A^2 - \left(g - \frac{M_4}{A_4}\right)^2 \right]^{1/2}}{\omega_A} \right\} - \omega_A^2 \arcsin \left(\frac{g - \frac{M_4}{A_4}}{\omega_A} \right) \right] \quad (108)$$

From Equations (102) and (103), S_4 and p_4 are then determined using:

$$\frac{S_4}{P_{disk}(\gamma)} = \frac{O_4}{\pi \omega_A^2} \quad (109)$$

and

$$p_4 = \frac{4A_4}{(2L + g)^2} \quad (110)$$

Summary

Equations have been developed which specify the maximum power possible, S_n , from a single pixel within a group of n pixels, which contain all of the image disk. These equations are shown graphically in Figure 30 (Chapter V) for an obscuration ratio of 0.2, and in Figures 37 and 38 for obscuration ratios of 0 and 0.4, respectively.

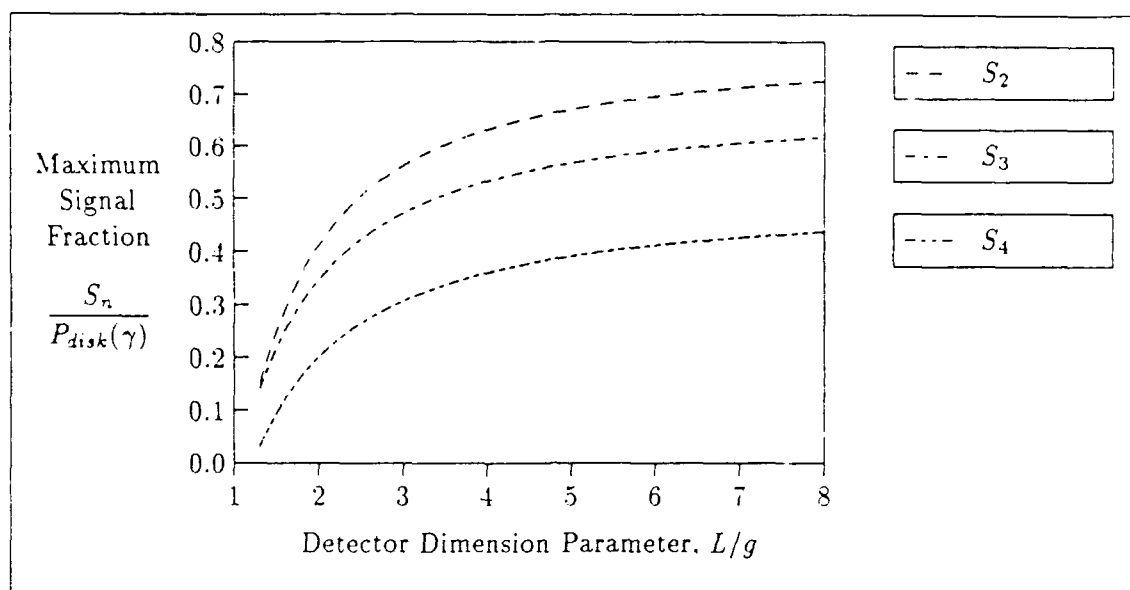


Figure 37. Maximum Signal Fraction when Image Overlays n Pixels and $\gamma = 0$

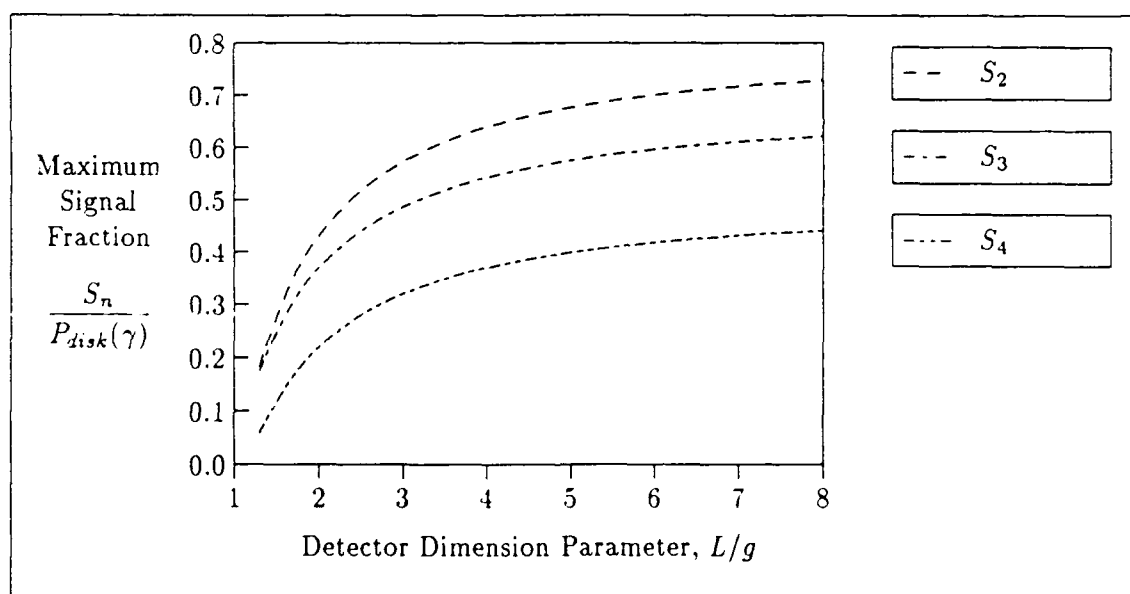


Figure 38. Maximum Signal Fraction when Image Overlays n Pixels and $\gamma = 0.4$

An additional set of equations has been developed for the corresponding probability, p_n , that all image power is contained within n pixels. These equations are

shown graphically in Figure 31 (Chapter V) for an obscuration ratio of 0.2, and in Figures 39 and 40 for obscuration ratios of 0 and 0.4, respectively.

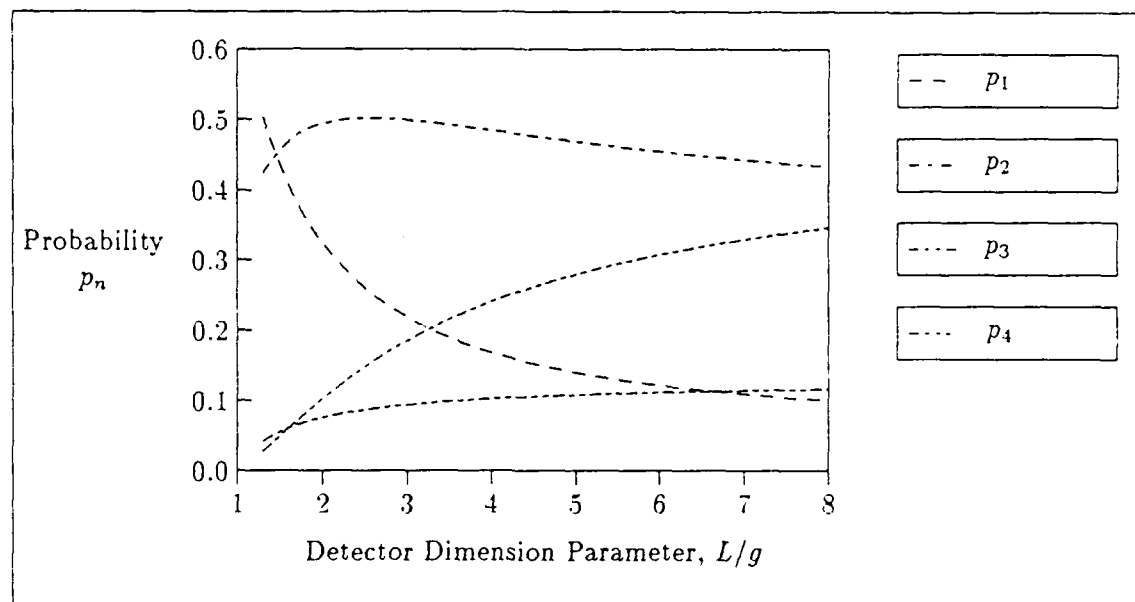


Figure 39. Probability of Image Overlaying n Pixels with $\gamma = 0$

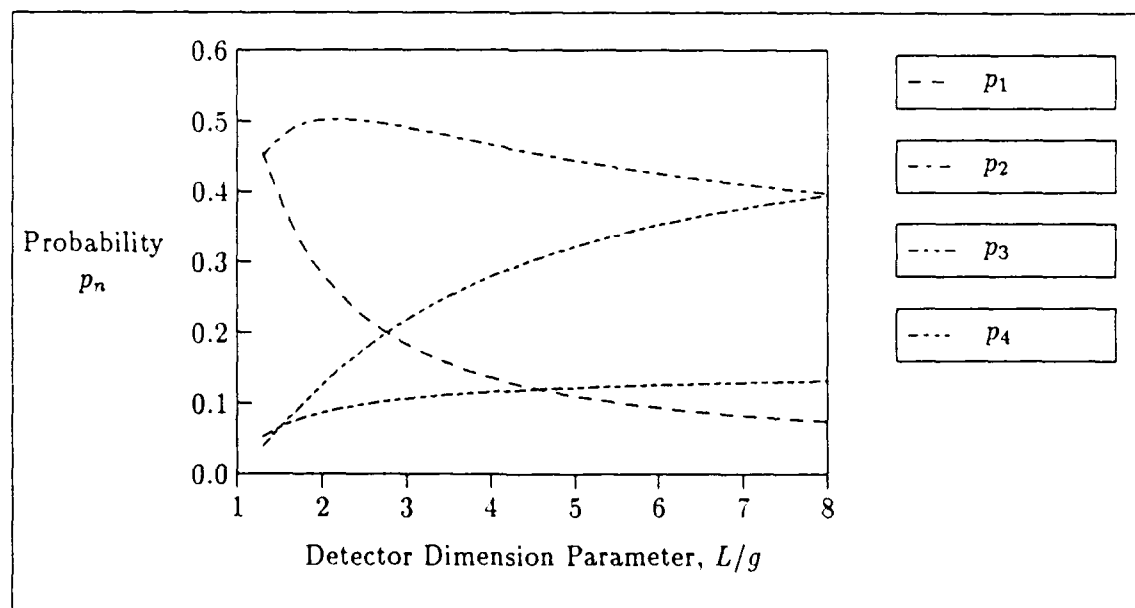


Figure 40. Probability of Image Overlaying n Pixels with $\gamma = 0.4$

The equations for S_n and p_n can then be combined to determine the maximum received signal, $E\{S_R\}$. Figure 32 in Chapter V displays the result for various obscuration ratios.

Bibliography

1. AVCO Everett Research Laboratory. *AMOS User's Manual Revision 5*. Everett MA: AVCO Everett Research Laboratory, 30 September 1982.
2. Agrawal, B. *Design of Geosynchronous Spacecraft*. Englewood Cliffs, NJ: Prentice-Hall, 1986.
3. Anderson, C. C. and Hattar, M. M. "Calorimetric Measurements of Thermal Control Surfaces at Geosynchronous Orbit," *AIAA Paper* 87-15718, 1987.
4. Aruga, T. et al. "Earth-to-Geosynchronous Satellite Laser Beam Transmission," *Applied Optics*, 24: 53-56 (1 January 1985).
5. Autric, M. et al. "Propagation of Pulsed Laser Energy Through the Atmosphere," *AIAA Journal*, 19: 1415-1421 (November 1981).
6. Bachman, C. G. *Laser Radar Systems and Techniques*. Dedham, MA: Artech House Inc, 1979.
7. Balcerak, Raymond et al. "Evolution of a new Semiconductor Product: Mercury Cadmium Telluride Focal Plane Arrays," *Optical Engineering*, 26: 191-199 (March 1987).
8. Barton, David K. *Modern Radar System Analysis*. Norwood, MA: Artech House Inc, 1988.
9. Beaulieu, A. J. "A Practical DF Laser for Ranging Applications," *SPIE Laser Radar Technology and Applications*, 663: 8-13 (1986).
10. Born, M. and Wolf, E. *Principles of Optics*. New York: Pergamon Press, 1970.
11. Braim, S. P. "Technological Constraints on the use of Thermal Imagery for Remote Sensing," *SPIE Applications of Infrared Technology*, 918: 110-119 (1988).
12. Brandewie, Richard A. and Davis, Walter C. "Parametric Study of a 10.6 μm Laser Radar," *Applied Optics*, 11: 1526-1533 (July 1972).
13. Carlson, F. Paul *Introduction to Applied Optics for Engineers*. New York: Academic Press, 1977.
14. Clifford, S. F. and Wandzura, S. "Monostatic Heterodyne Lidar Performance: The Effect of the Turbulent Atmosphere," *Applied Optics*, 22: 514-516 (1 February 1981).
15. Clough, S. A. et al. "Atmospheric Radiance and Transmittance:FASCOD2," *Handout #12 from the workshop on LOWTRAN and FASCOD2* held at Wright-Patterson AFB OH, 1989.
16. Contini, Casey and Honzik, Richard "Staring FPA Modeling Capability," *SPIE Thermal Imaging*, 636: 60-70 (1986).

17. Cruickshank, J. M. "Transversely Excited Atmospheric CO₂ Laser Radar with Heterodyne Detection," *Applied Optics*, 18: 290-293 (1 February 1979).
18. DeVere, G. T. and Johnson, N. L. "The NORAD Space Network," *Spaceflight*, 306-309 (July/August 1985).
19. Degnan, J. J. and Klein, B. J. "Optical Antenna Gain. 2: Receiving Antennas," *Applied Optics*, 13: 2397-2401 (October 1974).
20. Degnan, J. "Satellite Laser Ranging: Current Status and Future Prospects," *IEEE Transactions on Geoscience and Remote Sensing*, 398-413 (July 1985).
21. *Electron Tubes*. Product Catalog Book T13. Amperex Electronic Corporation, Slatersville Division, Slatersville, RI, 1986.
22. Elliott, C. T. "Detectors of Thermal Infrared Radiation," *SPIE Recent Developments in Infrared Components and Subsystems*, 915: 9-19 (1988).
23. Evans, Lt Col H. E., Instructor of Physics. Personal interview. Air Force Institute of Technology, Wright-Patterson AFB OH, 18 January 1989.
24. Fluckiger, D. U. et al. "Optical Autodyne Detection: Theory and Experiment," *Applied Optics*, 26: 318-325 (15 January 1987).
25. Gaposchkin, E. Impact of Metric Accuracy on Deep Space Network Capacity. Project Report STK-141. Contract F19628-85-C-0002. Lexington MA: MIT Lincoln Laboratory, June 1986.
26. Gschwendtner, A. B. "Coherent IR Radar Technology," *Laser and Remote Sensing*, Berlin: Springer-Verlag, 1982.
27. Harney, R. C. "Comparison of Techniques for Long-Range Laser Ranging," *SPIE Laser Radar II*, 783: 91-100 (1987).
28. —. "Dual Active/Passive Infrared Imaging Systems," *Optical Engineering*, 20: 976-980 (November/December 1981).
29. —. "Military Applications of Coherent Infrared Radar," *SPIE Physics and Technology of Coherent Infrared Radar*, 300: 2-10 (1981).
30. Hasegawa, Capt Glenn K. *A FORTRAN Program for Deep-Space Sensor Analysis*. MS thesis, AFIT/GSO/OS/84D-5. School of Engineering, Air Force Institute of Technology (AU), Wright-Patterson AFB OH, December 1984.
31. Hasson, V. et al. "CO₂ Laser Radar Transmitters," *SPIE Laser Radar III*, 999: 19-26 (1988).
32. Hess, R. V. et al. "Coherent Infrared Lidar Mission and Technology Needs for Measurements of Transport and Concentration of Tropospheric Trace Species," *SPIE Coherent Infrared Radar Systems and Applications II*, 415: 52-70 (1983).
33. Howell, J. A. "The Challenge of Space Surveillance," *Sky & Telescope*, 584-588 (June 1987).

34. Huang, C. and Levy, E. "Design Analysis of the Astrometrical Telescope Facility," *SPIE Current Developments in Optical Engineering III*, 965: 148-161 (1988).
35. Hulme, K. F. "CO₂ Laser Heterodyne Rangefinders, Velocimeters and Radars," *Infrared Physics*, 25: 457-466 (1985).
36. Iizuka, K. *Engineering Optics*. Berlin: Springer-Verlag, 1985.
37. Iliff, R. L. and Hadgigeorge, G. "Daytime Ground-to-Satellite Laser Ranging Experiments," *Applied Optics*, 8: 1742-1743 (August 1969).
38. Jamieson, J. A. "Infrared Technology: Advances 1975-84, Challenges 1985-94," *SPIE Infrared Technology X*, 510: 56-68 (1984).
39. Jenkins, R. A. "Infrared Laser Sources," *SPIE Recent Developments in Infrared Components and Subsystems*, 915: 2 (1988).
40. Jursa, Adolph S. *Handbook of Geophysics and the Space Environment*. Air Force Geophysics Laboratory. 1985.
41. Kachelmyer, A. L. "Range-Doppler Imaging: Waveforms and Receiver Design," *SPIE Laser Radar III*, 999: 138-161 (1988).
42. Kaminski, Walter R. "Range Calculations for IR Rangefinder and Designators," *SPIE CO₂ Laser Devices and Applications*, 227: 65-79 (1980).
43. Klein, B. J. and Degnan, J. J. "Optical Antenna Gain. 1: Transmitting Antennas," *Applied Optics*, 13: 2134-2141 (September 1974).
44. —. "Optical Antenna Gain. 3: The Effect of Secondary Element Support Struts on Transmitter Gain," *Applied Optics*, 15: 977-979 (April 1976).
45. Kneizys, F. X. et al. *Atmospheric Transmittance/Radiance: Computer Code LOWTRAN6*. Optical Physics Division, Air Force Geophysics Laboratory, Hanscom AFB MA, August 1983 (AD-A137786).
46. —. *Users Guide to LOWTRAN7*. Handout #1 from the Workshop on LOWTRAN and FASCODE held at Wright-Patterson AFB OH, 1989.
47. Koehler, Capt Charles A. *A Comparison Between the Ground-Based Electro-Optical Deep-Space Surveillance (GEODSS) System and a Proposed Visible Light Space-Based Sensor System for Deep Space Surveillance*. MS thesis, AFIT/GSO/ENS-ENP/86D-2. School of Engineering, Air Force Institute of Technology (AU), Wright-Patterson AFB OH, December 1986.
48. Lange, Maj J.J. and Evans Lt Col H. E. *Electro-Optical Space Systems Technology*. Staff Notes for PHYS 621 Electro-Optical Space Systems Technology. School of Engineering, Air Force Institute of Technology (AU), Wright-Patterson AFB OH, January, 1989

49. Lerou, R. J. "A CW CO₂ Laser Rangefinder Using Heterodyne Detection and On-Off Amplitude Modulation," *Optics and Laser Technology*, 153-159 (June 1983).
50. Lorrain, P. and Corson, D.R. *Electromagnetic Fields and Waves*. San Francisco: W.H. Freeman and Company, 1970.
51. Masten, Michael K. and Hilkert, J. "Electromechanical System Configurations for Pointing, Tracking, and Stabilization Applications," *SPIE Electromechanical System Interaction with Optical Design*, 779: 75-87 (1987).
52. Mathieu, P. and Otis, G. "High Efficiency, Tail-Free Pulses from TEA-CO₂ Lasers," *SPIE Laser Radar Technology and Applications*, 663: 74-77 (1986).
53. Mayer, G. J. Expected Energy Method for Electro-Optical SNR Calculations. Technical Report 634. Contract F19628-80-C-0002. Lexington MA: MIT Lincoln Laboratory, 2 February 1984 (AD A139 984).
54. McGarry, Jan L. et al. "Large Aperture High Accuracy Satellite Laser Tracking," *Proceedings of SPIE*, 641: 77-83. SPIE Press, 1986.
55. Merritt, Paul H. and Meline, Michael E. "Disturbance Effects on a Ground Based Precision Tracking System," *SPIE Acquisition, Tracking, and Pointing*, 641: 32-42 (1986).
56. Miller, A. et al. "A Pulsed Laser Source in the 4.6-4.8 micron Band," *SPIE Recent Developments in Infrared Components and Subsystems*, 915: 3-6 (1988).
57. Moody, Stephen E. "Design of a ¹³C¹⁶O₂ Laser Amplifier," *SPIE Gas Laser Technology*, 894: 102-106 (1988).
58. Nichols Research Corporation. GEODSS Automatic Moving Target Indicator Master Control Parameter Optimization. Technical Report. Contract F05604-85-C-0020. Colorado Springs CO: Nichols Research Corporation, August 1987.
59. O'Shea, D. C. et al. *An Introduction to Lasers and their Applications*. Reading, MA: Addison-Wesley Publishing Company, 1978.
60. Pace, Paul et al. "Frequency-Stabilized Transversely Excited Atmospheric (TEA) CO₂ Lasers for Coherent Infrared Radar Systems," *SPIE Physics and Technology of Coherent Infrared Radar*, 300: 148-152 (1981).
61. —. "A Wide-Aperture, Single Mode TEA-CO₂ Laser with a Low Chirp Rate," *SPIE Active Infrared Systems and Technology*, 806: 41-45 (1987).
62. Potter, Andrew E. "Measuring Debris," *Aerospace America*: 18-22 (June 1988).
63. Powell, Joel "Satellite Tracking with GEODSS," *Spaceflight*, 27: 129-130 (March 1985).
64. Prutzer, S. et al. "Advanced Technologies and State-of-the-Art for High Bandwidth CO₂ Heterodyne Detection," *SPIE Infrared Systems and Components II*, 890: 52-55 (1988).

65. Randolph, Anne "USAF Upgrades Deep Space Coverage," *Aviation Week & Space Technology*, 118: 57-58 (28 February 1983).
66. Reilly, James P. "CO₂ Frequency Stable Amplifier Assessment," *SPIE Laser Radar II*, 733: 60-68 (1987).
67. Schenk, D. D. and Russ, D. S. "Overview of Technology Developments in Coherent Infrared Radar," *SPIE Physics and Technology of Coherent Radar*, 300: 12-17 (1981).
68. Seyrafi, Khalil *Electro-optical Systems Analysis*. Los Angeles: Electro-optical Research Company, 1985.
69. Shapiro, J. H. "Imaging and Target Detection with a Heterodyne-Reception Optical Radar," *Applied Optics*, 20: 3292-3313 (1 October 1981).
70. Shawe, Merrick E. and Adelman, Andrew G. "Precision Laser Tracking for Global and Polar Motion," *IEEE Transactions on Geoscience and Remote Sensing*, GE-23: 391-397 (July 1985).
71. Silver, S. *Microwave Antenna Theory and Design*. New York: McGraw-Hill, 1949.
72. Skolnik, M. I. *Introduction to Radar Systems*. New York: McGraw-Hill Book Company, 1980.
73. —, Ed. *Radar Handbook*. New York: McGraw-Hill Book Company, 1970.
74. "Space Surveillance Deemed Inadequate," *Aviation Week and Space Technology*, 112: 249-259 (16 June 1980).
75. Stockum, Larry A. and Burge, James "Electro-Mechanical Design for Precision Pointing and Tracking Systems," *SPIE Electromechanical System Interaction with Optical Design*, 779: 66-74 (1987).
76. Sullivan, Leo J. "Firepond Laser Radar," *IEEE Electro/81 Conference Record, Session 34/2*: 1-12 (1981).
77. —. "Infrared Coherent Radar," *SPIE CO₂ Laser Devices and Applications*, 227: 148-161 (1980).
78. Taff, L. G. A GEODSS Search Exercise: Search Plan. Project Report STK-145. Contract F19628-85-C-0002. Lexington MA: MIT Lincoln Laboratory, 7 July 1987.
79. Tsunawaki, Y. et al. "Copper and Molybdenum Mirrors for High Power TEA CO₂ Laser," *SPIE CO₂ Laser Applications*, 1019: 414-415 (1988).
80. Ulich, Bobby L. "Overview of Acquisition, Tracking, and Pointing System Technologies," *SPIE Acquisition, Tracking, and Pointing II*, 887: 40-63 (1988).
81. "United States Space Command," *Signal, Special C³I Issue*: 36-44 (1987).

82. Wang, Jon Y. "Detection Efficiency of Coherent Optical Radar." *Applied Optics*, 23: 3421-3427 (1 October 1984).
83. —. "Heterodyne Laser Radar Performance." *SPIE Physics and Technology of Coherent Infrared Radar*, 300: 110-117 (1981).
84. Weber, R. The Passive, Ground-Based, Electro-Optical Detection of Synchronous Satellites. Technical Note 1978-27. Contract F19628-78-C-0002. Lexington MA: MIT Lincoln Laboratory, 19 June 1978 (AD A059 275).
85. Wetherell, W. B. and Rimmer, M. P. "General Analysis of Aplanatic Cassegrain, Gregorian, and Schwarzschild Telescopes." *Applied Optics*, 11: 2817-2832 (December 1972).
86. Witteman, W. J. *The CO₂ Laser*. Berlin: Springer-Verlag, 1987.
87. Wolfe, W. L. and Zissis, G. J. Eds. *The Infrared Handbook*. Office of Naval Research, Department of the Navy, Washington, DC, 1978.
88. Yoder, M. John and Youmans, Douglas G. "Laser Radar Wavelength Selection and Trade-offs," *SPIE Laser Radar III*, 999: 72-83 (1988).

Vita

Flight Lieutenant Kevin F. G. Davey [REDACTED]

[REDACTED] He graduated from Matriculation College in Burnie, Tasmania in December 1977. He then joined the Royal Australian Air Force (RAAF) and attended the Royal Melbourne Institute of Technology, from which he received the degree of Bachelor of Engineering in Electronics Engineering in May 1982. He was employed as a radar systems instructor at the RAAF School of Radio at RAAF Base Laverton, Victoria (Australia) for two years before joining the RAAF F/A-18 new tactical fighter project in September 1984. He completed F/A-18 automatic test equipment training in April 1985 at NAS Lemoore, California before spending three years at RAAF Base Williamtown, New South Wales (Australia) establishing F/A-18 avionics engineering support, including the development of F/A-18 modification procedures and maintenance-pipeline control software. He entered the School of Engineering, Air Force Institute of Technology, in May 1988.

[REDACTED]

UNCLASSIFIED

SECURITY CLASSIFICATION OF THIS PAGE

REPORT DOCUMENTATION PAGE

Form Approved
OMB No. 0704-0188

1a. REPORT SECURITY CLASSIFICATION UNCLASSIFIED			1b. RESTRICTIVE MARKINGS		
2a. SECURITY CLASSIFICATION AUTHORITY			3. DISTRIBUTION/AVAILABILITY OF REPORT Approved for public release; Distribution unlimited.		
2b. DECLASSIFICATION/DOWNGRADING SCHEDULE					
4. PERFORMING ORGANIZATION REPORT NUMBER(S) AFIT/GSO/ENP/ENS/89D-1			5. MONITORING ORGANIZATION REPORT NUMBER(S)		
6a. NAME OF PERFORMING ORGANIZATION School of Engineering		6b. OFFICE SYMBOL (if applicable) AFIT/ENP		7a. NAME OF MONITORING ORGANIZATION	
6c. ADDRESS (City, State, and ZIP Code) Air Force Institute of Technology Wright-Patterson AFB OH 45433-6583			7b. ADDRESS (City, State, and ZIP Code)		
8a. NAME OF FUNDING/SPONSORING ORGANIZATION		8b. OFFICE SYMBOL (if applicable)		9. PROCUREMENT INSTRUMENT IDENTIFICATION NUMBER	
8c. ADDRESS (City, State, and ZIP Code)			10. SOURCE OF FUNDING NUMBERS		
			PROGRAM ELEMENT NO.	PROJECT NO.	TASK NO.
11. TITLE (Include Security Classification) Ground-Based Deep-Space LADAR For Satellite Detection: A Parametric Study					
12. PERSONAL AUTHOR(S) Kevin F. G. Davey, FLTLT, RAAF					
13a. TYPE OF REPORT MS Thesis		13b. TIME COVERED FROM _____ TO _____		14. DATE OF REPORT (Year, Month, Day)	
				15. PAGE COUNT 150	
16. SUPPLEMENTARY NOTATION					
17. COSATI CODES			18. SUBJECT TERMS (Continue on reverse if necessary and identify by block number)		
FIELD	GROUP	SUB-GROUP			
17	05	01	Optical Radar, Laser Tracking, Satellite Detection, Infrared Detection.		
19. ABSTRACT (Continue on reverse if necessary and identify by block number)					
Thesis Advisor: Lieutenant Colonel Howard E. Evans Instructor of Physics					
20. DISTRIBUTION/AVAILABILITY OF ABSTRACT <input checked="" type="checkbox"/> UNCLASSIFIED/UNLIMITED <input type="checkbox"/> SAME AS RPT. <input type="checkbox"/> DTIC USERS			21. ABSTRACT SECURITY CLASSIFICATION UNCLASSIFIED		
22a. NAME OF RESPONSIBLE INDIVIDUAL Howard E. Evans, Lt Col, USAF			22b. TELEPHONE (Include Area Code) (513) 255-2012		22c. OFFICE SYMBOL AFIT/ENP

ABSTRACT

This research determines the minimum performance requirements of a ground-based infrared LADAR designed to detect deep-space satellites, and presents a candidate sensor design based on current technology. The research examines LADAR techniques and detection methods to determine the optimum LADAR configuration, and then assesses the effects of atmospheric transmission, background radiance, and turbulence across the infrared region to find the optimum laser wavelengths. Diffraction theory is then used in a parametric analysis of the transmitted laser beam and received signal, using a Cassegrain telescope design and heterodyne detection. The effects of beam truncation and obscuration, heterodyne misalignment, off-boresight detection, and image-pixel geometry are also included in the analysis.

The derived equations are then used to assess the feasibility of several candidate designs under a wide range of detection conditions including daylight operation through cirrus. The results show that successful detection is theoretically possible under most conditions by transmitting a high-power frequency-modulated pulse train from an isotopic $^{13}\text{CO}_2$ laser radiating at 11.17 micrometers, and utilizing post-detection integration and pulse compression techniques.